Chapter 4

Results and Discussions

4. Results and discussions

4.1. Optimization of the medium for hyaluronic acid production

4.1.1. Microbial growth

Revival of the culture was done from the freeze-dried state on Growth Medium. Microbial growth was observed in the aerobic batch fermentation process**.** As Figure 4.1 (C) observed, a classical sigmoidal growth curve was obtained with a short lag phase (approximately 4 hours) followed by an exponential, stationary, and death phase. As Huang et al. explained, hyaluronic acid's growth and synthesis are measly in the lag phase as the bacterial cell takes time to adapt to a new broth culture environment (Huang et al., 2007). A high metabolic activity characterizes the exponential phase, as DNA, RNA, cell wall components, and other substances necessary for growth are generated for division. The stage is critical to HA's capsular synthesis (Zhang et al., 2016b).

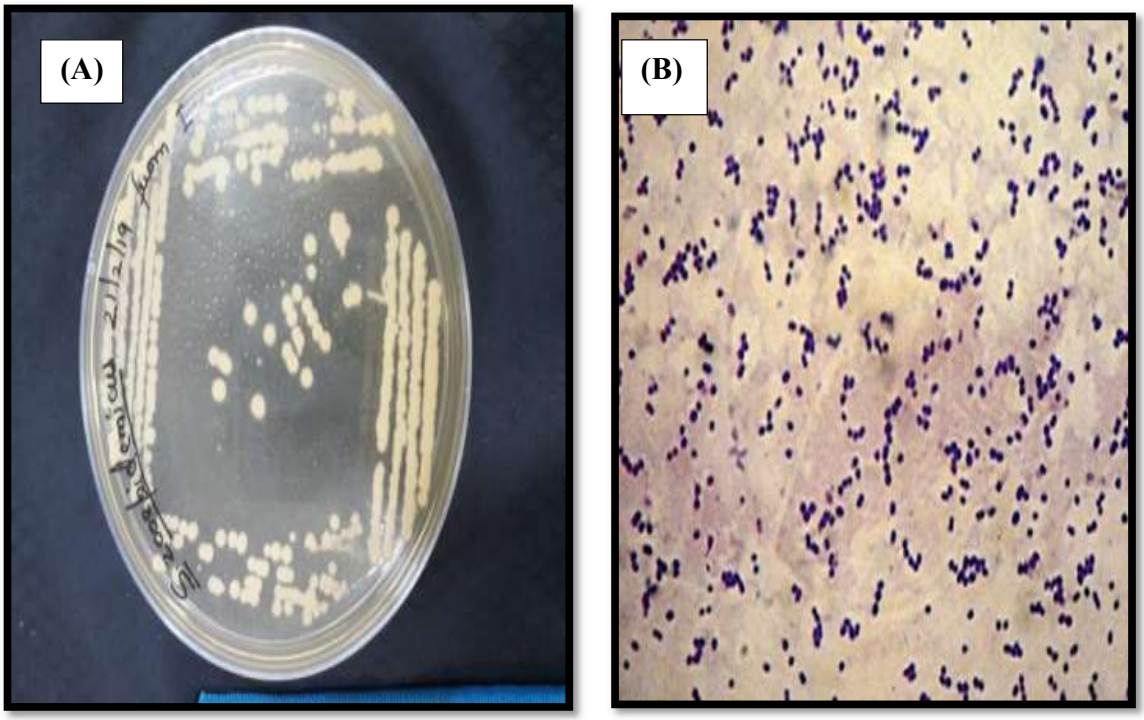

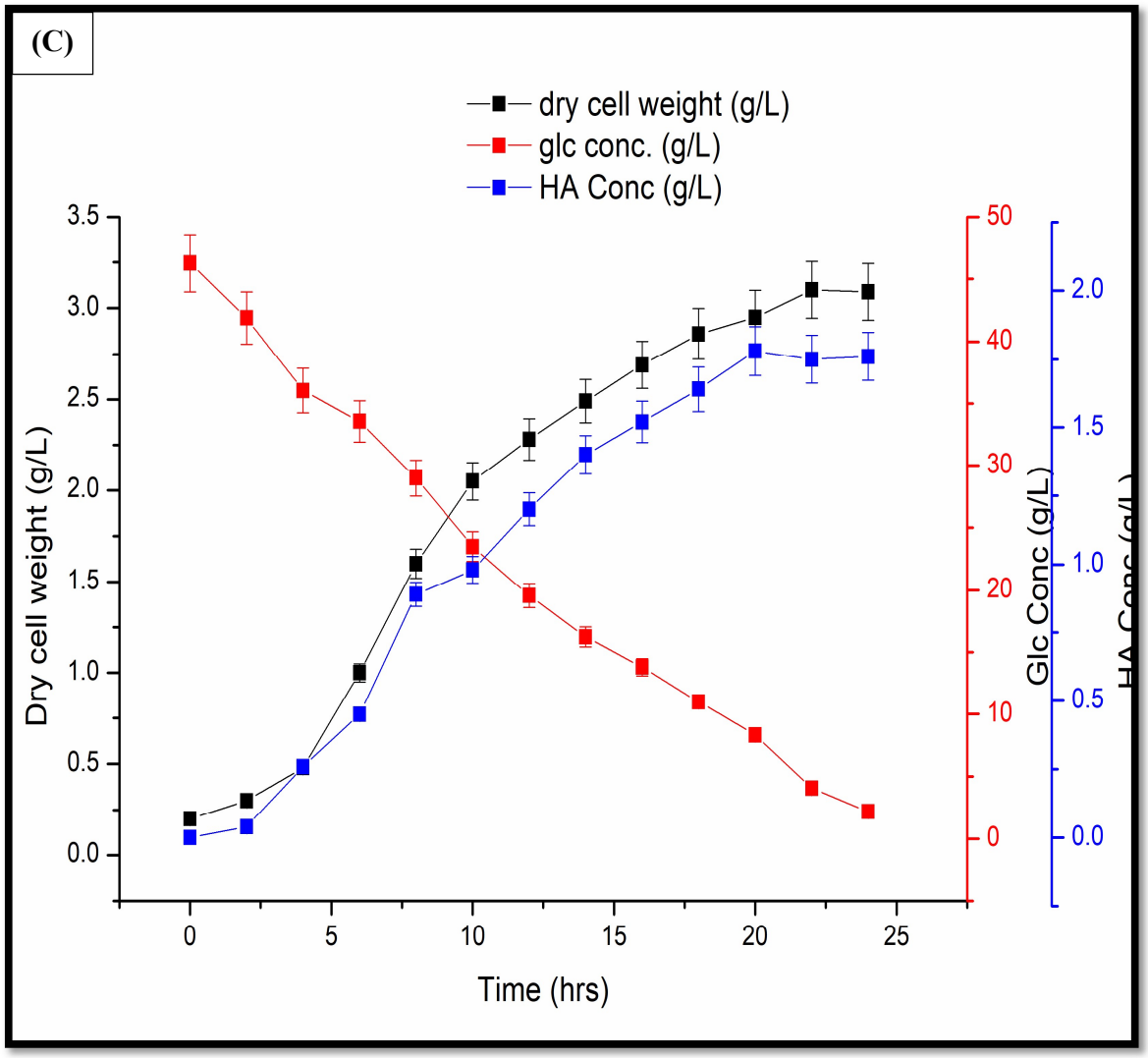

Figure 4.1. (A) *S. zooepidemicus,* (B) Microscopic view of *S. zooepidemicus,* (C) Graph representing growth of *S. zooepidemicus,* HA production, and substrate uptake in growth medium

4.1.2. Hyaluronic Acid Production using one variable at a time method

The *S. zooepidemicus* MTCC 3523 was used for the production of hyaluronic acid by a batch fermentation process performed in a 3.7-liter bioengineering bioreactor. Carbon, the most prominent component of the medium, has a crucial role in the development and production of the metabolite.

It was optimized using different carbon sources in the production process while keeping the other factors constant. Similarly, other inoculum percentages, pH, temperature, and agitation were also optimized, and a combination of them with the physiological state best for the product formation was achieved.

4.1.3. Impact of Carbon Provenance on Hyaluronan Yield

In fermentation, the carbon source is the principal constituent for developing the cellular material and hyaluronic acid production. Carbon sources used for the glycolytic pathway have a significant role in biomass production and in synthesizing the precursors of hyaluronan.

The bacteria fabricate hyaluronic acid in response to stress conditions produced during fermentation. It is used as a barrier against the acidity or alkalinity of the medium (Pires & Santana, 2010). The efficacy of varied carbon provenances on HA production was observed, as demonstrated in Figure 4.2. The production medium was enriched with fructose, lactose, sugarcane molasses, corn powder, tapioca powder, sucrose, maltose, and dextrose.

Molasses was the most productive, yielding 3.16 g/L, followed by fructose, which produced 2.32 g/L. The lowest production was observed in xylose, with a 0.93 g/L yield. Sugarcane molasses are the agricultural industries' by-products; thus, the production cost will be reduced.

The Levenberg–Marquardt nonlinear least square approach was used to assess the parameters to minimize the residual sum of squares. Each experiment was replicated thrice, with the average outcome provided.

The defined medium to produce the required HA glucose concentration was 50 grams per liter. The carbon content of glucose is 40%, which means that in 1 gm of glucose, 0.4g of carbon content is present, and similarly, for 50g of glucose, 20g of carbon content is present. The exact amount of carbon content was used for the rest of the carbon sources utilized during the optimization process so that the HA produced could be assessed on a similar scale.

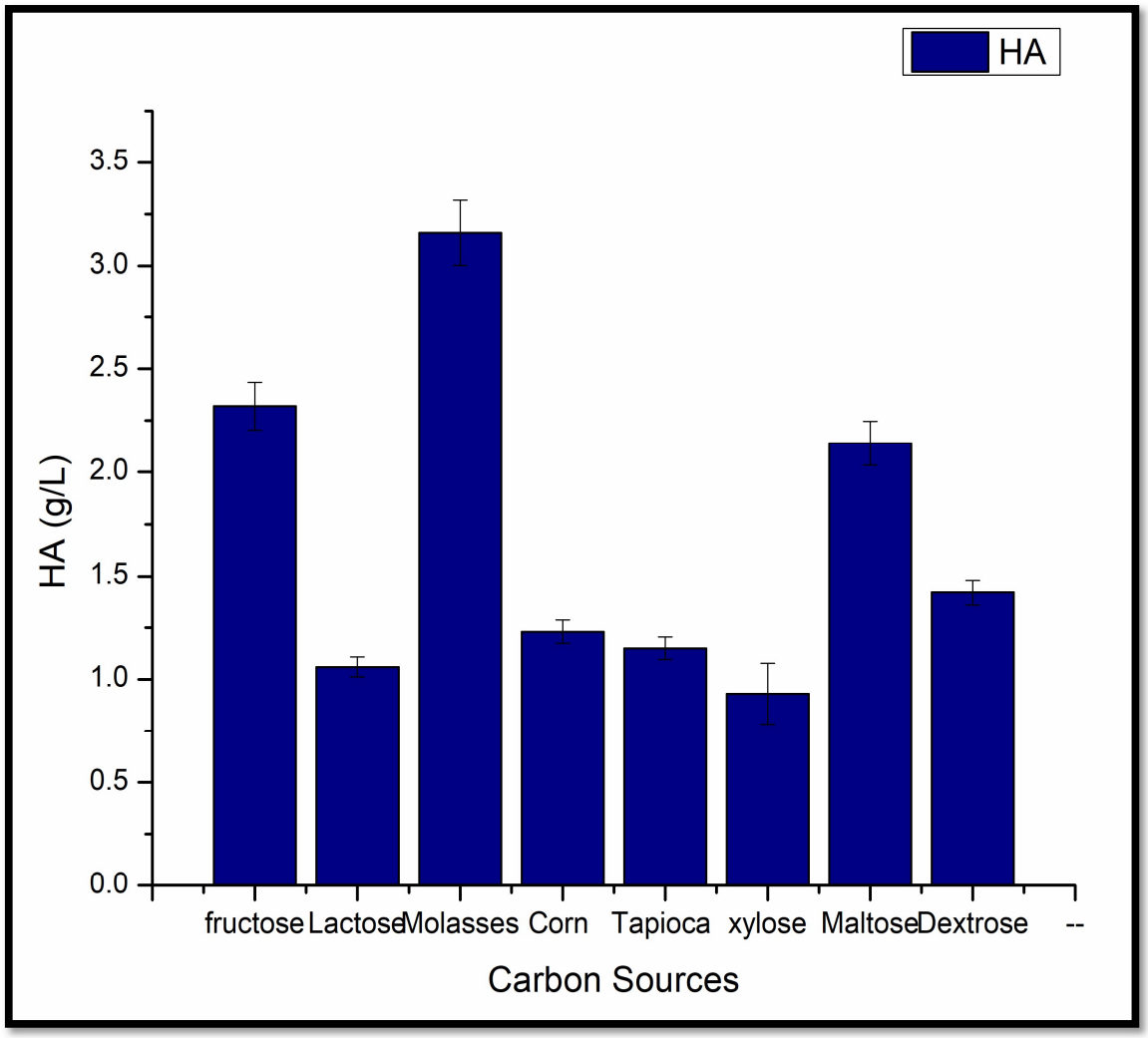

Figure 4.2. The efficacy of varied carbon provenances on HA production while other factors were kept constant, pH 6.8, temperature 37˚C, and agitation at 100 rpm.

Molasses and tapioca powder have a carbon content of around 24% (Samocha et al., 2007) and 40% (Mahariawan et al., 2020), respectively, and cornflour has a carbon content of approximately 46% (Zhu et al., 2015).

Molasses is 75% carbs and 22% water, with no protein or fat. The total reduced sugar in molasses is approximately 17% (Awad El-Kareem, 2003). Sucrose (29% carbohydrate), glucose (12%), and fructose (13%) are the sugars found in molasses (Curtin, 1983).

4.1.4. Effect of molasses percentage

Molasses is the byproduct of the agriculture industry and are often used as a carbon source in fermentation. The recovered molasses was first diluted with distilled water to 15% (w/v) of the total sugar concentration.

The supernatant was collected after 15 minutes of centrifugation at 10,000 rpm and 4°C. The supernatant was then treated for one hour at 70°C with continual stirring with 12 % (w/v) activated charcoal, centrifuged at 4°C at 10,000 rpm, and filtered using a Whatman, n°1 filter (Treichel et al., 2009). Different molasses percentages were used in the medium, and hyaluronic acid production was recorded.

The highest production was recorded at 10% molasses (v/v) with a yield of 3.19 g/L and the lowest at 15% with a 1.9 g/L yield, as shown in figure 4.3. The conditions previously specified in the complex medium were used to determine the optimum HA yields per biomass in culture broth generated using agricultural byproduct molasses: regulated pH (6.8), agitation of 100 rpm, and temperature 37°C.

The carbon and nitrogen sources were 5, 7.5, 10, 12.5, and 15% v/v sugarcane molasses, respectively, while the other salts were the same as in the complex medium. These results were compared thoroughly and recorded that 10 percent molasses concentration gave the most satisfactory results of 3.19 ± 0.15, as shown in Table 4.1 in the production of HA and cell biomass 3.3 ± 0.16 as depicted in Figures 4.4 and 4.5.

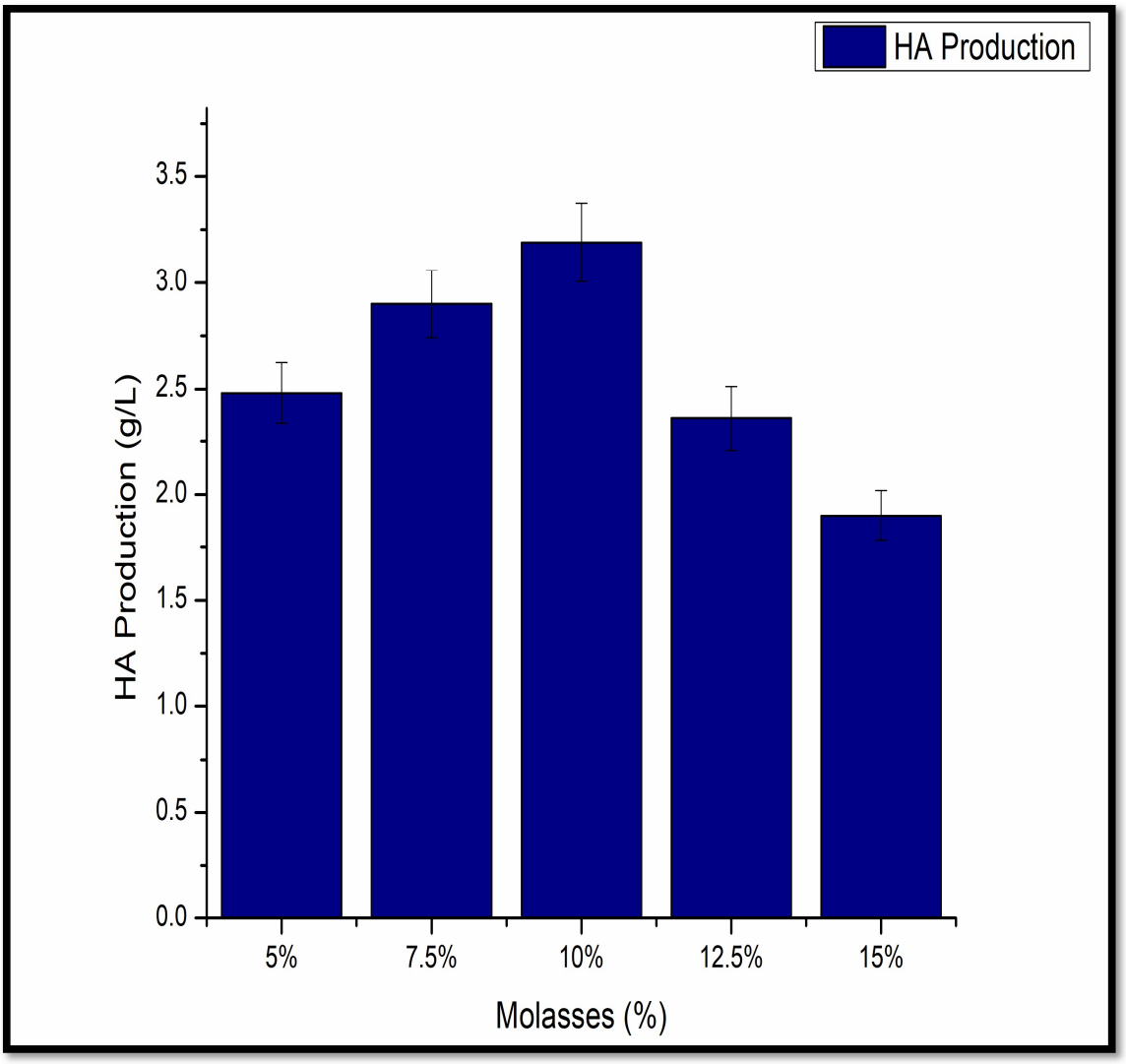

Figure 4.3. The effect of different molasses percentages on HA production and other factors were kept constant, pH 6.8, temperature 37˚C, and agitation at 100 rpm.

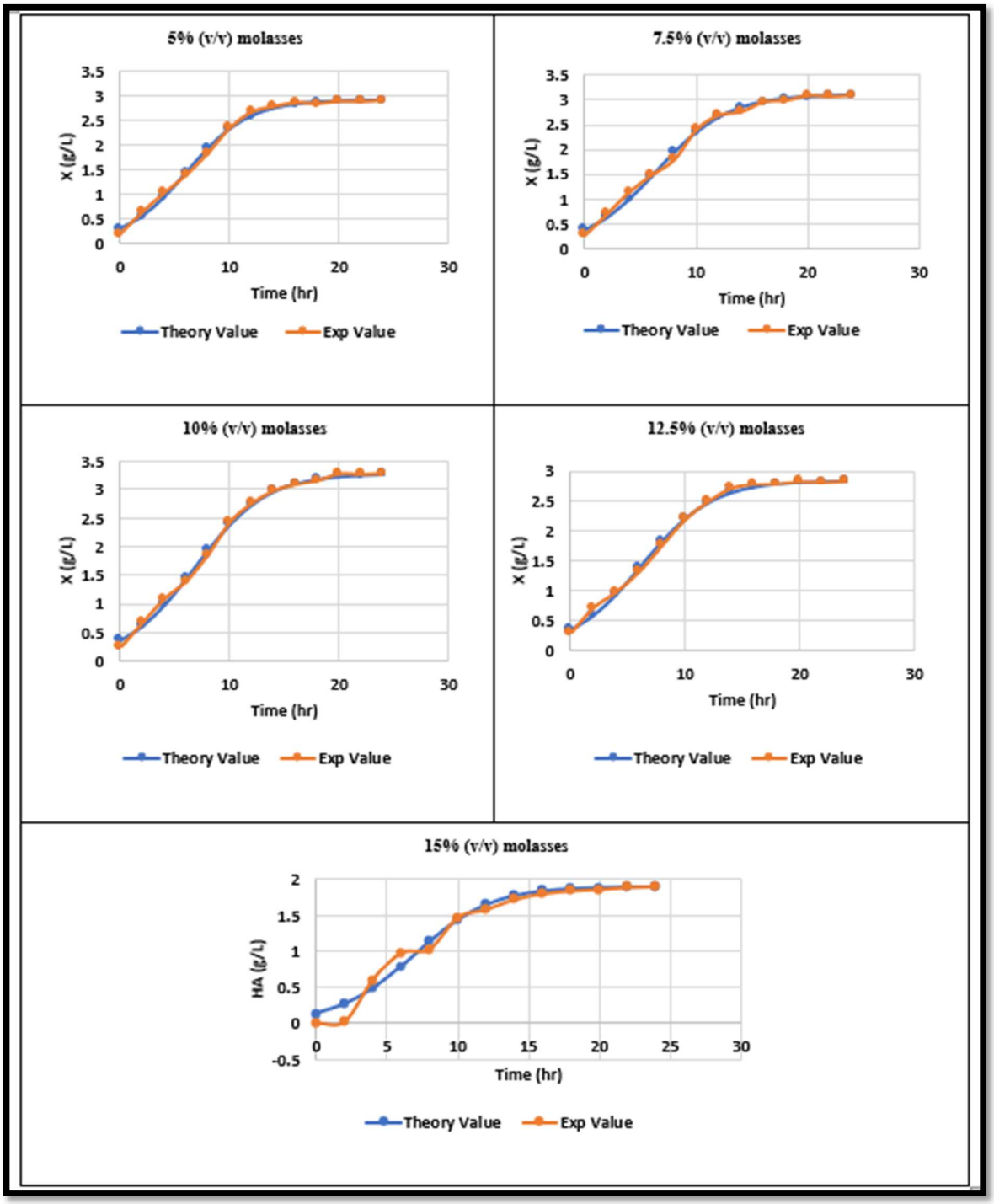

Figure 4.4. Graph representing the theoretical and experimental values of *S. zooepidemicus* MTCC 3523 cell biomass at different time intervals, to varying concentrations of molasses at pH 6.8, temperature 37˚C, and agitation at 100 rpm.

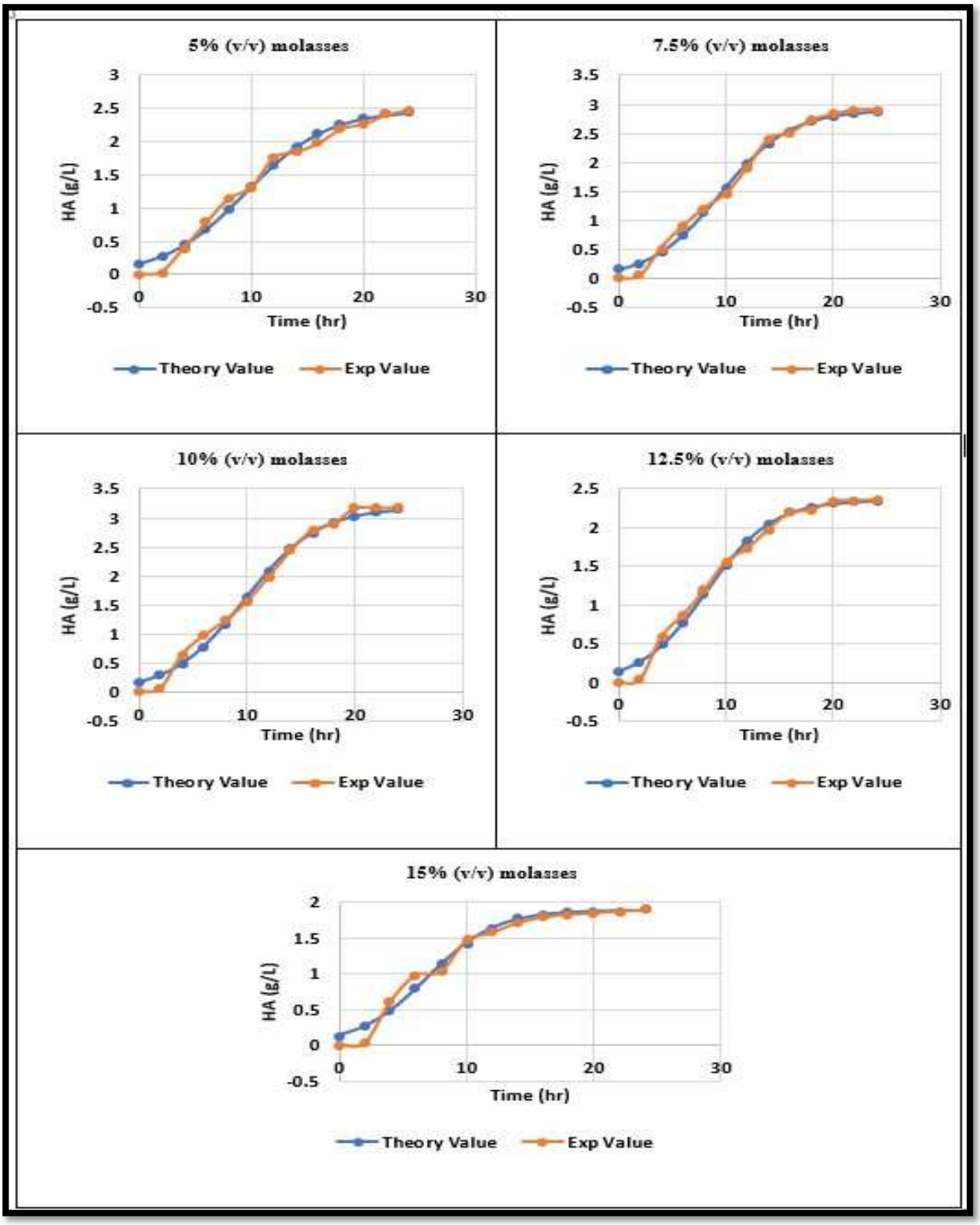

Figure 4.5. Graph representing the theoretical and experimental values of HA production from *S. zooepidemicus* at different time intervals, varying concentrations of molasses at pH 6.8, temperature 37˚C, and agitation at 100 rpm.

4.1.5. Effect of temperature, pH, and agitation

When hyaluronic acid is produced by fermentation using *S. zooepidemicus* as a producer microorganism, a drop in pH is seen, primarily due to the formation of lactic acid, which resulted in lower microbial biomass and impeded hyaluronic acid production (Liu et al., 2011a; Lu et al., 2016).

Thus, optimization of pH helps in promoting the fabrication of hyaluronic acid. The pH levels covering 6.0 to 8.0 were examined to see how effective they increased hyaluronic acid synthesis. When the pH was increased, HA production also increased to a certain level, and then a decrease was observed, with the pH becoming more alkaline. The best production was observed at pH 7 with a yield of 3.32 g/L, as shown in Figure 4.6.

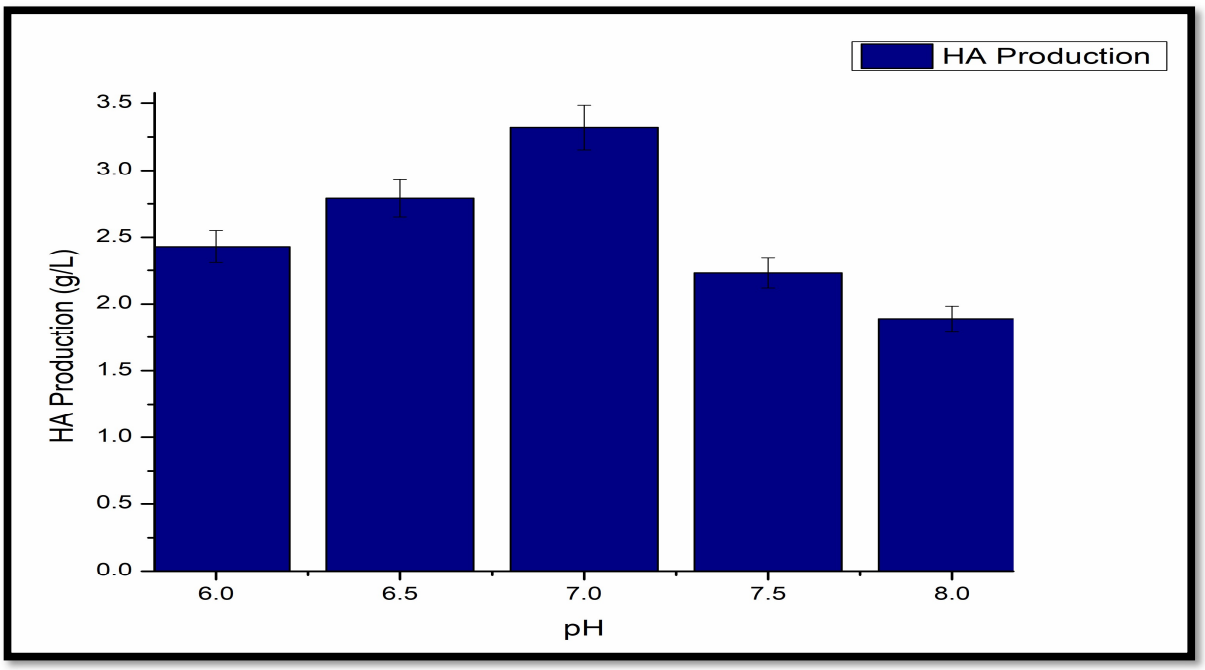

Figure 4.6. Effect of pH on HA production, temperature maintained at 37˚C, agitation 100 rpm.

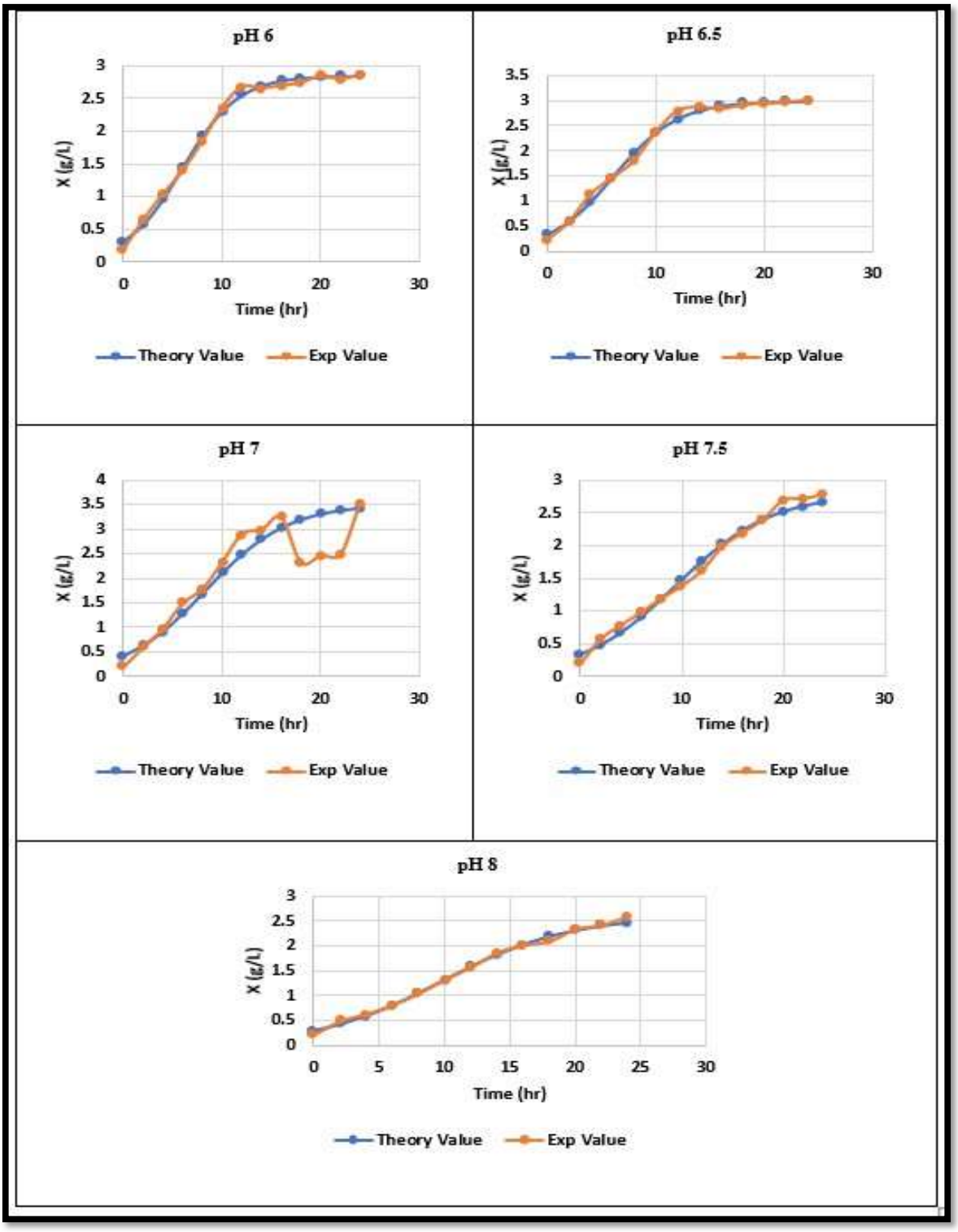

Figure 4.7. Graph representing the theoretical and experimental values of cell biomass of *S. zooepidemicus* at different time intervals, at different pH at 37˚C and agitation at 100 rpm.

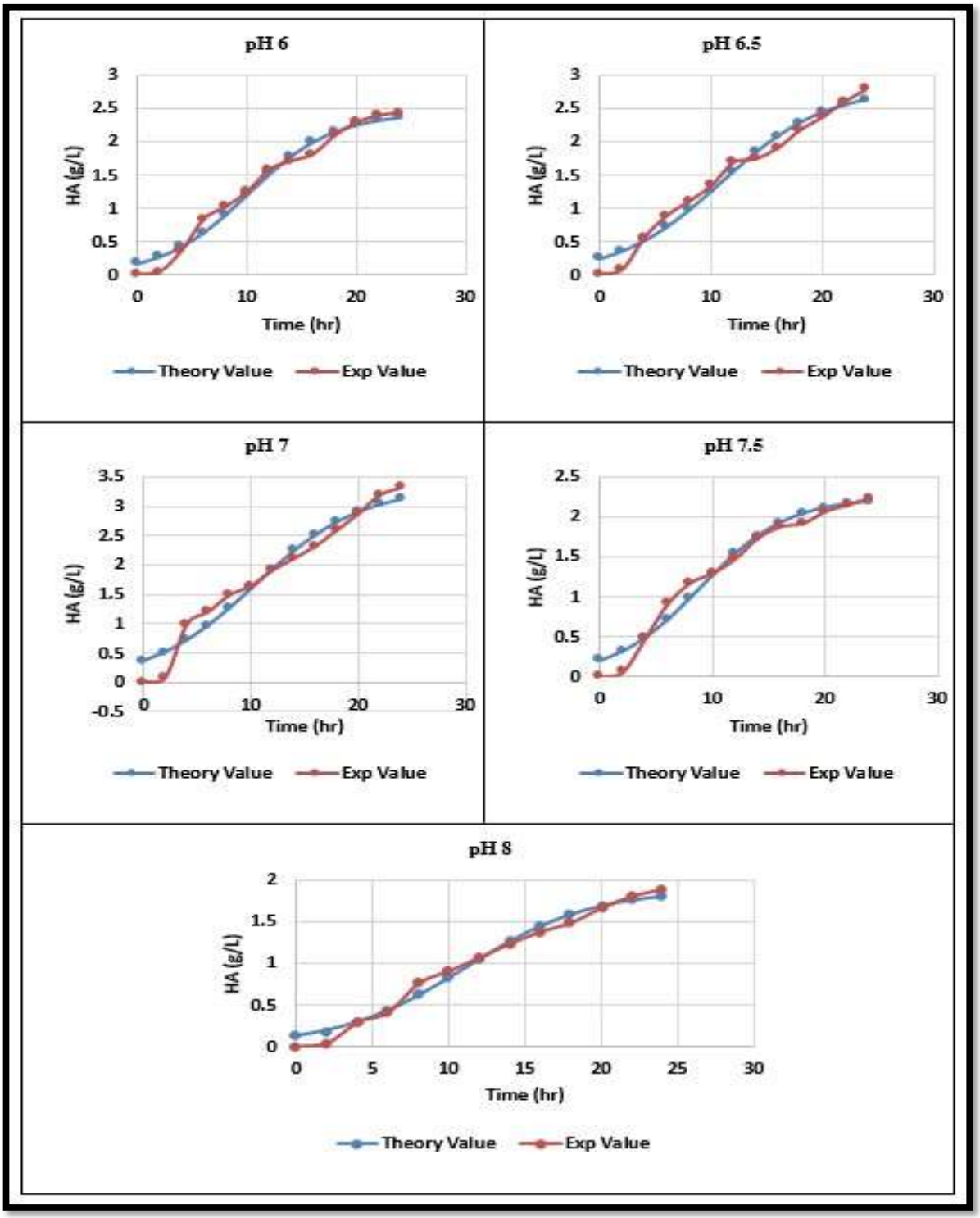

Figure 4.8. Graph representing the theoretical and experimental values of HA production from *S. zooepidemicus* MTCC 3523 at different time intervals, at different pH at temperature 37˚C and agitation at 100 rpm.

The impact of controlled pH on HA production was investigated using cultures at 100 rpm with or without controlled pH (data not shown). Cultivation amid regulated pH resulted in a massive increase in maximal HA production when correlated to non-regulated pH cultures with equal agitation rates. At 100 rpm and 37˚C temperature, the highest maximum HA output and cell biomass were recorded as 3.32 ± 0.16 and 3.51 ± 0.17 (Table 4.1) (Figure 4.7, 4.8), respectively. .Intracellular enzyme activity primarily depends on the medium's temperature; a remarkable temperature alteration can affect the microbe's growth and product synthesis (Vigetti et al., 2014). The effect of various temperatures was observed, and it was found that at 37˚C the microbial growth and HA synthesis both are at its maximum with a HA fabrication of 3.29 g/L as shown in figure 4.9. An increase in temperature caused minor damage to the cell biomass (Figure 4.10) as it started dropping, and HA production was affected (Figure 4.11, Table 4.1)

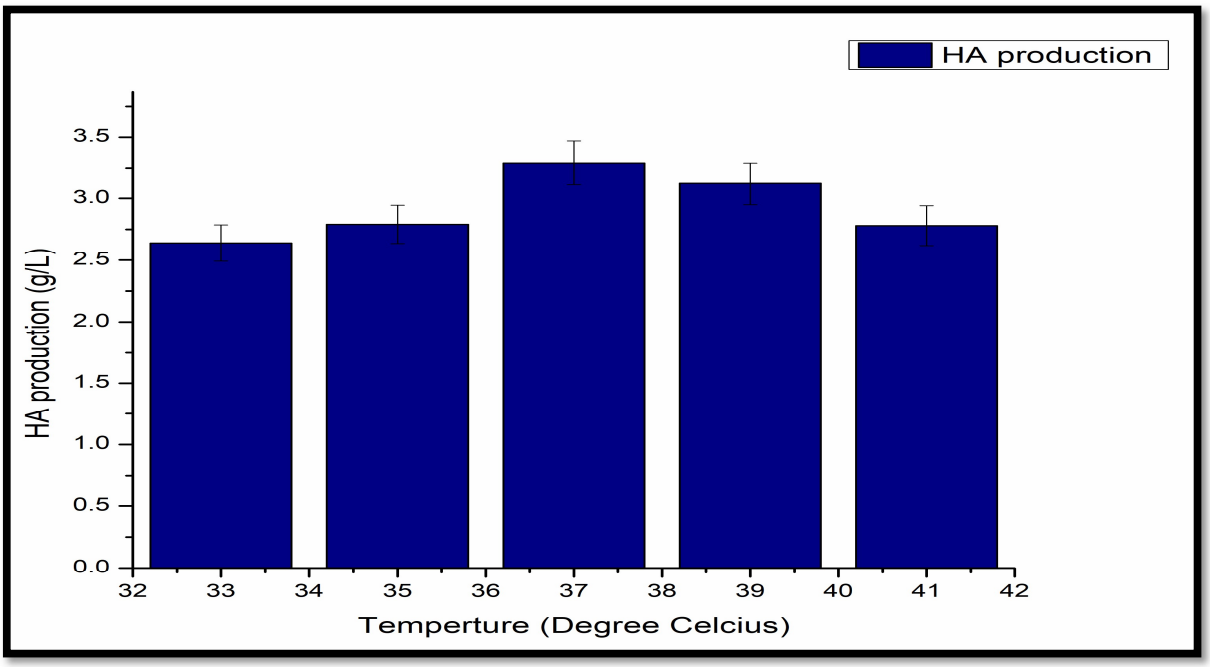

Figure 4.9. Impact of different temperature conditions on HA fabrication, pH maintained at 6.8 and agitation 100rpm

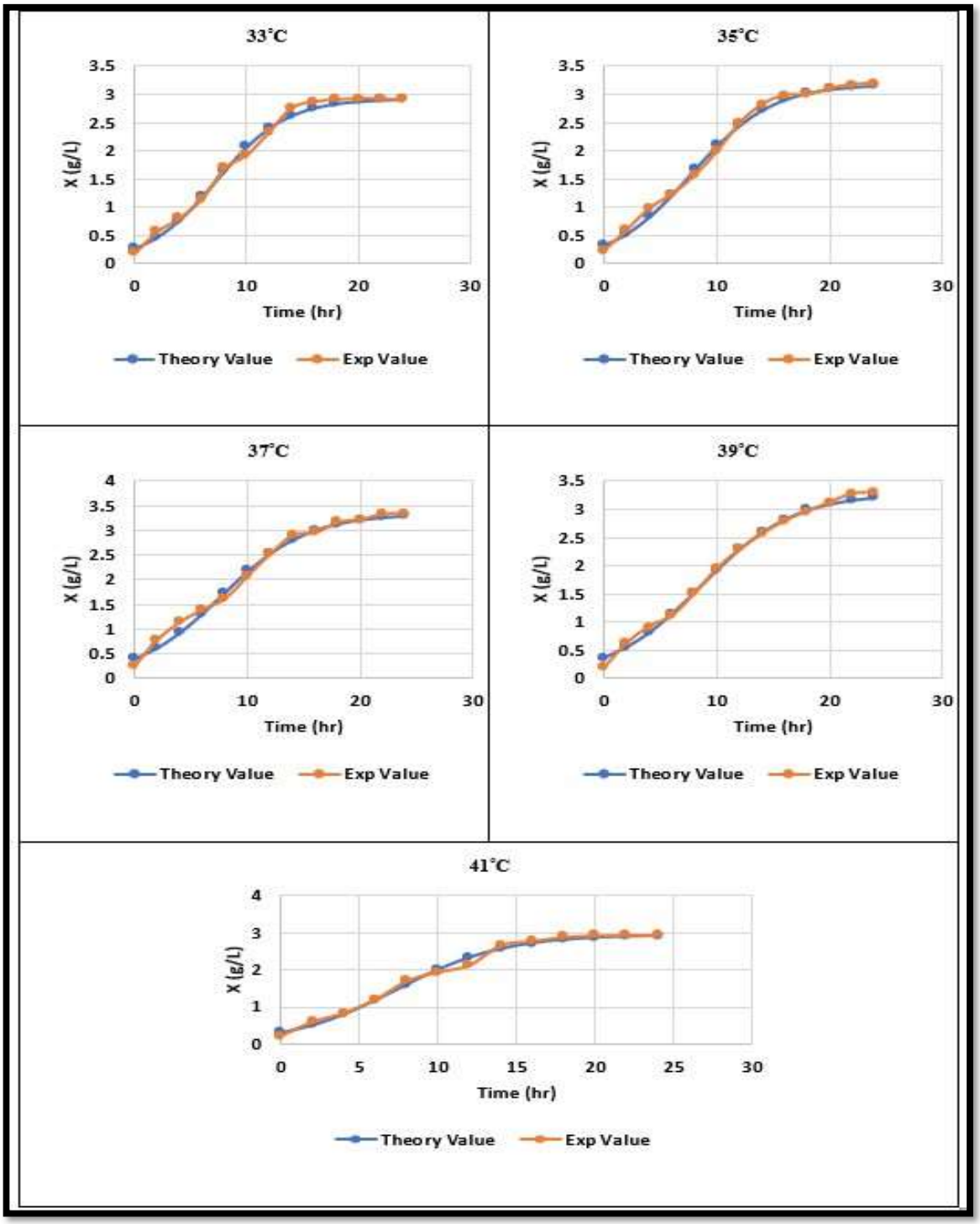

Figure 4.10. Graph representing the theoretical and experimental values of cell biomass of *S. zooepidemicus* at different time intervals, at a different temperature at pH 6.8, and agitation at 100 rpm.

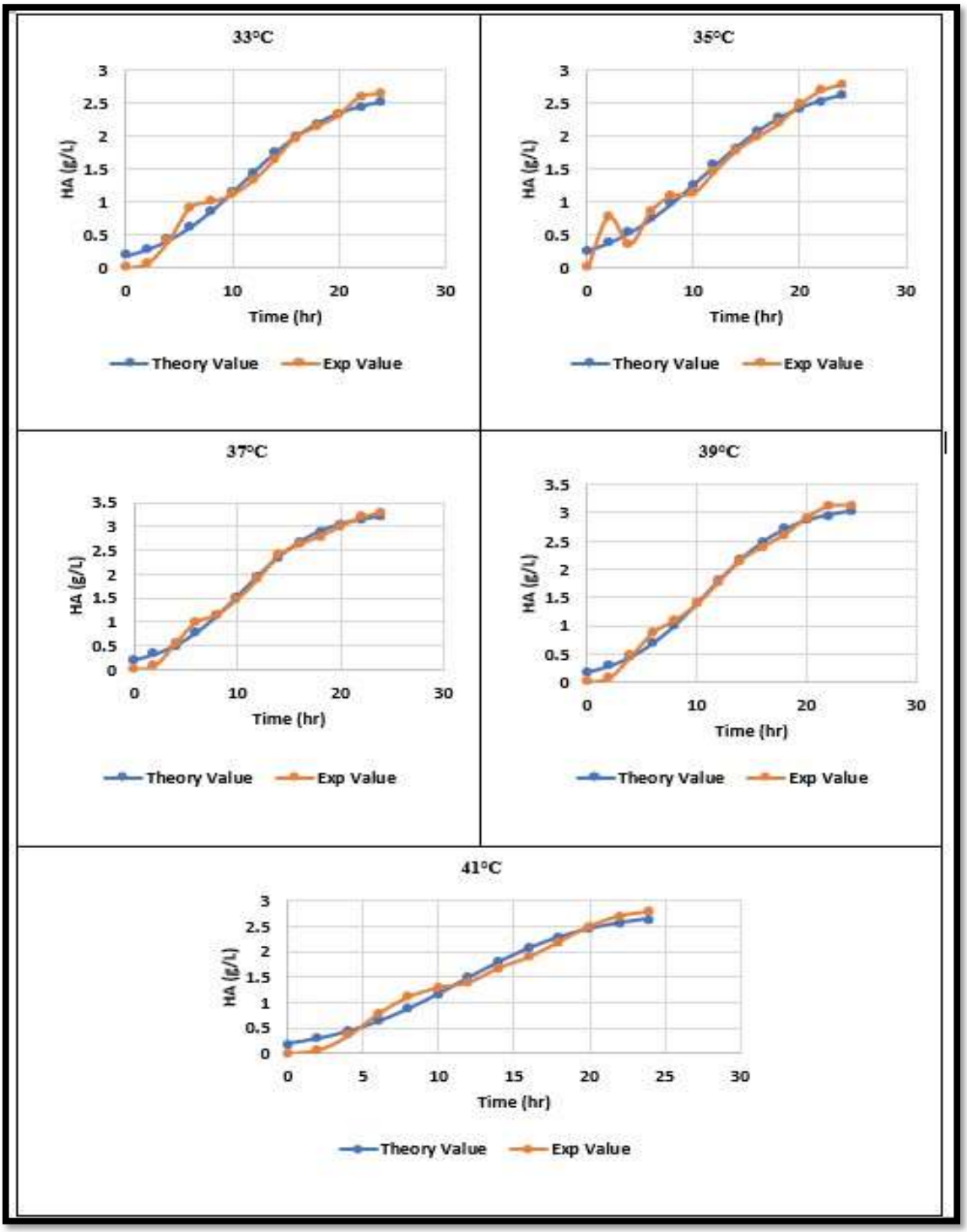

Figure 4.11. Graph representing the theoretical and experimental values of HA production from *S. zooepidemicus* at different time intervals, at a different temperature at pH 6.8, and agitation at 100 rpm.

Because the synthesis of HA raises the viscosity of the broth, oxygen mass transfer and agitation rates significantly impact HA fabrication (Liu et al., 2011a). Nevertheless, there seems to be no consensus on whether intense agitation boosts the generation of HA. In this context, it has been discovered in several investigations that increasing mixing speed reduces polysaccharide production rates (Kim et al., 1996), whereas others have observed the opposite (Johns et al., 1994). Although agitation is required to transfer nutrients and eliminate lactate from the cell's surroundings (Johns et al., 1994), increased agitation speeds might harm HA synthesis and the structure of the polymer (Johns et al., 1994). Different agitation rates have been experimented with to examine the influence of agitation on the fabrication of HA, as shown in Figure 4.12.

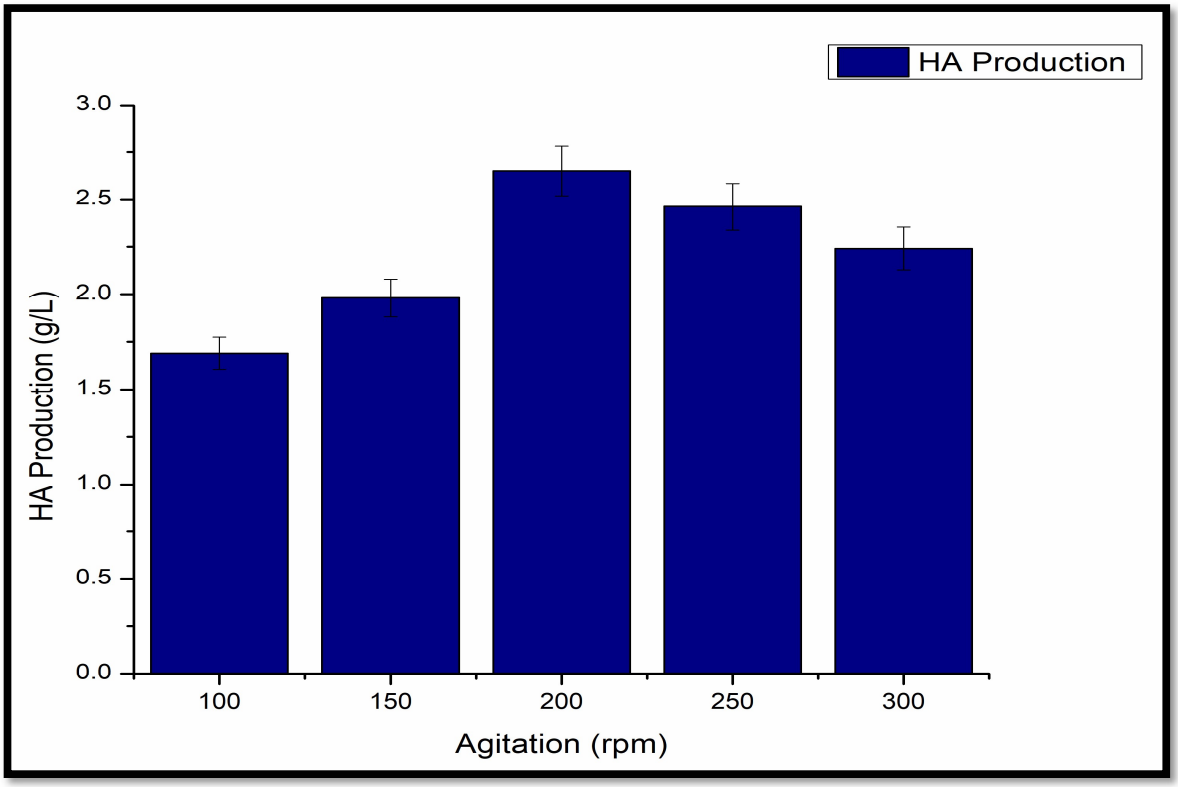

Figure 4.12. Impact of various agitation speed on HA fabrication, pH maintained at 6.8 and temperature 37˚C

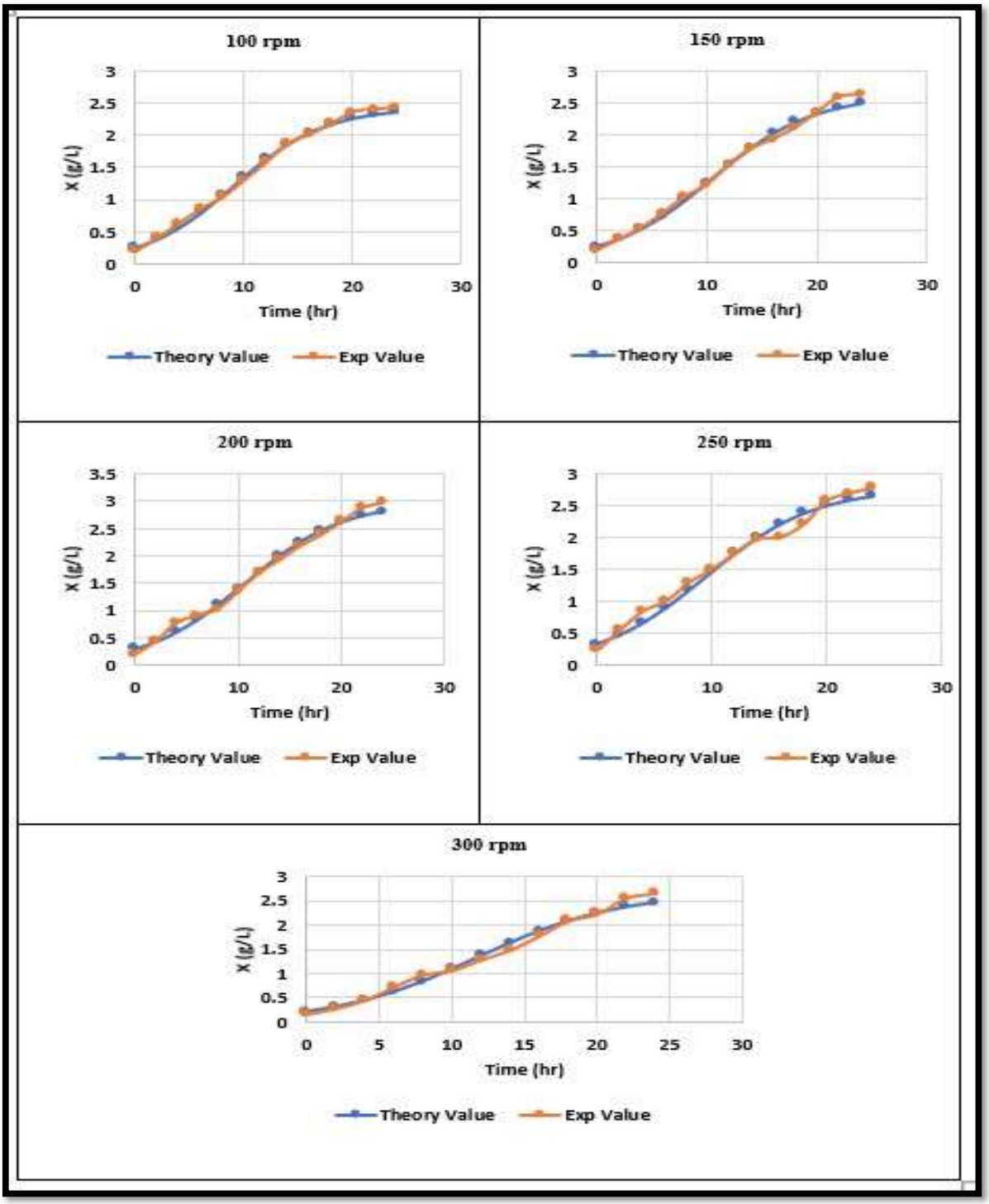

Figure 4.13. Graph representing the theoretical and experimental values of cell biomass of *S. zooepidemicus* at different time intervals, at different agitation rates at pH 6.8 and temperature 37˚C.

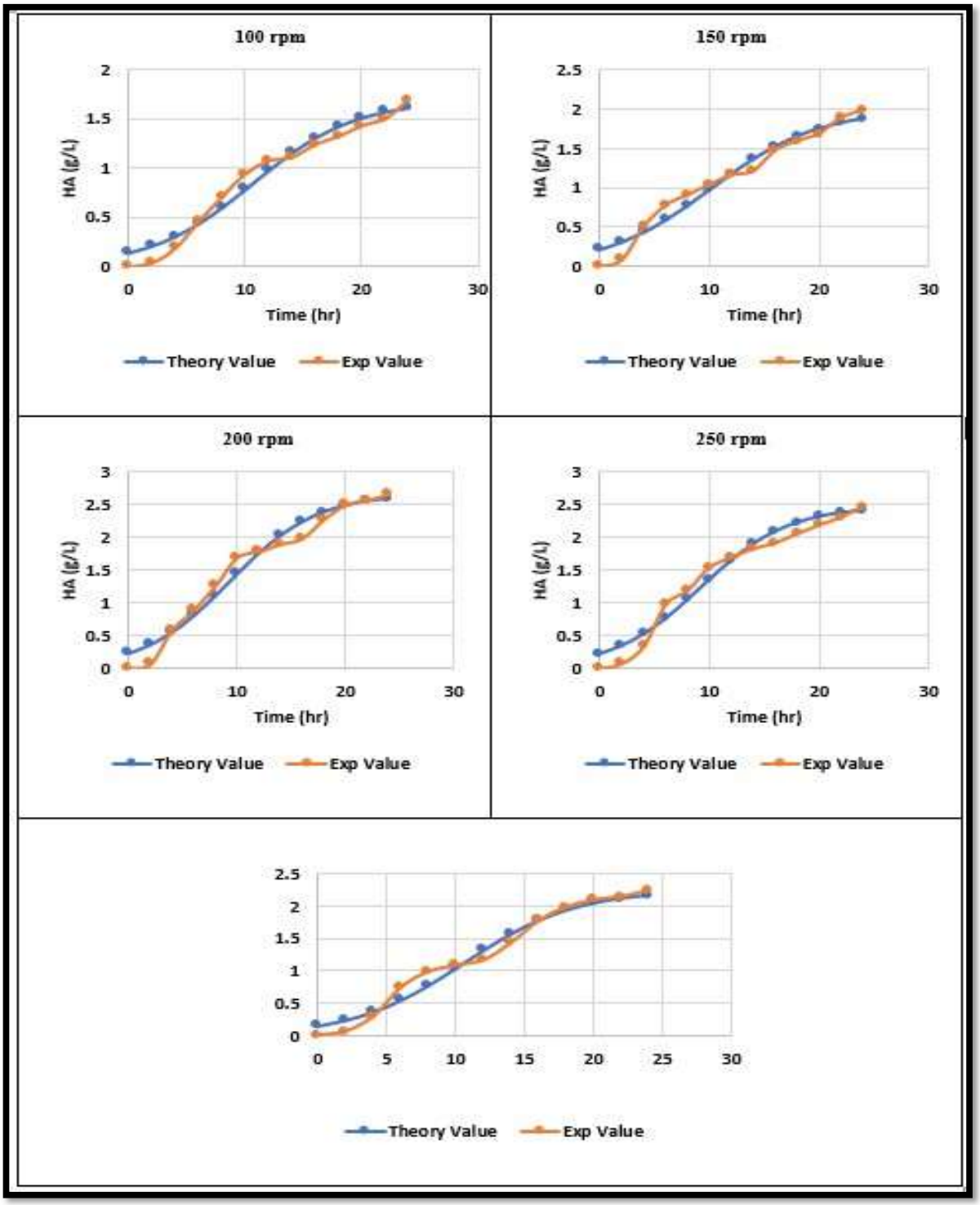

Figure 4.14. Graph representing the theoretical and experimental values of HA production from *S. zooepidemicus* at different time intervals, at different agitation rates at pH 6.8 and temperature 37˚C.

The impact of the agitation on the product yield is a little complicated (Boeriu et al., 2013). The agitation speed is closely interconnected to the heat and mass transfer in the fermentation broth, a high viscosity non-newtonian fluid. The viscosity here ranged between 0.59 to 0.67 pascal seconds. Agitation speed increased from 150 to 200; the maximum hyaluronic acid production was achieved with the production of 2.65 g/L. The yield dropped slightly when the agitation speed was further enhanced to 250 rpm.

The higher agitation speed may result in high shear stress that might cause damage to the microbial cell; cell biomass was affected (Figure 4.13) and directed towards hyaluronic acid degradation (Duan et al., 2008). Indeed, it was found that the agitation rate was raised from 100 to 300 rpm, and a significant decrease in HA production was observed after 200 rpm (Table 4.1, Figure 4.14).

Table 4.1. Results of non-linear adjustment of biomass (X) and hyaluronic acid (HA) time courses in cultivating *S. zooepidemicus* under different conditions. X_m, maximum biomass; HA_m, maximum hyaluronic acid production; V, maximum hyaluronic acid production rate; $\boldsymbol{\lambda}$ (h) lag phase of hyaluronic acid production. The table also shows yields of hyaluronic acid on biomass ($Y_{H/X}$) calculated using Eq. (3-10, in materials and methods). The determination coefficients (R^2) and p-values from Fisher's F-test for the mathematical are shown.

Variables	**Variations**				
	Agitation (rpm)				
Hyaluronic Acid	**100**	**150**	**200**	**250**	**300**

HA_m(g/l)	1.69 ± 0.08	1.98 ± 0.09	2.65 ± 0.13	2.46 ± 0.12	2.24 ± 0.11
V (g/lh)	0.09 ± 0.004	0.1006 ± 0.005	0.16 ± 0.008	0.15 ± 0.007	0.13 ± 0.006
λ (h)	1.87 ± 0.09	0.32 ± 0.01	1.22 ± 0.06	1.24 ± 0.06	2.49 ± 0.12
$Y_{h/x}$ (g g-1)	0.62 ± 0.03	0.87 ± 0.04	1.02 ± 0.05	0.92 ± 0.04	0.97 ± 0.04
p-value	<0.001	<0.001	<0.001	<0.001	<0.001
r (obs-pred)	0.98	0.97	0.98	0.98	0.98
Biomass					
X_m(g/l)	2.43 ± 0.12	2.63 ± 0.13	2.98 ± 0.14	2.78 ± 0.13	2.65 ± 0.13
V (g/lh)	0.14 ± 0.07	0.14 ± 0.007	0.15 ± 0.007	0.14± 0.007	0.13 ± 0.006
λ (h)	0.60 ± 0.003	1.22 ± 0.06	0.93 ± 0.04	1.02 ± 0.005	2.05 ± 0.1
p-value	<0.001	<0.001	<0.001	<0.001	<0.001
r (obs-pred)	0.99	0.99	0.99	0.98	0.99
Molasses					
Hyaluronic Acid	**5%**	**7.5%**	**10%**	**12.5%**	**15%**

HA_m(g/l)	2.48 ± 0.12	2.9 ± 0.14	3.19 ± 0.15	2.36 ± 0.11	1.9 ± 0.09
V (g/lh)	0.17 ± 0.008	0.22 ± 0.01	0.23 ± 0.01	0.19 ± 0.009	0.17 ± 0.008
λ (h)	2.28 ± 0.11	2.98 ± 0.14	2.99 ± 0.14	2.06 ± 0.1	1.55 ± 0.07
$Y_{h/x}$ (g g-1)	0.63 ± 0.03	0.74 ± 0.03	0.77 ± 0.03	0.73 ± 0.03	0.69 ± 0.03
p-value	<0.001	<0.001	<0.001	<0.001	<0.001
r (obs-pred)	0.99	0.99	0.99	0.99	0.98
Biomass					
X_m(g/l)	2.91 ± 0.14	3.1 ± 0.15	3.3 ± 0.16	2.84 ± 0.14	2.84 ± 0.14
V (g/lh)	0.25 ± 0.01	0.24 ± 0.01	0.25 ± 0.01	0.22 ± 0.01	0.22 ± 0.01
λ (h)	0.42 ± 0.02	0.49 ±0.02	0.29 ± 0.01	0.39 ± 0.01	0.38 ± 0.01
p-value	<0.001	<0.001	<0.001	<0.001	<0.001
r (obs-pred)	0.99	0.99	0.99	0.99	0.98
pH					
Hyaluronic Acid	**6**	**6.5**	**7**	**7.5**	**8**

HA_m(g/l)	2.43 ± 0.12	2.79 ± 0.13	3.32 ± 0.16	2.23 ± 0.11	1.89 ± 0.09
V (g/lh)	0.15 ± 0.007	0.14 ± 0.007	0.16 ± 0.008	0.14 ± 0.11	0.11 ± 0.005
λ (h)	2.20 ± 0.11	1.50 ± 0.07	0.51 ± 0.02	1.13 ± 0.05	2.7 ± 0.13
$Y_{h/x}$ (g g-1)	0.60 ± 0.03	0.66 ± 0.03	0.84 ± 0.04	0.83 ± 0.04	0.68 ± 0.03
p-value	<0.001	<0.001	<0.001	<0.001	<0.001
r (obs-pred)	0.98	0.98	0.97	0.98	0.99
Biomass					
X_m(g/l)	2.85 ± 0.14	2.99 ± 0.14	3.51 ± 0.17	2.78 ± 0.13	2.59 ± 0.12
V (g/lh)	0.25 ± 0.01	0.25 ± 0.01	0.21 ± 0.01	0.14 ± 0.007	0.13 ± 0.006
λ (h)	0.29 ± 0.01	0.27 ± 0.01	0.11 ± 0.005	0.060 ± 0.003	0.18 ± 0.009
p-value	<0.001	<0.001	<0.001	<0.001	<0.001
r (obs-pred)	0.99	0.99	0.90	0.99	0.99
Temperature (°C)					
Hyaluronic Acid	**33**	**35**	**37**	**39**	**41**
HA_m(g/l)	2.64 ± 0.13	2.79 ± 0.13	3.29 ± 0.16	3.12 ± 0.15	2.78 ± 0.13

V (g/lh)	0.15 ± 0.007	0.14 ± 0.007	0.21 ± 0.01	0.20 ± 0.01	0.15 ± 0.007
λ (h)	2.52 ± 0.12	1.26 ± 0.06	3.01 ± 0.15	3.18 ± 0.15	2.67 ± 0.13
$Y_{h/x}$ (g g-1)	0.67 ± 0.03	0.79 ± 0.03	0.84 ± 0.04	0.78 ± 0.03	0.69 ± 0.03
p-value	<0.001	<0.001	<0.001	<0.001	<0.001
r (obs-pred)	0.98	0.98	0.99	0.99	0.98
Biomass					
X_m(g/l)	2.93 ± 0.14	3.19 ± 0.15	3.35 ± 0.16	3.29 ± 0.16	2.94 ± 0.14
V (g/lh)	0.23 ± 0.01	0.22 ± 0.01	0.21 ± 0.01	0.20 ± 0.01	0.21 ± 0.01
λ (h)	0.96 ± 0.04	0.556 ± 0.02	0.12 ± 0.005	0.36 ± 0.01	0.43 ± 0.02
p-value	<0.001	<0.001	<0.001	<0.001	<0.001
r (obs-pred)	0.99	0.99	0.99	0.99	0.99

By using logistic equations (1) and (2), the experimental data (biomass: X and hyaluronic acid: H) were quantified and modeled. Higher R^2-values indicate excellent agreement between theoretical and empirical data (Table 4.1). The Fisher's F-test p-values demonstrated that the models adequately accounted for the experimental data. For all conditions analyzed (Student's t-test, Table 4.3), the kinetic parameters described by equations (3)–(10) were statistically significant.

4.1.6. Optimization of HA concentration by RSM

In the current analysis, Central Composite Design (CCD) of a two-level four factors were bought in to work to escalate HA production. The borderlines of these tentative frameworks were picked up on the footing of lonesome criterion selection probation. The computative interpretation of HA production is given by:

$$Y = -52.8 + 0.311A + 3.652B - 4.07C + 0.0159D - 0.04093A^2 - 0.07708B^2 - 0.438C^2 - 0.000094D^2 - 0.00400AB + 0.0860AC + 0.000380AD + 0.2663BC + 0.001187BD - 0.00365CD$$

A represents molasses, B represents temperature, C represents pH, and D represents agitation rate. According to regression analysis of empirical data, molasses exhibits positive synergic analysis with all determinants (Table 4.2).

ANOVA of the quadratic equation for HA fabrication was exemplified in table 2. Because the model has a P-value of 0.001, it is expected to be evincible. The model is evincive, as evidenced by the high values of the determination coefficient (R^2 = 94.56 percent) and the adjusted determination coefficient (adjusted R^2= 89.80 percent). Figure 4.15 shows the RSM plots that show the effects of the pairwise amalgamation of the four components.

The graphs in Figure 4.15 clearly show how any two factors interacted to influence the response.

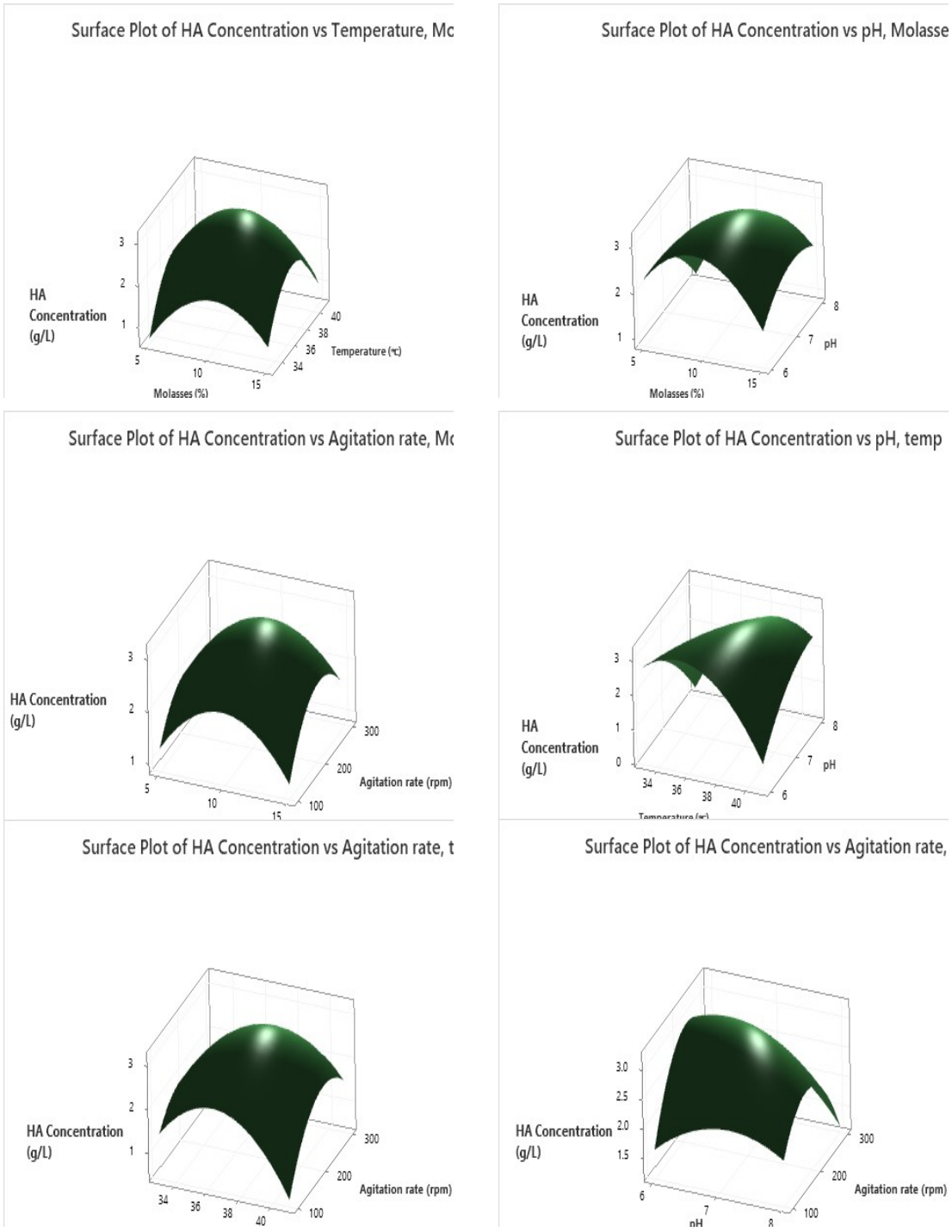

Figure 4.15. Response Surface Plots for the correlative impacts of various factors on the production of hyaluronic acid.

Table 4.2. Experimental design and results information by RSM using CCD

S. No	Molasses	Temp	pH	Agitation Rate	Experimented HA	Predicted HA
1	15	34	8	300	2.54	2.62
2	15	40	8	300	2.56	2.53
3	5	40	6	100	2.14	2.10
4	10	37	7	200	3.19	3.18
5	15	40	8	100	2.90	2.78
6	15	34	6	100	2.19	2.17
7	5	34	8	100	3.10	3.09
8	10	37	7	100	3.22	3.14
9	10	34	7	200	3.29	3.45
10	5	34	8	300	3.00	2.83
11	10	37	8	200	3.03	3.07
12	15	34	8	100	2.95	2.99
13	10	37	7	200	3.33	3.18

14	10	40	7	200	3.11	3.04
15	5	40	6	300	2.36	2.28
16	15	34	6	300	2.24	2.12
17	10	37	7	300	2.99	3.04
18	10	37	7	200	3.08	3.18
19	15	37	7	200	2.88	2.85
20	10	37	6	200	2.73	2.66
21	10	37	7	200	3.13	3.18
22	5	34	6	100	2.58	2.57
23	5	40	8	300	2.22	2.27
24	15	40	6	100	2.03	2.16
25	5	40	8	100	2.34	2.42
26	10	37	7	200	3.16	3.18
27	5	34	6	300	2.49	2.64
28	15	40	6	300	2.18	2.22
29	10	37	7	200	3.07	3.18

30	10	37	7	200	3.25	3.18
31	10	37	7	200	3.20	3.18

ANOVA of response surface plots

Using 3-D surface plots, the equipped polynomial equation was expressed in order to visualize the variation of the responses resulting from the combined effects of the determinants. The impacts of molasses, temperature, pH, and agitation rate on each other were studied with all of the synergistic studies, making it possible that molasses played a role in the manufacturing process. Table 4.3 depicts the RSM model's ANOVA analysis.

The ANOVA analysis yielded a better-than-average score for HA production. The greatest projected generation of HA was 3.45 g/L at 9.74 percent molasses, 36.2°C, pH 6.46, and a 207rpm agitation rate. Experiments were run in triplicates to ensure that the results were accurate.

Empirically, the maximum HA production was found to be 3.36 g/L near it. Lactic acid produced during the initial production process of 26.32 g/L was reduced by up to 40% after optimizing the HA production process.

Table 4.3. The ANOVA analysis of the Response surface model

Source	**DF[a]**	**Adj SS[b]**	**Adj MS[c]**	**F**	**P**
Regression	14	7.27	0.51	19.87	<0.001
Linear	4	0.39	0.09	3.74	0.025

Square	4	5.16	1.29	49.37	<0.001
Interaction	6	1.72	0.28	10.96	<0.001
Residual error	16	0.41	0.02		
Lack of fit	10	0.31	0.03	1.84	0.23
Pure error	6	0.10	0.01		
Total	30	7.69			

[a] Degree of Freedom

[b] Sum of Square

[c] Mean of Square

The production of HA in a previously defined medium with glucose as a carbon source was replaced with agricultural waste cane molasses. Different production conditions were tested by varying the pH, temperature, and agitation rates, one at a time. Different concentrations of molasses were also tried for enhanced and better HA yield. When comparing the productivity with the molasses and the glucose, the overall productivity was improved with a final result of 3.36 g/L. As reported, molasses contains different kinds of sugar. Sucrose is the primary sugar. A potent inhibition in the growth of *S. zooepidemicus* can be observed when the concentration of molasses is reported after a certain extent earlier (Liu et al., 2008a). The inhibition of *S. zooepidemicus* growth in media containing molasses must be related to other components of this byproduct, such as lactic acid (Liu et al., 2008a)and phenolic compounds (Takara et al., 2007), which have been known to be *Streptococci* inhibitors. Further molasses

pre-treatment using an activated carbon resin to remove inhibiting chemicals and improve HA titer helped in better HA production.

According to Jagannath and Ramachandra, replacing glucose with sucrose boosted HA productivity, molecular weight, and the rate of specific HA synthesis (Jagannath & Ramachandran, 2010). Molasses, the combination of different sugars, has been used in studies earlier as a carbon source for HA production with different medium compositions (Amado et al., 2017) and suggested that molasses is a better carbon source than glucose (Duffeck et al., 2020).

4.2. Impacts of aeration and agitation rates on oxygen transfer coefficient

Analyses of the DO uptake rate (OUR) and oxygen transfer (OTR) into the fermentation medium are necessary because oxygen plays a crucial role in microbial development and metabolism. To determine the k_La values, the fermentations of *S. zooepidemicus* were accomplished at bench scale by changing the agitation (150, 200, 250, and 300 rpm) and aeration rate (0.5, 1.0, 1.5, and 2 vvm).

4.2.1. Impact of agitation and aeration on DOT

S. zooepidemicus was used to study how aeration affected the synthesis of HA. The fermentation process was maintained in a bench-size bioreactor for 28 h to assess the impact of the aeration rate. The aeration rate of the fermentation system was maintained using a rotameter ranging from 0.5 vvm to 2 vvm. Figure 4.16 (A) demonstrates how all dissolved oxygen levels across all aeration rates drastically dropped to a minimal level and were maintained at 20–35% throughout.

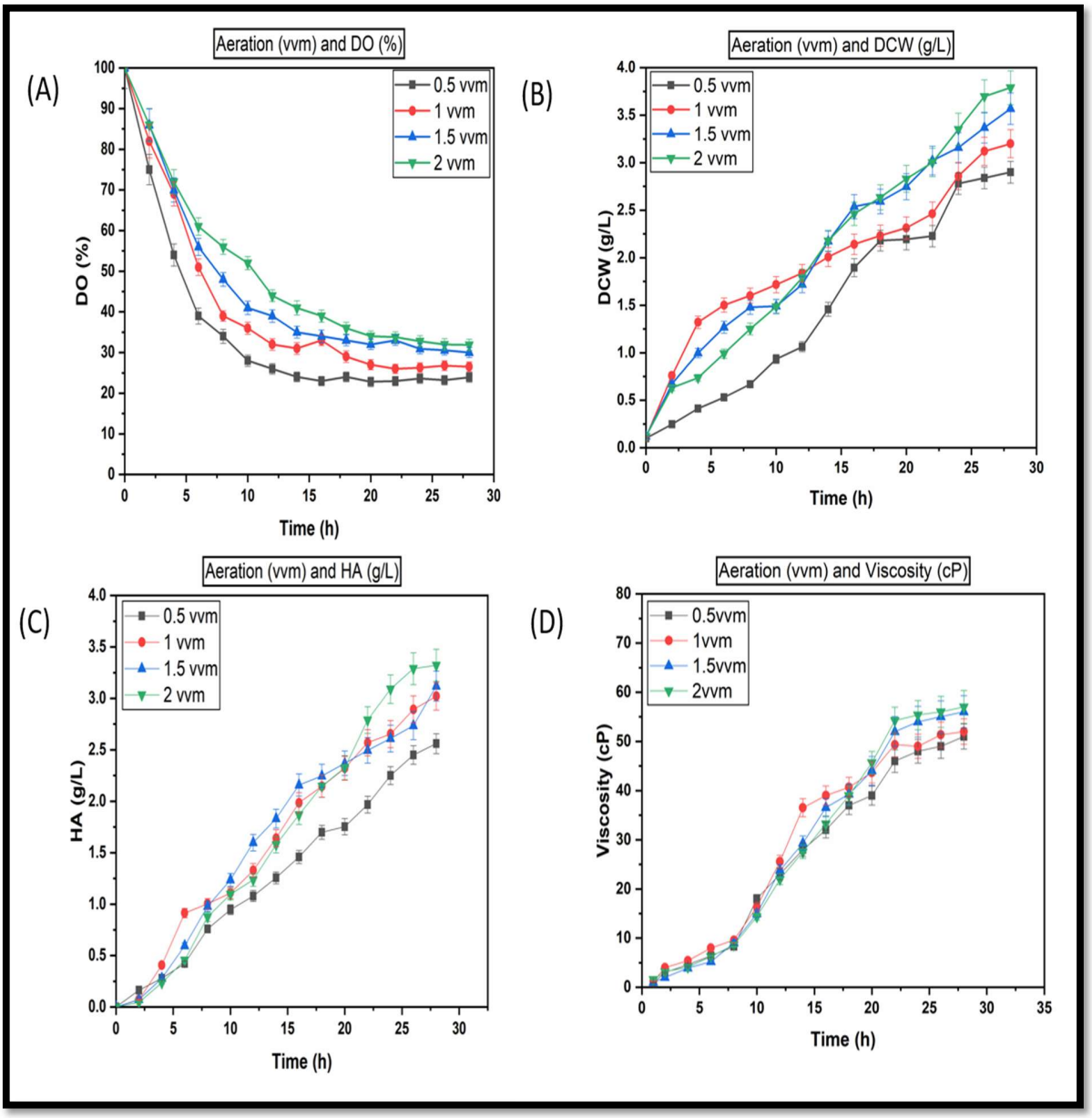

Figure 4.16. Impact of aeration rate on (A) dissolved oxygen tension, (B) dry cell weight, (C) hyaluronic acid production and, (D) viscosity during cultivation of *S. zooepidemicus* at 37 ºC and pH 7.

The percentage of dissolved oxygen increased at higher aeration rates. However, the dissolved oxygen levels in every experiment were never lower than 15%, showing ample

oxygen available for cell use. High and low aeration levels affect oxygen retention duration, corresponding to the broth's gas velocity. As well as supplying oxygen for cell growth, aeration removes exhaust gases produced during fermentation in bioreactors. Oxygen is necessary for microbial development in aerobic fermentation, but too much oxygen can harm some microorganisms. It is ideal for the pace of dissolved oxygen supply to match the rate of oxygen demand.

The amount of oxygen flow retained in the broth will be impacted only by the amount of aeration (as oxygen support); at both low and high rates, aeration will decrease or increase gas velocity in the broth. Air bubble distribution and mixing are both affected by the agitation of the system. Instead of using aerated-only containers, which may not be sufficient to induce the liquid turbulence required for forming tiny air bubbles, mechanically agitated aerated vessels are frequently utilized. Although agitation could keep dissolved oxygen in the fermenter, improper agitation speed leads to poor oxygen transfer, especially in highly viscous broth. It was found that DO concentrations were dramatically reduced to a critical point when the agitation rate was varied during the production of HA using *S. zooepidemicus*. The DO values initially decreased until 10 h of cultivation and afterward kept at 15 to 40%. Figure 4.17 (A) represents the impact of agitation rates on DO concentration. The DO values did not depend on agitation rates. However, agitation affects the system's mixing and dispersion of air bubbles. Aerated alone vessels, which may not be sufficient to induce the liquid turbulence required to create tiny air bubbles, are rarely employed in place of mechanically agitated aerated vessels. Even though the agitation might keep the fermenter’s DO levels stable, it causes poor oxygen transport, especially in broths with a high viscosity. DO diffusion into viscous broth was prevalent at both low and high speeds.

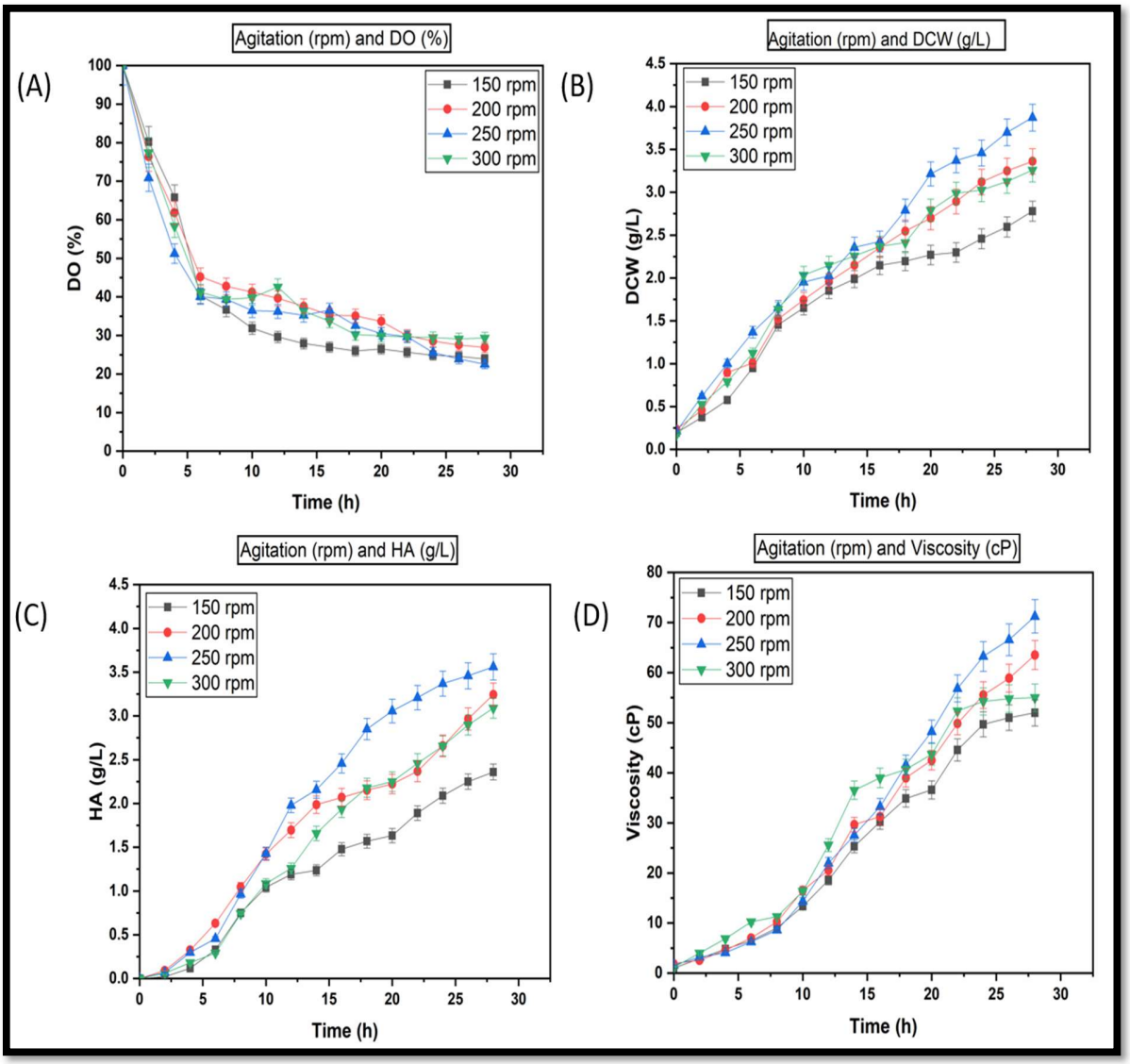

Figure 4.17. Impact of agitation rate on (A) dissolved oxygen tension, (B) dry cell weight, (C) hyaluronic acid production, and (D) viscosity during cultivation of *S. zooepidemicus* at 37 ºC and pH 7.

4.2.2. Impact of agitation and aeration on DCW

One of the critical determinants for the development of cultured microorganisms is the availability of oxygen in the broths, which can also be crucial for the expansion of aerobic biosynthetic systems. The biomass of *S. zooepidemicus* cells as dry cell weight was also

measured for all experiments. The DCW of the cells was also escalated when the aeration rate increased (2.94 ± 0.11, 3.25 ± 0.02, 3.56 ± 0.02, and 3.78 ± 0.1 g/L respectively at 0.5, 1.0, 1.5, and 2.0 vvm). Figure 4.16 B shows the impact of aeration on DCW. Therefore, the influence of aeration rates on DCW is favorable. The amount of oxygen in the culture should have been sufficient to meet the needs of the tested microorganism. Still, it may be provided at a greater concentration if it does not impact the micro-organism and is not harmful when oxygen concentrations are too high.

Therefore, it should be no surprise that *S. zooepidemicus* maximal growth and HA production were reported at 2.0 vvm. The bioreactor's capacity to meet microbial cells' oxygen demand determines the diffusion rate and oxygen solubility into the broths. Excessive biomass concentrations may affect growth and oxygen transfer by lowering oxygen solubility in the medium.

The impact of agitation rate on biomass during HA production was investigated (Figure 4.17 B). The observed DCW was 2.78 ± 0.21 g/L, 3.36 ± 0.12 g/L, 3.87 ± 0.12 g/L, and 3.25 ± 0.01 g/L at 150 rpm, 200 rpm, 250 rpm, and 300 rpm, respectively. At a high rate of agitation, the DCW drops. At 250 rpm, the most incredible DCW value, 3.87 ± 0.12 g/L, was recorded. However, mixing effects and shear force caused the DCW to decrease at more incredible speeds. Shear rate is among the most crucial variables in the layout of an aerobic fermenter for viscous non-Newtonian processes.

Oxygen transmission is permanently reduced by vigorous mixing at high agitation speeds, which inhibits cell growth and activity. A high rate of agitation led to heterogeneous mixing, which caused some developing cells to detach from the medium and adhere to the glass

vessel walls. Heterogeneous mixing (inadequate mixing) resulted from the broth being agitated too quickly during the first exponential phase; as a result, some bacterial cells attached to the glass vessel walls above the broth and detached from the media. This was not the case during the late exponential phase, presumably because of the broth's increased viscosity. High shear rates impact oxygen transport and cell activity. Violent mixing at high agitation rates always reduces oxygen transport, which hinders cell activity and growth.

When the circumstances are viscous, aeration and agitation should be changed at various rates to provide higher yields. In non-Newtonian broths, the blocking effect and biomass coalescence have been shown to be countered by aeration with optimum turbulence agitation (Galaction et al., 2004).

Biomass may reduce the solubility of oxygen in medium, particularly surface aeration, and block agitation and aeration systems, negatively affecting growth and oxygen transfer. Studies have shown that surface aeration contributes 15-20 times less oxygen transfer during varied bacterial fermentations than it does for viscous broths without biomass.

4.2.3. Impact of agitation and aeration on HA production

In the present study, HA production increases when the aeration rate increased, which was observed at 2.56 ± 0.01 g/L, 3.02 ± 0.02 g/L, 3.12 ± 0.01 g/L, and 3.32 ± 0.02 g/L respectively at 0.5, 1.0, 1.5, and 2 vvm. The impact of aeration on HA generation is depicted in Figure 4.16 C. The maximum HA yield (3.32 ± 0.02 g/L) and dry cell weight (3.78 ± 0.10 g/L g/L) were monitored at 2.0 vvm. It may be because oxygen transport to bacterial cells significantly impacts HA formation by altering metabolic fluxes and pathways.

As a result, the effectiveness of the bioreactor and microbial physiology determine oxygen transport in a fermenter. The results of DCW values were extrapolated after increasing the aeration and agitation rates. In this example, Cell growth correlates with product production, with significant growth leading to outstanding production. When oxygen is transferred into microbial cells, this influences metabolic pathways and changes metabolic fluxes, affecting product formation (Çalık et al., 2000). As a result, the effectiveness of the bioreactor and microbial physiology determine oxygen transport in a fermenter.

The effect of agitation rate during HA production was investigated, and the maximum HA yield of 3.56 ± 0.01 g/L was found to be monitored at the agitation of 250 rpm. The range of variation in agitation was 150 rpm to 300 rpm. Shearing and mixing may be the significant outcomes of agitation throughout the fermentation process.

Agitation efficiently distributes nutrients, warms the atmosphere, and incorporates oxygen into the broth throughout fermentation. Agitation also expands the area where the gas and liquid come in contact by breaking the air into tiny bubbles. It also prevents the biomass from congregating to enhance oxygen absorption. The rapid mixing of nutrients creates a heterogeneous mixture and uses more energy.

4.2.4. Impact of agitation and aeration on viscosity

The impact of the aeration rate on the viscosity of fermented broth was investigated during the HA production, and it was observed that if the rate of aeration increased, the viscosity values increased (51.1 ± 0.01 cp, 52.23 ± 0.006 cp, 65.32 ± 0.01 cp, 66.89 ± 0.001) as presented in figure 4.16 D. Oxygen limitation or broth heterogeneity is caused by fast-

growing microbes, high biomass, and HA formation, which increases broth viscosity and serves as a diffusion barrier.

Too much aeration slows down the rate at which products are formed by causing flooding (a reduction in viscosity) around the impellers. In conditions characterized by high viscosity, where bubbles form and mass transfer properties are worsened, oxygen mass transfer can act as a rate-controlling factor. Variables need to be looked at in order to have the best biopolymer yield feasible. Thus, OTR and OUR were investigated to obtain the most increased biopolymer production.

The impact of agitation rate on the viscosity of fermented broth during HA production was investigated and observed that the viscosity of fermented broth increased if the agitation rate increased. Mixing agitation rate directly affects viscosity, oxygen solubility, and oxygen transfer, boosting the cells' absorption and product formation.

It was challenging to produce homogenous mixing in some bioreactors because of the considerable distances between specific portions of the impellers and the culture broth volume. In viscous culture, rapid mixing with high agitation speed is consistently employed to enhance oxygen transport and reduce cell proliferation and activity due to the shear effect.

The agitation rate immediately influences mixing when stirring at an appropriate pace, crucial for reducing the impact of high viscosity and enhancing oxygen transfer and solubility. It improves the cells' capacity to take up dissolved oxygen and generate products. Fast mixing at increased agitation speeds is continually used for improved oxygen transport and inducing the shear action-induced suppression of cell growth and activity in viscous cultures.

The shear rate mainly determines the system viscosity. It may become a rate-controlling phase in aerobic fermentations because of the enhanced bubble coalescence by higher viscosity and the diminished mass-transfer characteristics.

4.2.5. Impact of agitation and aeration on OTR, OUR, and k_La

The experimental graph in Figure 3.2 was created utilizing the dynamic gassing-out method while the *S. zooepidemicus* culture was in its exponential phase at 2 vvm, 250 rpm, in the 3.7 L fermenter. The initial drop curve showed how cell oxygen consumption reduced the amount of DO in the fermenter when the airflow was interrupted (OUR value). When the supply of air had been reestablished while the oxygen was still being utilized by the cells, the following section of the curve demonstrated an increase in the amount of DO in the fermenter, suggesting a change in the oxygen content in the fermenter (dCo/dt value). Both values in exponential phases lowered the DO in the fermenter more quickly than those in the stationary phase, both during cell oxygen consumption and after restarting the oxygen supply. These suggested that in a thick soup, oxygen delivery would be challenging. It is feasible to figure out the oxygen transfer efficiency (OTR value) using the OUR and dC_o/dt values generated by Eq. (13). Aeration and agitation control are often used in aerobic processes because of their significant impact on oxygen transport efficiency.

The OTR and OUR values were tested at various agitation and aeration rates (Figure 4.18). The OUR values observed were 19.32 ± 0.01, 23.52 ± 0.002, 26.42 ± 0.01, and 28.56 ± 0.12 mmol/L/h at the varied aeration rates studied (0.5 to 2 vvm, respectively), but the OTR values ranged from 32.75 ± 0.003, 37.84 ± 0.02, 41.25 ± 0.12, and 43.65 ± 0.03 mmol/L/h.

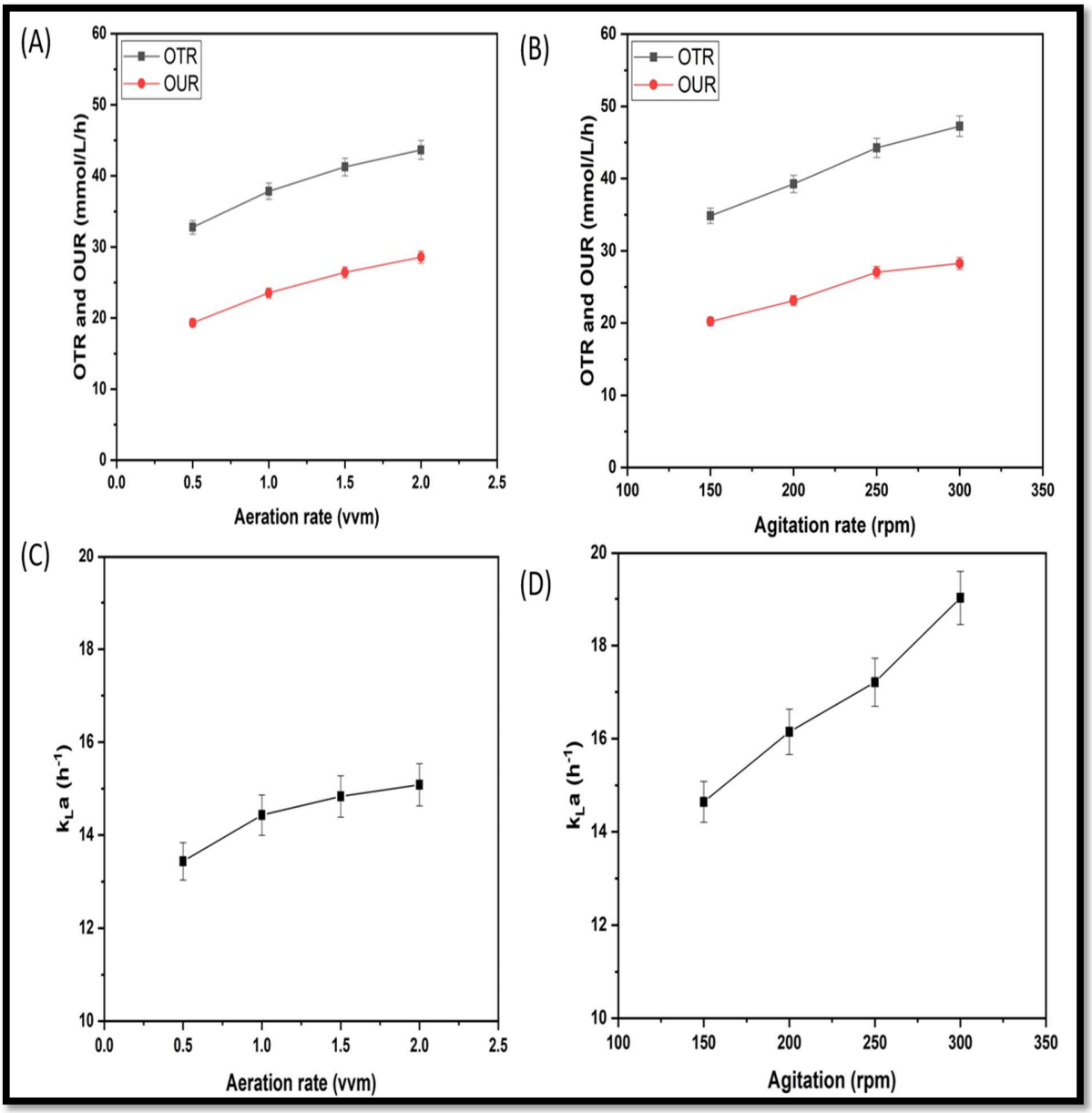

Figure 4.18. Correlation between agitation and aeration rate on (A and B) OTR and OUR, and (C and D) k_La.

The OTR values were more significant than the OUR values, indicating sufficient oxygen for cultivating our desired microbe. With the aeration rate, the OUR and OTR values increased by 31.56 ± 0.12 mmol/L/h for OUR and 43.65 ± 0.03 mmol/L/h for OTR at 2 vvm.

At various agitation speeds evaluated (100-300 rpm), the values of the OUR were 20.21 ± 0.002, 23.11 ± 0.01, 27.04 ± 0.02, 28.25 ± 0.03 mmol/L/h, while the values of OTR were 34.85 ± 0.04, 39.25 ± 0.02, 44.25 ± 0.01, 47.25 ± 0.001 mmol/L/h. The OUR and OTR values enhanced with the rising aeration rate. The highest OTR and OUR values were discovered at 300 rpm. It implied that more oxygen was taken up by cells if more was introduced into the system. It showed that the OTR had an impact on OUR as well.

Mostly, OTR values in this investigation were greater than OUR values in all runs because ample oxygen was available for cultivation. After all, the DOT did not fall below 20%. The cells' high rate of oxygen uptake caused DOT to decline sharply. Although the HA yield decreased with an increase in agitation rate, all processes' OUR and OTR somewhat increased when the aeration and agitation rates were raised. These demonstrated that *S. zooepidemicus* could function and survive in environments with low oxygen levels and strong shear and viscosity.

With the growth in agitation and aeration rate, an increase in the k_La was observed (Figure 4.18 c and d). The k_La values were roughly 13.43 ± 0.002, 14.32 ± 0.002, 14.83 ± 0.01, 15.08 ± 0.01 h^{-1} in the exponential phase at different aeration rates (0.5-2.0 vvm). The values of k_La at varied agitation rates ranged from 14.64 ± 0.001, 16.14 ± 0.001, 17.21 ± 0.02, 19.02 ± 0.002 h^{-1}.

In this study, aeration and agitation rate increases resulted in higher k_La values, but agitation rate increases resulted in lower cell growth and biopolymer production. As a result, the aeration effect and k_La values are positively correlated with biopolymer productivity, while the agitation effect and k_La values are negatively correlated with biopolymer productivity.

Numerous investigations on fermentation's role in forming biopolymers have indicated that these relationships are frequently present. A high agitation rate (high shear stress) reduces cell activity and growth while altering the structure and viscosity of biopolymers. In brief, the biopolymer yield for most aerobic procedures increased as both the aeration rate and agitation speed climbed, with the agitation speed having a higher negative impact than the aeration rate. It was expected because agitation significantly affected oxygen transfer rates more than aeration in a mechanically agitated tank (Elibol & Ozer, 2000).

It is simple to see how DO concentrations, OTR, and k_La values are related. A significant increase in productivity was associated with increased k_La at various aeration rates and agitation speeds since OTR had a more substantial impact on agitation than on aeration. Mixing remained crucial for oxygen transfer and cell activity as the bioprocess was scaled up. As a result, the biomass production rate and the resultant polymer's physical properties are significantly impacted (Audet et al., 1998).

As a consequence of excellent air dispersion and, subsequently, faster adsorption of cells onto the bubble surfaces, the intensification of mixing may result in a drop in k_La (Galaction et al., 2004). The phenomenon of cells clinging to bubble surfaces obstructing their surfaces causes an increase in the k_La value. This phenomenon can be explained by contrasting the k_La values for viscous suspensions with and without biomass.

4.2.6. Bench-scale correlation of k_La values with HA production

Increasing agitation and aeration rates increased k_La values at the bench scale, whereas enhancing agitation rates decreased cell growth and biopolymer yield. Hence, aeration effects

are positively associated with k_La values on HA productivity, while agitation effects are negatively associated with k_La values on biopolymer productivity.

Numerous studies of fermentation for the production of biopolymers have found similar correlations. Bandaiphet et al. (2006) (Bandaiphet & Prasertsan, 2006) studied the effects of an increased k_La value on exopolysaccharide concentration at a high agitation rate. However, low productivity was reported despite increased oxygen transfer into the viscous broth. The structure and characteristics of the biopolymer, such as viscosity, are impacted by shear stress (high agitation rate), which also inhibits cell growth and activity. Following an unavoidable rise in shear stress brought on by a higher rate of agitation, cell viability declined. The growth and productivity of our cells are impacted by a faster mixing rate since it increases the mechanical stress across the membrane and eventually leads it to cell-burst. The cell viability was minimum with 67% at 300 rpm, while at 250 rpm it was maximum with 83%.

Low DCW and biopolymer yield were caused by a low viscosity resulting from a high agitation rate and heterogeneous mixing. Most aerobic processes increase their biopolymer productivity by enhancing aeration rate and agitation speed, with agitation speed having a more significant negative effect than the aeration rate. The oxygen transfer rate was expected to be affected more severely by mechanical agitation than by aeration in a mechanically agitated vessel (Elibol & Ozer, 2000). A direct correlation exists between DO concentrations and OTR and k_La values. OTR depends more soundly on agitation than on aeration as determined by k_La under different aeration rates and agitation speeds; therefore, with increasing k_La, productivity increased satisfactorily.

Oxygen transfer and cell activity were also influenced by mixing in a bioprocess and its scaling up. The biomass generation rate and the polysaccharide product's physical characteristics were significantly influenced by mixing (Audet et al., 1998). Mixing intensification helps reduce k_La, especially when the air dispersion is adequate, and cells are more accessible to adsorb to bubble surfaces because of a reduced diffusion rate, resulting in lower biomass concentration (Galaction et al., 2004).

Bubble surfaces are obstructed by cell adhesion, which is the reason for the rise in k_La value. It is possible to explain this phenomenon by comparing the k_La values for viscous suspensions with and without biomass. It is essential to consider the type of microorganism when analyzing the blocking effect's strength on k_La values. Since the mixing is proper near the impellers, the k_La is high, but where the mixing is heterogeneous, the k_La is low. During HA production, heterogeneous mixing was also observed at too high agitation rates, affecting k_La.

4.2.7. Impact of agitation and aeration rate on k_La at pilot plant scale

The broth will become increasingly heterogeneous, and some parts of the reactor might run short of oxygen while scaling up (Thiry & Cingolani, 2002). The oxygen supply typically constrains scale-up to the developing cells. The DOT values declined exponentially at the pilot plant scale in this investigation, which is consistent with the bench scale results.

The DOT values were consistently higher than 20%, suggesting that the oxygen support system was always sufficient during all the runs. Pilot plants were also used for aeration studies (0.5, 1.0, 1.5, and 2.0 vvm) and agitation experiments (150, 200, 250, and 300 rpm) on OTR, OUR, and k_La values. These parameters influence the agitation rate more

significantly than the aeration rate. The k_La values at various agitation rates are shown in Figure 4.19. The agitation and aeration rates rose along with the k_La values. The highest k_La values (19.57 h^{-1}) were discovered at 2.00 vvm and 300 rpm for different aeration rates (1.25-2.00 vvm). The k_La values at 150 rpm were 11.75-14.98 h^{-1}, 200 rpm (13.65-15.68 h^{-1}), and 250 rpm (15.39-17.45 h^{-1}). Due to the high OUR under high viscosity, the maximum k_La value was still present at the most elevated agitation and aeration rates. It was discovered by comparing the k_La values from the bench scale that there is little difference between the two k_La values at 2 vvm and 250 rpm, or 17.21 and 17.45 h^{-1}. Therefore, it was decided to keep k_La around this for scale-up production to produce HA under optimal circumstances.

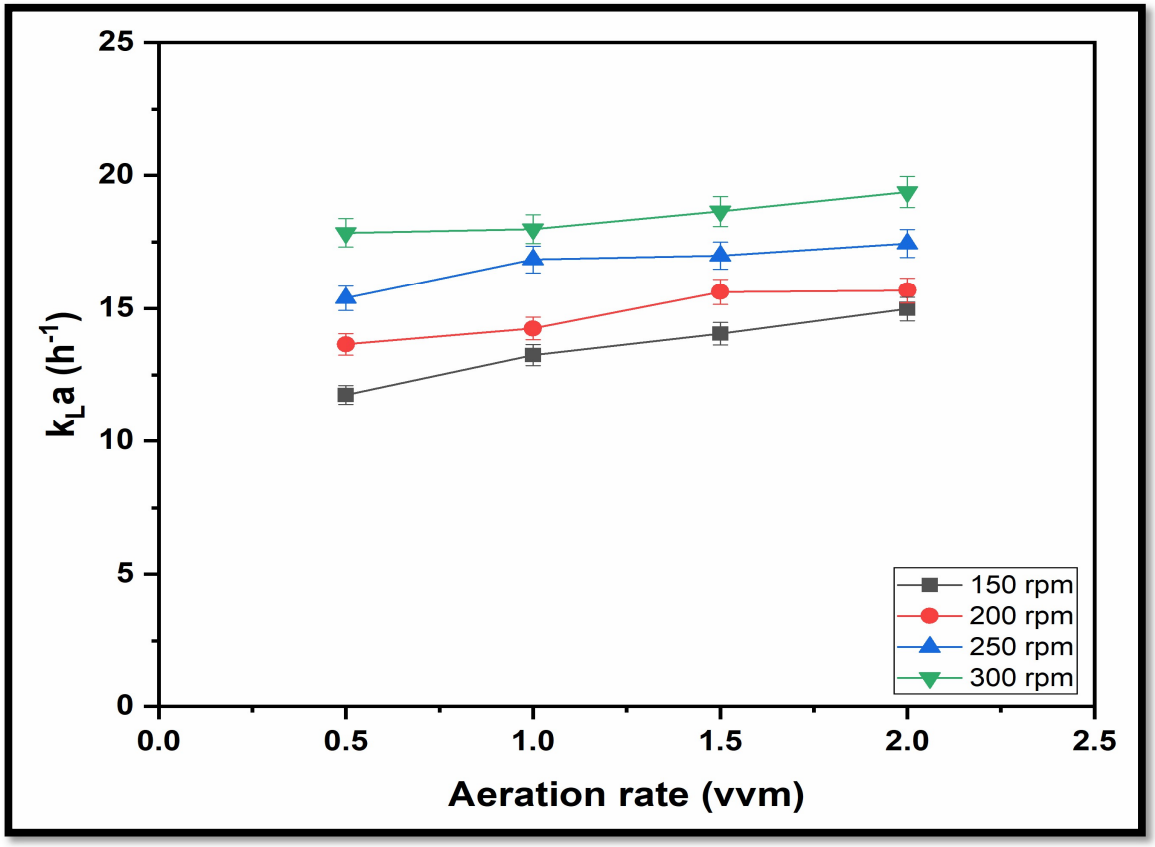

Figure 4.19. k_La values at various agitation and aeration rates.

4.3.Optimization using artificial neural networking

4.3.1. Development of the model

Prior studies have shown that optimizing the concentration of the cane molasses in the feedstock, pH, and rpm during the fermentation method increases HA yields (Amado et al., 2017; Shukla et al., 2022a). Here, our goal is to fit the concentration levels of the carbon pH and rpm of the media during the production process using innovative ANNs and SVM, which can then be used to forecast the HA titer.

The dependent variable was chosen to be the HA titer (g/L), and the amount of the cane molasses (g/L), pH, and rpm levels were specified as independent variables. Divide the data into training and testing sets before model formation because the numerical prognosis of the machine learning approach is entirely dependent on already-existing data. While testing sets validate the trained model after training, training sets assist programs in "learning" data regulation.

Throughout this case, 40% of the dataset was chosen for the testing set and 60% for the training set. The trial version of the NeuralTools® software from Palisade Corporation, NY, USA, was used to create the ANN prediction models (Balali et al., 2020; Desai et al., 2008; Pollar et al., 2007; Wang et al., 2016a). GRNN and MLFN were chosen as training algorithms. The SVM was created using the Matlab program. To evaluate the effectiveness of the ANNs and SVM, training time and root mean square (RMS) error acted as the performance metrics (Table 4.4). A correlation was sought between developing the 2 to 25 MLFN node count and the change in MLFN regulation.

Table 4.4 reveals that the average RMS errors for the GRNN (394.98), SVM (456.25), and MLFNs with two and three nodes (637.96 and 654.21) are comparatively minuscule. In contrast to the MLFNs, which have much higher RMS errors and prolonged training durations, the RMS errors and training times of the SVM and GRNN are the shortest. The forecast accuracy functioned as a yardstick for assessing prediction accuracy.

If the relative error is lower than 30% of the actual value, a solitary prediction result could be regarded as an "excellent prediction" in applications where the empirical threshold of ANNs is 30%. The percentage of "good predictions" in the tested sample relative to the entire testing set is the forecast accuracy in this case. According to Table 4.4, the GRNN and SVM exhibit forecast accuracy of 30% or less off from 100% and 99.63, respectively. To choose the optimal platform for setting up the parameters for the fermentation process that would produce HA, the existing GRNN, SVM, and MLFNs were explored throughout this topic.

Table 4.4. Tabular presentation of the models applied and their training time, RSM error, and forecast accuracy

Model Type	**RSM Error (Mean)**	**Training Time**	**Forecast Accuracy (%)**
MLFN (2 nodes)	637.96	0:00:14	86.96
MLFN (3 nodes)	654.21	0:00:21	88.65
MLFN (4 nodes)	879.61	0:00:42	81.23

MLFN (5 nodes)	865.23	0:00:59	79.37
MLFN (6 nodes)	745.22	0:01:03	85.25
MLFN (7 nodes)	1326.56	0:01:32	62.36
MLFN (8 nodes)	985.65	0:01:48	74.69
MLFN (9 nodes)	793.89	0:01:57	78.98
MLFN (10 nodes)	844.26	0:02:18	63.39
…….	……	……	……
MLFN (25 nodes)	2569.73	0:02:06	0.0
GRNN	394.98	0:00:01	100
SVM	456.25	0:00:01	99.63

4.3.2. Comparison of the MLFNs and the GRNN

Comparing the GRNN to the other 24 MLFNs used in our research, its training duration is the shortest, and its RMS error is the lowest. In our study, the GRNN has a significant advantage over other ANNs due to its excellent repeatability and robustness of the underlying principles (Kayaer & Yildirim, 2003; Patel et al., 2022). The computational tests for the GRNN were repeated to examine the robustness of the network, and the outcomes are outlined in Figure 4.20**.**

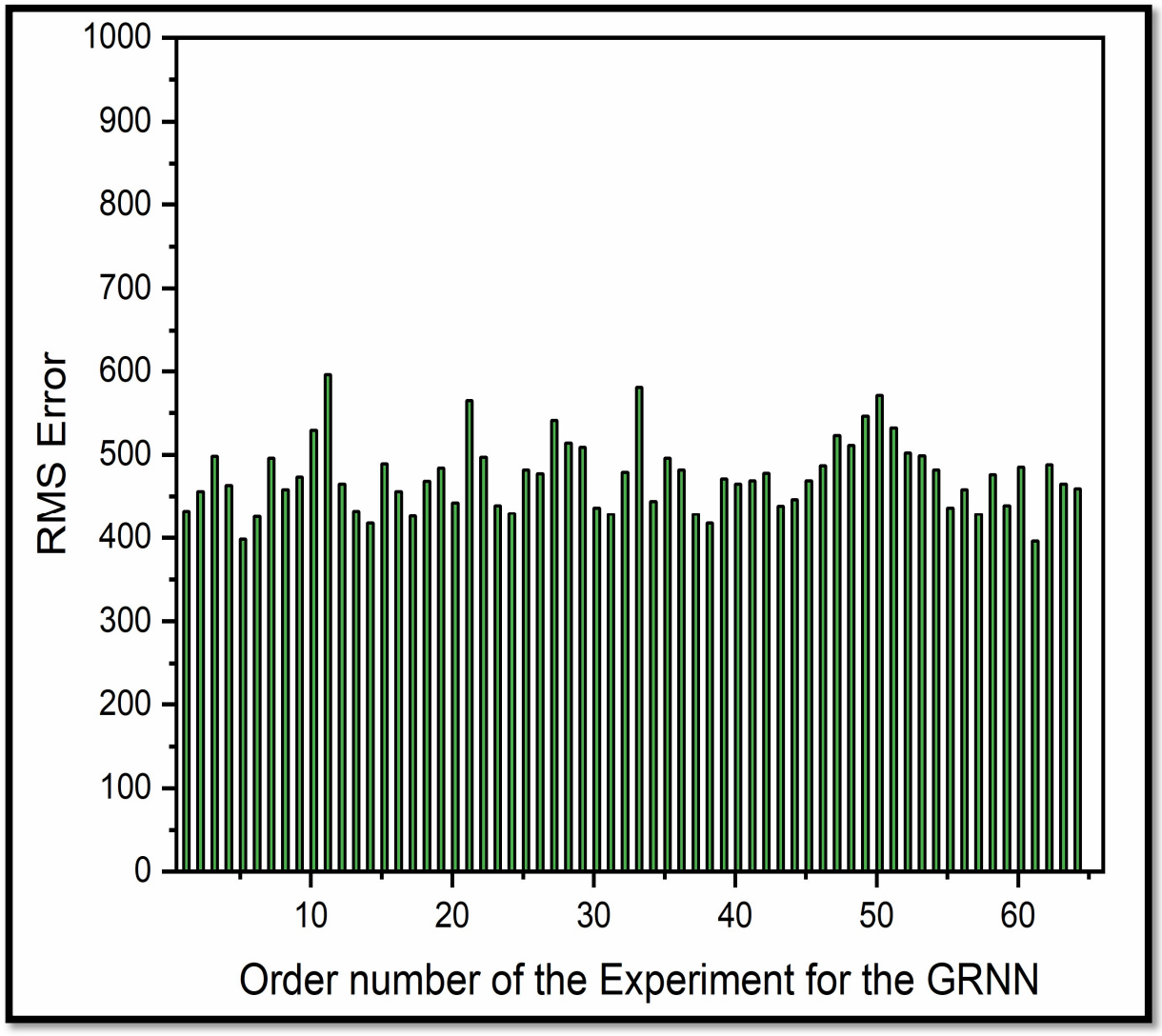

Figure 4.20. GRNN experimentation results from repeated computations.

Figure 4.20 shows the GRNN's RMS errors throughout multiple experiments. The fact that there is a consistent fluctuation throughout the experiments is essential since it shows how reliable the GRNN utilized in the optimization procedure is. Notably, the mean RMS error is small, guaranteeing the GRNN's accessibility. In all repeated studies, the GRNN's prediction accuracy is 100% within the tolerance of 30%.

Figure 4.21 illustrates how distinct MLFNs regulate variation by displaying the RMS errors and training intervals for MLFNs with multiple nodes. With the rise in the number of nodes, MLFNs' RMS errors and training times fluctuate, which is prominent and perfectly consistent with the fluctuation-like structure of the MLFN paradigm. It should be underscored that the significance of the multiple randomized beginning values selected by the computer during training means that the results in the various MLFNs reported in Table 4.4 do not represent the fixed outcomes.

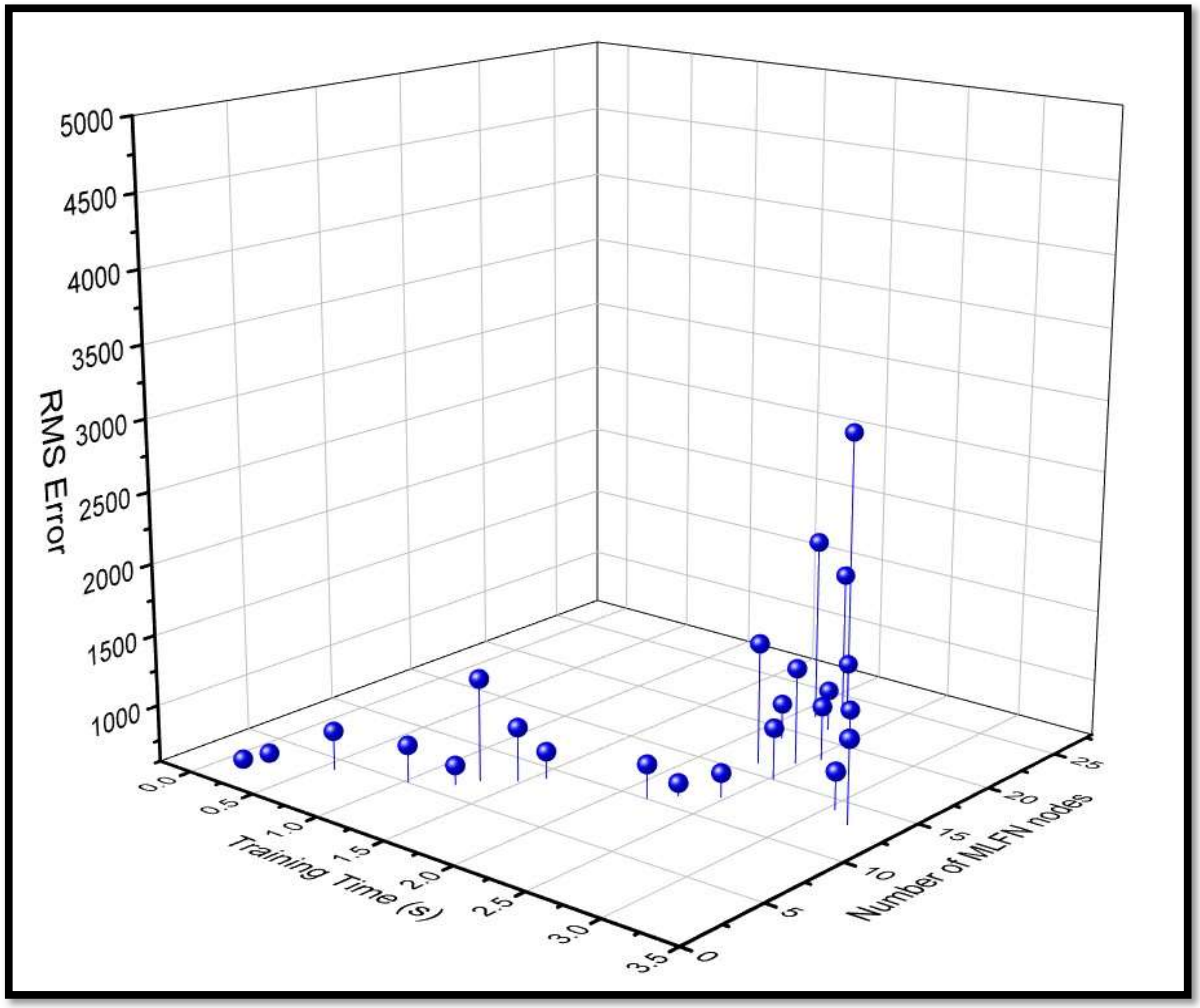

Figure 4.21. Training times and RMS error of MLFN with the change of nodes

MLFNs can function successfully, albeit with a few nodes (far too few RMS errors and rapid training times). In the vicinity of a handful of nodes, the optimal model for fed-batch fermentation environment improvement must be obtained; one should employ pertinent software for potential implementation. MLFNs are more expensive and have fewer stable fluctuations than GRNNs. As a result, the GRNN is thought to be a superior model for figuring out how to set up fed-batch fermentation best.

4.3.3. Details of training and testing the SVM and GRNN

To further illustrate the value of the GRNN and SVM, the most widely used applications of such training and testing results were employed. The training and testing results for the GRNN are shown in Figures 4.22 and 4.23, whereas those for the SVM are shown in Figure 4.24. For both GRNN and SVM, the training and testing datasets are identical. Figure 4.22, which shows the results of the GRNN's training, is an example of the network's recall capacity for design optimization. It exhibits the strong recall capability of the GRNN. The model's significant non-linear fitting effects may be seen in Figure 4.22a, where the projected numbers and the actual values are reasonably similar. Analogies between the residual and actual or expected values further demonstrate that the residual values seem modest (Figures 4.22b and 4.22c), indicating the durability of the GRNN's development.

The GRNN's utility was illustrated after training using the data set that was not employed in the training process. Figure 4.23 displays the outcomes. During the testing phase, the precise expected results are shown in Figure 4.23. Values predicted are reasonably close to those observed (Fig. 4.23a). The residual values of Figures 4.23b and 4.23c demonstrate the low residual values. Results show the GRNN model's availability and robustness during testing.

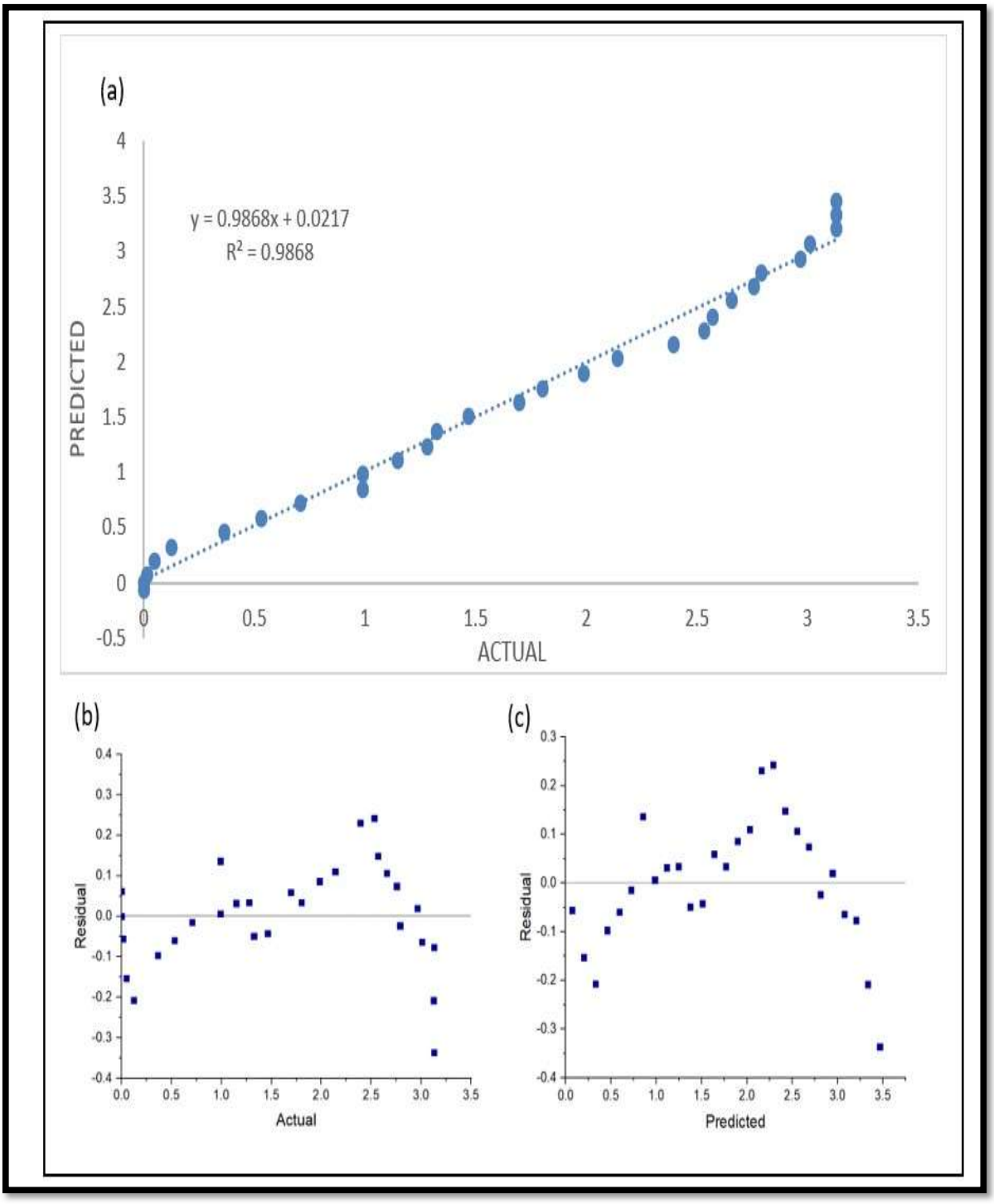

Figure 4.22 Performance of training the GRNN. Comparisons of (a) expected and actual values, (b) residual and actual values, and (c) predicted and residual values.

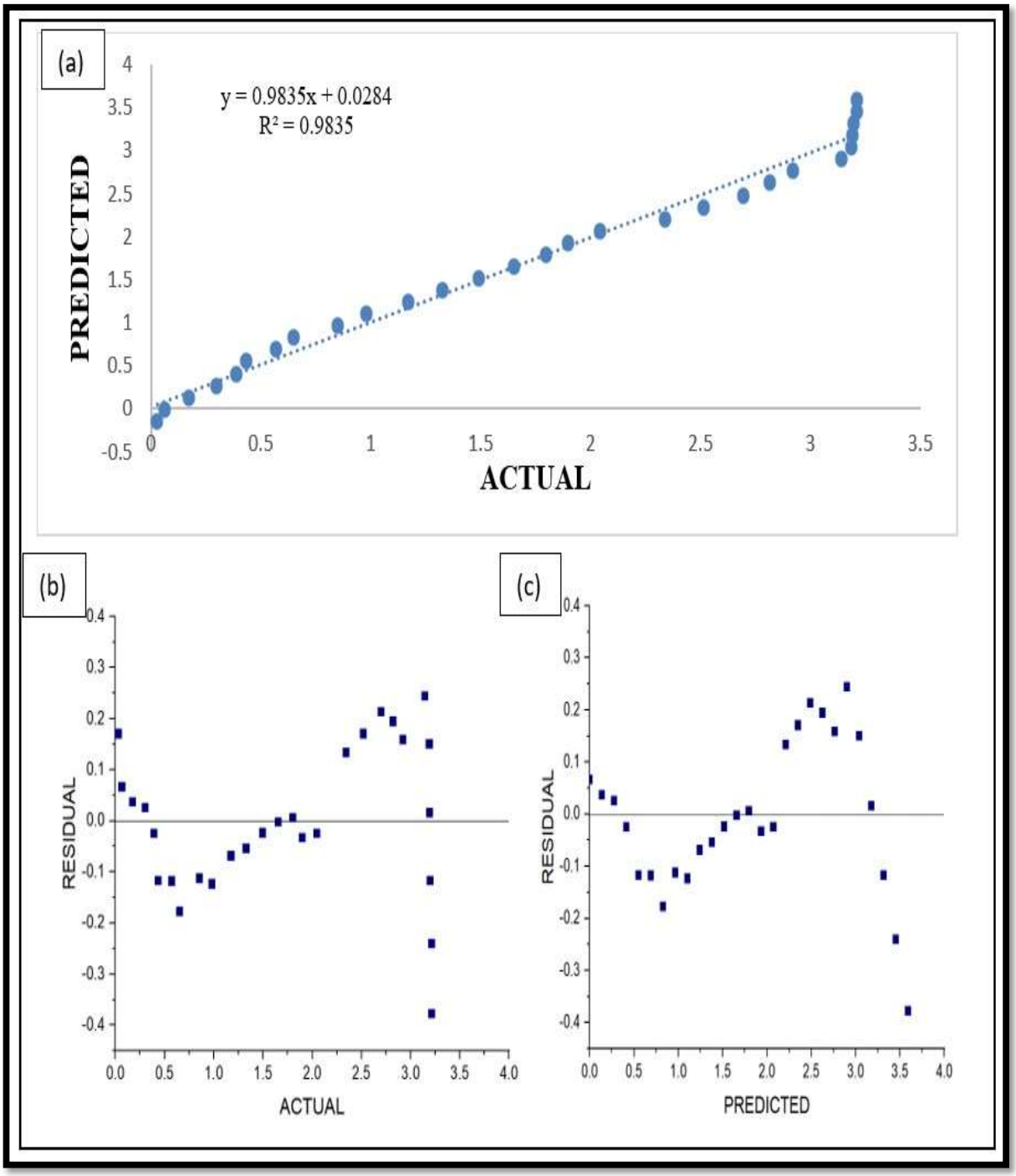

Figure 4.23 Performance of the GRNN's testing. A comparison of (a) predicted and actual values, (b) residual and actual values, and (c) residual and predicted values.

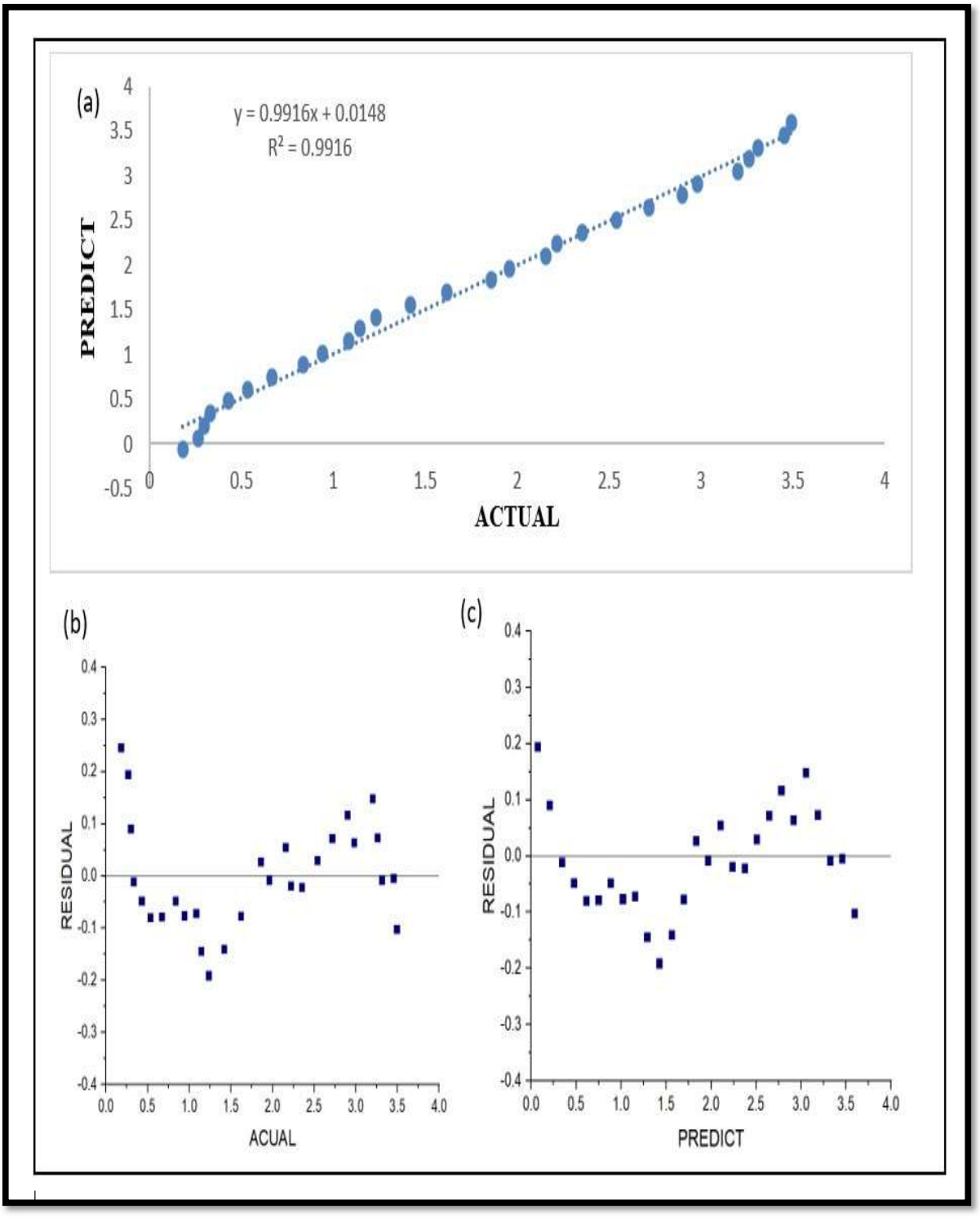

Figure 4.24 Performance of the SVM's testing. A comparison of (a) predicted and actual values, (b) residual and actual values, and (c) residual and predicted values.

Figure 4.24 demonstrates how well the SVM executed correctly and persistently in the SVM testing results' prediction component. Given that the SVM's RMS error and training time are comparable to those of the GRNN, the testing results are also relatively identical to those of the GRNN. The SVM can produce a reasonably similar and accurate result by comparing its testing results to those of the GRNN.

In conclusion, HA can be created by utilizing the GRNN and SVM to optimize the fed-batch fermentation conditions. The RMS errors and training times of the GRNN and SVM are relatively low.

The user-friendly software makes the GRNN and SVM more useful (Abdou et al., 2012; Liu et al., 2021; Pollar et al., 2007; Wang et al., 2016a). Alone without the necessity for intricate operation labor, professionals can apply the concepts and techniques presented in this article to imperative programming.

4.3.4. Comparisons with the RSM method of optimization

The current work for fermentation media optimization evaluates the prediction and generalization capacities, sensitivity analysis, and optimization effectiveness of ANN and RSM techniques. ANN demonstrated superior accuracy and generalization abilities even with a few experiments compared to RSM. Compared to RSM, ANN's prediction accuracy was nearly three times higher.

Previous papers (Liu et al., 2009b; Mohan et al., 2016; Samadi et al., 2022; Shukla et al., 2022a) presented related alternative optimization approaches for biotechnology, including the RSM, regression analysis, and the orthogonal experiment method. Despite having particular strengths that are their own, these models have substantial shortcomings comparable to

ANNs and SVM and several alternative machine learning methods (such as minimal CPU requirements).

Precision, resilience, and time efficiency are typically the significant benefits of ANNs and SVM in the optimization procedure of the biotechnological industry. The "well-trained" training data set is the foundation for ANN and SVM projections, and their applications can operate automatically with little human assistance.

An effective non-linear prediction system that guarantees forecast accuracy can even be made using the non-linear function of ANNs (Vouk et al., 2011). The SVM's guiding principle can substantially ensure reliable outcomes (Deng et al., 2012)**.** ANNs and SVM, which are quicker and easier to utilize, may now be constructed thanks to advancements in computers and programming tools.

4.4.Hyaluronic acid production on bench scale

Twenty-eight hours of batch fermentation were used to produce HA. During the fermentation procedure, the aeration and agitation rates were kept constant at 2 vvm and 250 rpm, respectively.

The pH and temperature were set at 7 and 37 ºC. Periodically, samples were collected to assess dry cell weight, substrate uptake, and HA production. It was observed that the dry cell weight exponentially increased until 28 h of incubation, and the final cell mass reached a maximum of about 4.08 ± 0.01 g/L.

The substrate concentration gradually decreases as sugar is consumed more in the growth phase. HA is present in the fermentation broth as it is part of the microorganism's cell

membrane, but its production enhanced at about 4 h when the exponential phase started and observed a maximum of 3.51 ± 0.01 g/L (Figure 4.25). HA, a growth-associated product, did not increase in the stationary phase (results not shown).

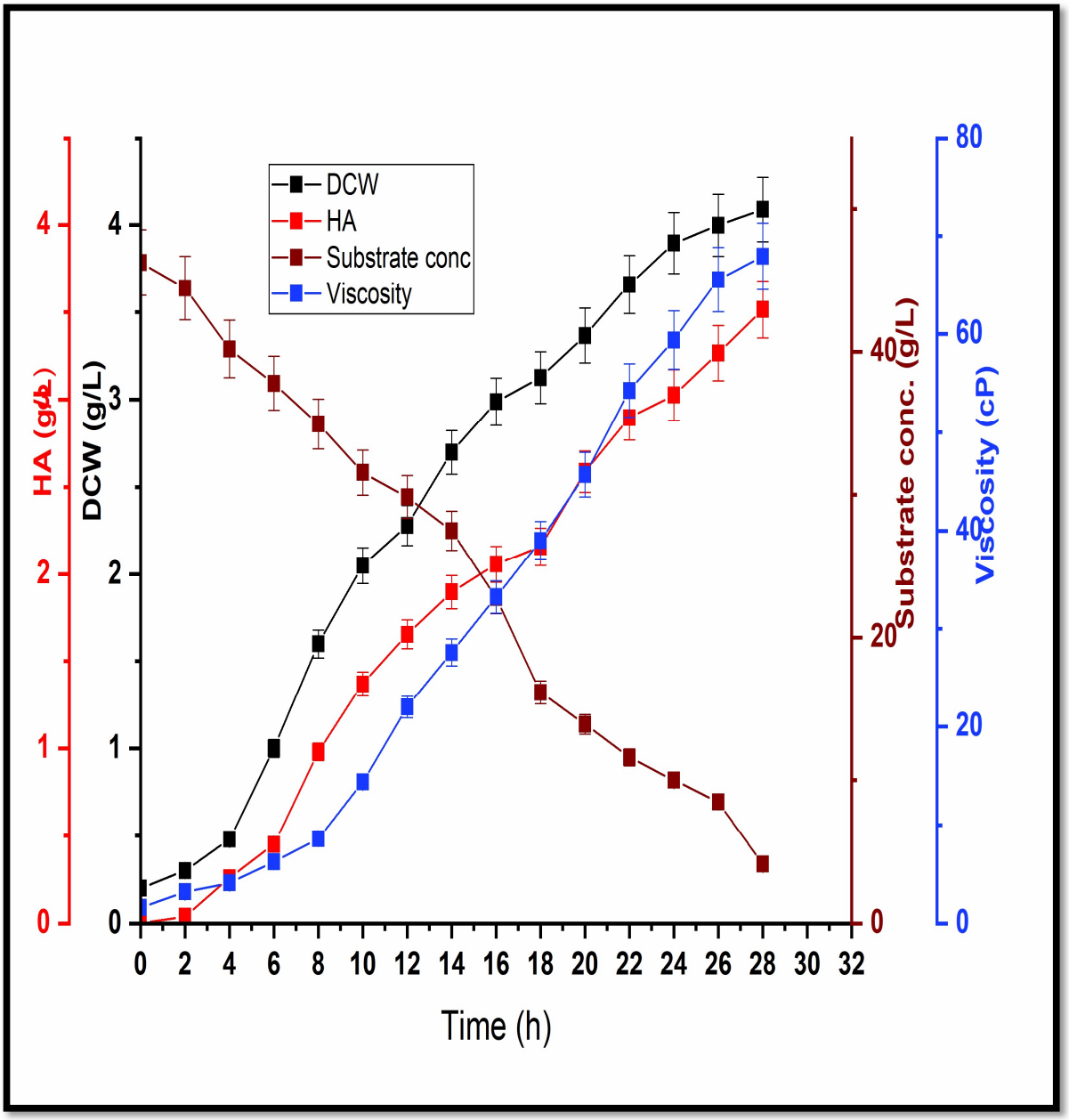

Figure 4.25. DCW, HA production, substrate consumption, and viscosity concerning time during *S. zooepidemicus* cultivation.

Researching the impact of agitation, aeration, and other factors like dissolved oxygen, viscosity, and substrate concentration during the process will help us better understand biopolymer production and its kinetics (Garcia-Ochoa & Gomez, 2009).

Two significant outcomes of agitation in the course of fermentation are mixing and shearing, which efficiently combines oxygen, heat, and nutrients, enhance the surface area of the gas-liquid interface by distributing air into tiny bubbles, and prohibit cells from aggregating to promote oxygen absorption (Mantzouridou et al., 2002).

However, if the agitation rate is inadequate, the fermentation broth's viscosity will increase, reducing the effectiveness of mass transfer (Bandaiphet & Prasertsan, 2006). The study discloses that 250 rpm was the optimal agitation speed for producing HA from the strain *S. zooepidemicus*.

In addition to providing the essential oxygen for cell growth, aeration eliminates the exhaust gases produced during fermentation (Mantzouridou et al., 2002). The amount of the fermentation medium is nonetheless reduced when the aeration rate is increased. In aerobic fermentation, oxygen supply is required for microbe growth, yet some bacteria may experience oxygen toxicity at high oxygen concentrations (Bandaiphet & Prasertsan, 2006).

Aeration and agitation were optimized for enhanced HA production on a bench scale during the fermentation process, which resulted in a final HA production of 3.51 ± 0.01 g/L in a 3.7 L fermenter. Don et al. reported approximately 1.9 g/L of HA production by optimizing the effect of glucose on growth kinetics (Don & Shoparwe, 2010).

Samadi et al. increased the HA production twofold by optimizing the growth kinetics with enzymes and reported production of 384.6 ± 7.5 g/L (Samadi et al., 2022). In a 5-liter

bioreactor, Amado et al. reported producing 3.2 g/L of HA using cheese whey as a substitute substrate (Amado et al., 2016). Long et al. reported an increase in HA production by 30% by increasing k_La by adding 5% (v/v) n-dodecane in the medium (Long et al., 2009). In our study, the average k_La rate maintained was around 20 $h^{-1,}$ which increased HA when agitation and aeration rate were maintained at 250 rpm and 2.0 vvm, respectively.

The molecular weight of HA ranged between 500 and 950 kDa. This varied range of molecular weight may result from the formation of HA, which is growth-associated, with low molecular weight first emerging at the beginning and high MW HA accumulating by the end of fermentation (Rangaswamy & Jain, 2008a).

Heterogeneity in a scale of molecular weight range has been observed in various purification studies (Reddy & Karunakaran, 2013). Glucose produces lower MW HA than lactose or sucrose-containing medium as a carbon source (Armstrong & Johns, 1997).

A wide range may also result from HA's lower prolonged mechanical integrity (DeAngelis, 1999). The HA obtained has an average zeta size of 9075 ± 0.03, a polydispersity index of 0.58 ± 0.06, and a PDI width of 6920 ± 0.05 d.nm.

4.5. Hyaluronic acid recovery and purification

4.5.1. Precipitation

An investigation into an array of purification techniques was performed to determine how early purification stages might affect the final efficacy of the product (Kumar et al., 2004). In HA production, proteins serve as the primary source of contaminants. For the removal of proteins, precipitation using organic solvents or quaternary salts has been employed extensively (Reddy & Karunakaran, 2013).

Precipitation typically appears in the earliest stages of the HA purification procedures due to its efficiency in eliminating the majority of proteins and other impurities (Amagai et al., 2009a).

A careful study was performed on how ethanol and NaCl interact to precipitate retentates (Figure 4.26). Ethanol is more cost-effective and less hazardous (Murado et al., 2012). This reaction evaluated HA concentration and recovery proteins by re-dissolving relevant sediments in ethanol-water.

Salt concentration did not impact HA recovery, which increased asymptotically with ethanol content. However, extreme levels of both variables caused HA recovery to decrease continuously from its maximal value.

In contrast, protein repair decreased as salt concentration increased at any pre-determined level of ethanol because proteins are significantly affected by salt content. The data showed that the most effective recovery of HA (89.36%) was achieved with 2 M NaCl concentration and ethanol fractions 2 vol/vol of the retentate fraction.

Lower salt concentrations did not alter HA recovery but did result in extracts with higher protein concentrations, whereas lower ethanol concentrations resulted in loss of HA.

The elimination of host cell proteins, nucleic acids, and endotoxins was enhanced by a two-step precipitation procedure that used 2 M $CaCl_2$ and 10% hexadecyltrimethylammonium bromide solution for flocculation, followed by dilution with ethanol (3:2 v/v) for HA precipitation from the culture medium.

This experiment eliminated over 10% of the proteins, nucleic acids, and endotoxins, while just 1% to 2% of the HA was lost. Almost a complete removal of cell debris was observed.

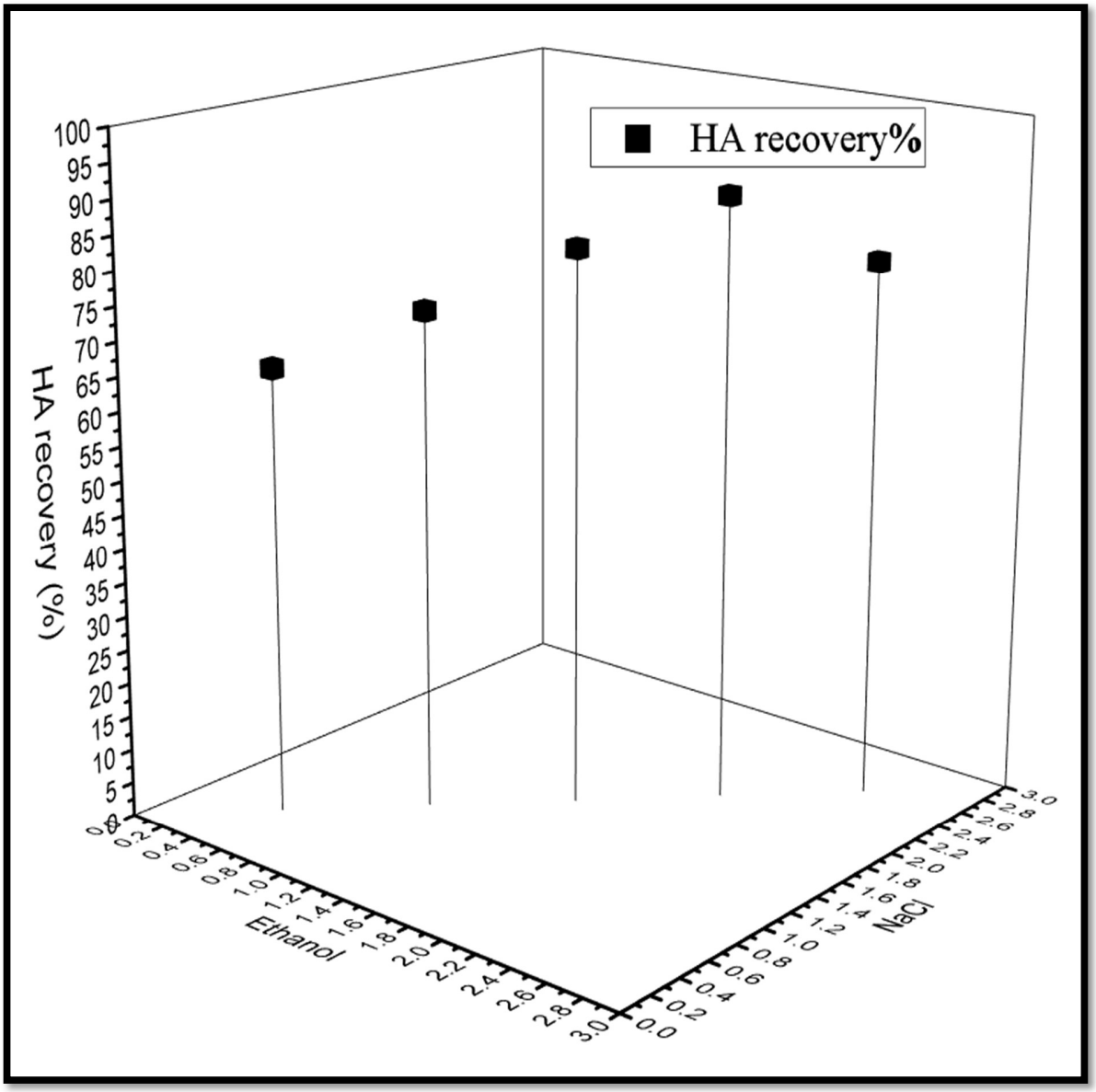

Figure 4.26. Recoveries of HA in redissolution of precipitates containing different proportions of ethanol (volumes per volume of the retentate) and NaCl (molarity in the retentate).

4.5.2. Adsorption

The powdered and granulated activated charcoal displayed potent HA adsorption abilities in purification broth; their saturation adsorption capacities reached 178.61 and 123.72 mg/g, respectively (Figure 4.27). Granular activated charcoal adsorbed less HA than the powdered activated charcoal's total adsorption.

Table 4.5 displays the desorption of HA from activated charcoal by various eluents. Neither ethanol nor acetic ether could entirely desorb HA, but ethanol's desorption capability marginally increased with adding HCl. Once the concentration reached 2.0%, NaOH solution served as an effective desorption agent, releasing 93.12% of the HA from activated charcoal.

Powdered activated charcoal DARCO® was added to the precipitated solution, effectively adsorbing lingering proteins and other contaminants. It resulted in a transparent solution by removing the turbidity. After the adsorbent treatment, proteins and nucleic acids were present in considerably small amounts in the solution.

The charcoal treatment, unlike precipitation, resulted in around 7-9% HA loss with no effect on HA’s molecular weight. A pure HA product was obtained after filtering off the adsorbents utilized. The color in the sample broth, mainly because of the cane molasses, was almost removed, and a clear solution was obtained.

However, XAD-7 resins were applied for adsorption to remove any activated carbon and other remaining impurities. The XAD-7 resins preferentially adsorbed more contaminants than HA under the examined conditions.

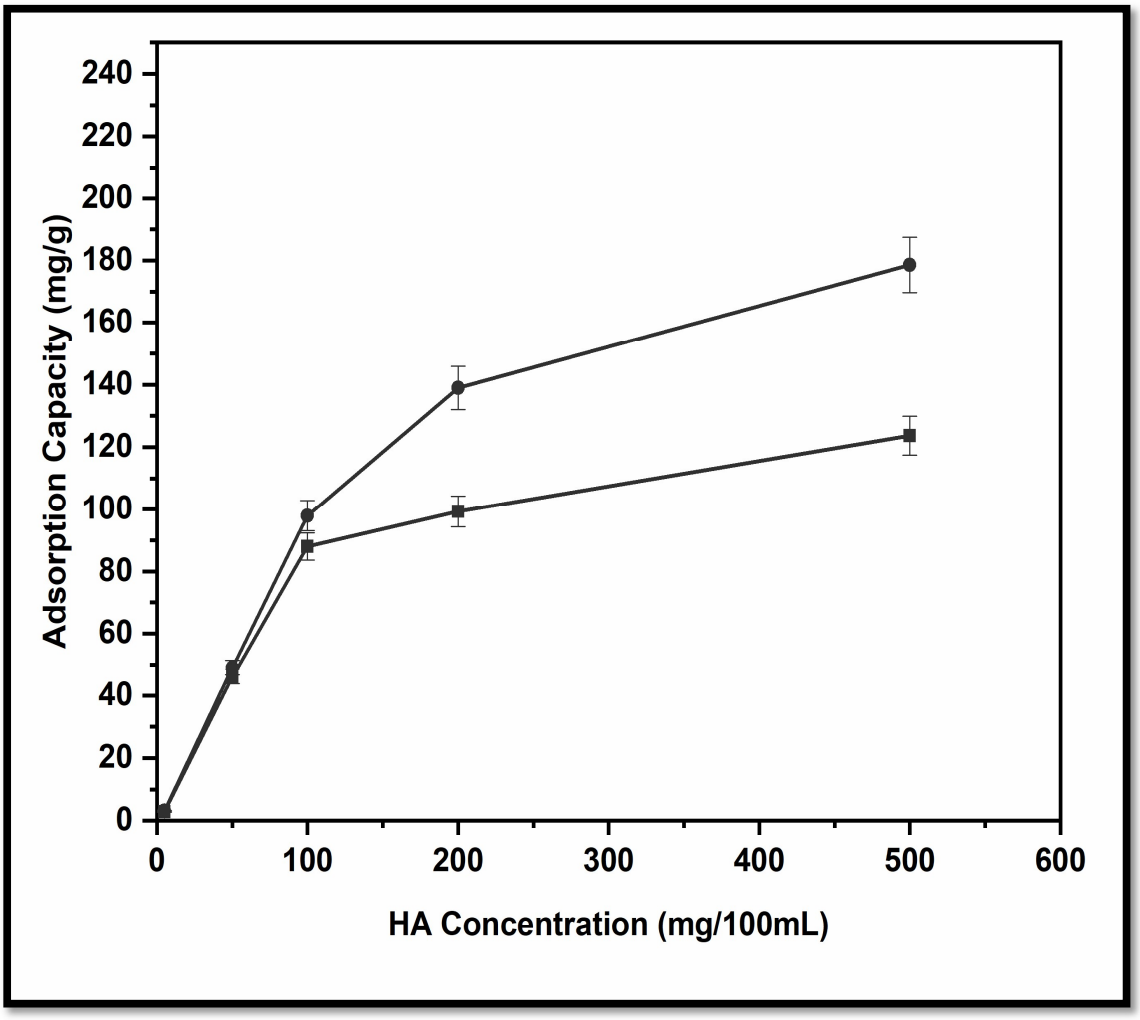

Figure 4.27 Activated charcoal's ability to adsorb hyaluronic acid at various concentrations, powdered activated charcoal (circles), and granular activated charcoal (squares).

Table 4.5 Pure HA desorption from activated charcoal: Effect of several eluting solutions at room temperature and pH 7

Eluting Solutions		**Desorption (%)**
NaOH	0.5%	72.32±0.03

	1%	84.63±0.12
	1.5%	91.68±0.09
	2%	93.12±0.21
Acetic ether		10.23±0.03
Ethanol/HCl		23.63±0.34
Ethanol		12.39±0.25
Deionized water		9.65±0.22

Additionally, it was discovered experimentally that the contaminants in the treated broth were swapped or adsorbed earlier in the process (within 4-6 h) than the desired HA. Therefore, the resins were utilized to adsorb contaminants from the treated broth rather than the HA.

The controlled temperature-swing adsorption method provided excellent HA separation efficiency. The intensification parameters examined were the surface area, adsorbent structure (granular and powder), and energy efficiency. It caused the volume of the adsorbent to decrease significantly, and it improved mass transfer effectiveness.

Different levels of endotoxins were adsorbed into them depending on the type of adsorbents. Activated carbon showed maximum removal of endotoxins (89.63%) out of both adsorbents utilized, which was higher than the earlier reported removal of endotoxins (Rangaswamy &

Jain, 2008a; Reddy & Karunakaran, 2013) and close to 90% removal as reported by Choi *et al.* with the use of Norit C Gran and Norit GAC 1240^{+} (Choi et al., 2014). The resins' removal of endotoxins was lower than the DARCO® (63.87%).

In the case of peptides and proteins, activated carbons eliminated 93.58% of the proteins, while XAD-7 removed 69.23% of the proteins. Around 96.23% and 72.3% of nucleic acids were removed using activated carbon and XAD-7 resins, respectively. After using activated charcoal in this case, slightly polar XAD-7 resins were very effective since they eliminated the charcoal particles and other contaminants and created a clear solution for further filtration.

4.5.3. Diafiltration

Three categories were used to categorize the total solute composition: HA (macrosolutes), charged microsolutes (mostly minerals and salts), and peptides and proteins (proteins microsolutes). During the first four diavolumes, the C/C_o of charged microsolutes and peptides/proteins dropped significantly, whereas HA remained constant. It demonstrated substantial HA retention (R) and poor protein and mineral retention (R). Using the least-squares method, the microsolutes R values for HA, charged, and amino acids were calculated using the following mass balance equation (Eq. (3), (Figure 4.28) (Foley, 1999)):

$$\frac{C}{C_o} = e^{-(1-R)\frac{V_W}{V_o}} \ldots\ldots \quad \text{Eq. 3}$$

The concentration of solute in the feed tank is given as C, the initial feed tank volume is presented as V_o, the initial solute concentration is given as C_o, the water delivered to the feed

tank is given as V_w, and the retention is given as R. It represents how many diavolumes cross the membrane when V_w/V_o is ratioed.

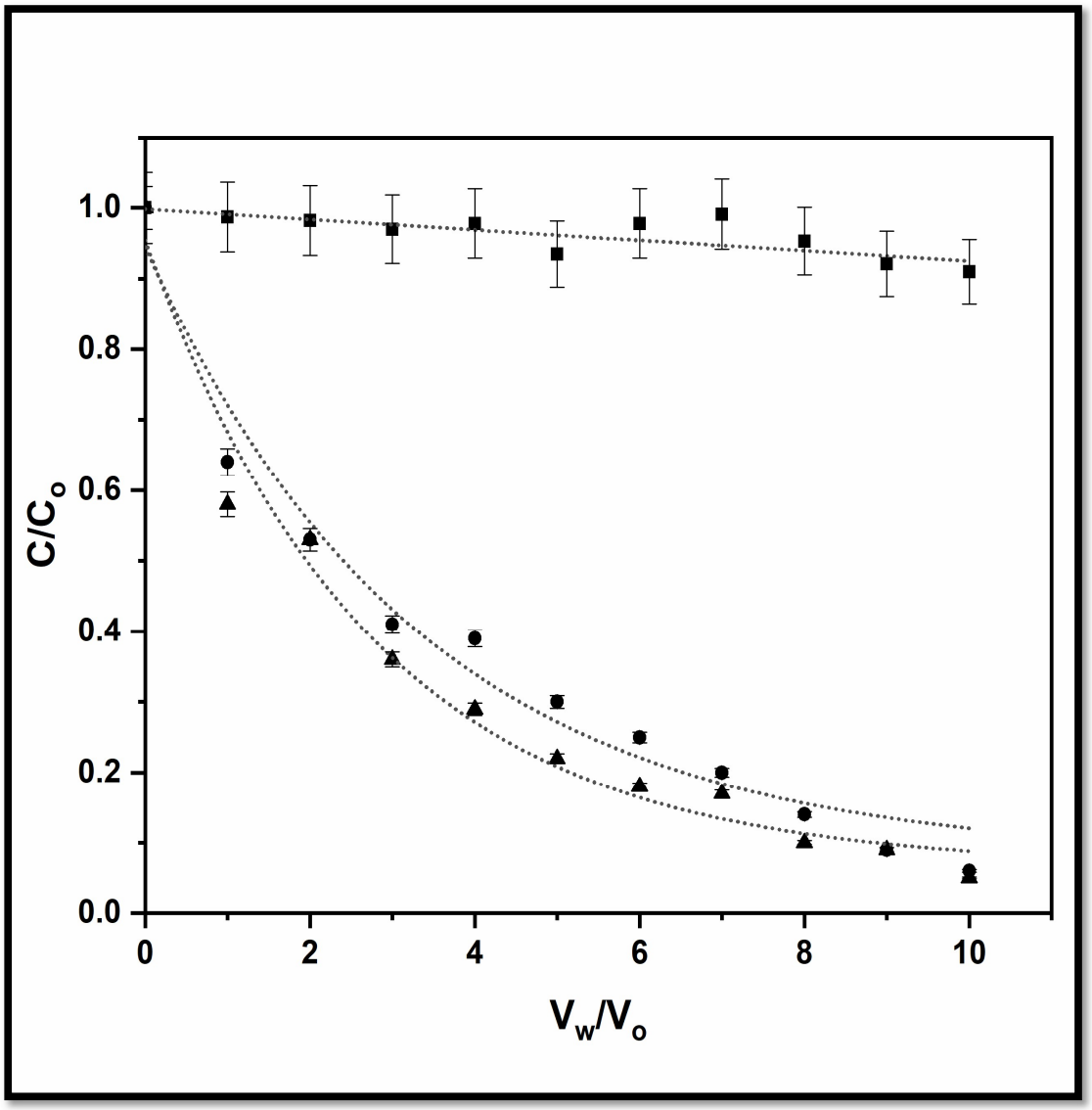

Figure 4.28 Determination of the relative concentrations of HA, microsolutes, and peptides/proteins was made during DF (300 kDa membrane at 1.5 bar of TMP). It represents the number of diavolumes crossing the membrane when V_w/V_o is ratioed. The dotted lines

show the theoretical relative concentrations. The squares represent HA, the circles represent microsolutes, and the triangles represent the concentration of peptides/proteins.

R_{HA}, $R_{proteins\ microsolutes}$, and $R_{minerals\ microsolutes}$ had respective values of 0.96, 0.32, and 0.32. The considerable disparity between the HA molar weight and the 300 kDa membrane cut-off made the high R_{HA} recovery expected. Charged microsolutes retentions and peptides/protein retention rates were very high. HA carboxylic groups, minerals, amino acids, and peptides/proteins are all set at pH 7.

Consequently, it made sense to assume that these solutes' comparatively high retention values were electrostatic interactions with HA, whether at the polarization layer or in bulk, which had this effect. These interactions between salts and minerals have already been demonstrated (Mo et al., 1999). Diafiltration (DF) was used to eliminate the charged microsolutes and peptides/proteins, yet it had a retention value of about 0.2.

Two crucial performance criteria for assessing a separation process are yield and purity. The change in HA production and purity throughout DF in the feed tank is depicted in Figure 4.28. A small amount of HA was depleted, but after ten diavolumes, it rose to 15%, a finding that aligns with the high HA retention.

The purity increased rapidly to 7 diavolumes, stabilizing with an HA yield of 76.69%. Following that, as anticipated, DF was quite effective at filtering HA under these circumstances.

The ratio C/C_o is a straightforward way to determine a solute's yield (η). Considering Eq. (3), the single variable that influences HA yield is its retention, which can be stated as follows (Eq. 4):

$$\eta_{HA} = e^{-(1-R_{HA})\frac{V_W}{V_0}} \quad \text{Eq. 4}$$

The ratio C/C_i determines a solute's purity (P) (In the mixture of the feed tank, I is the i component). In this case, P can be expressed as follows (Eq. 5):

$$P_{HA} = \frac{C_{0HA}\ e^{-(1-R_{HA})\frac{V_W}{V_0}}}{\sum C_{0i}\ e^{-(1-R_i)\frac{V_W}{V_0}}} \quad \text{Eq. 5}$$

R_i is the retention of the i solute, C_{oi} is the initial concentration of the i solute, and C_{oHA} is the initial concentration of HA.

HA is a component that includes charged peptides/proteins and microsolutes. The purity of HA can be estimated at any diavolume following their retention and initial concentration. With retention and starting concentrations of HA (0.96, 1.39 g/L), proteins (0.32, 1.46 g/L), and microsolutes (0.32, 10.58 g/L), equations were used to compare experimentally obtained HA yield and purity to calculated values. (Figure 4.29).

It was interesting to note that the computed and experimental numbers were comparable for both performance criteria. Relative errors did not exceed 6% for HA yield and 14% for purity, respectively. Although experimental values at the end of the procedure were above 100% and computed purities were somewhat lower than experimental, this suggests that the CTAB method (CTM) likely overestimated the concentration of HA.

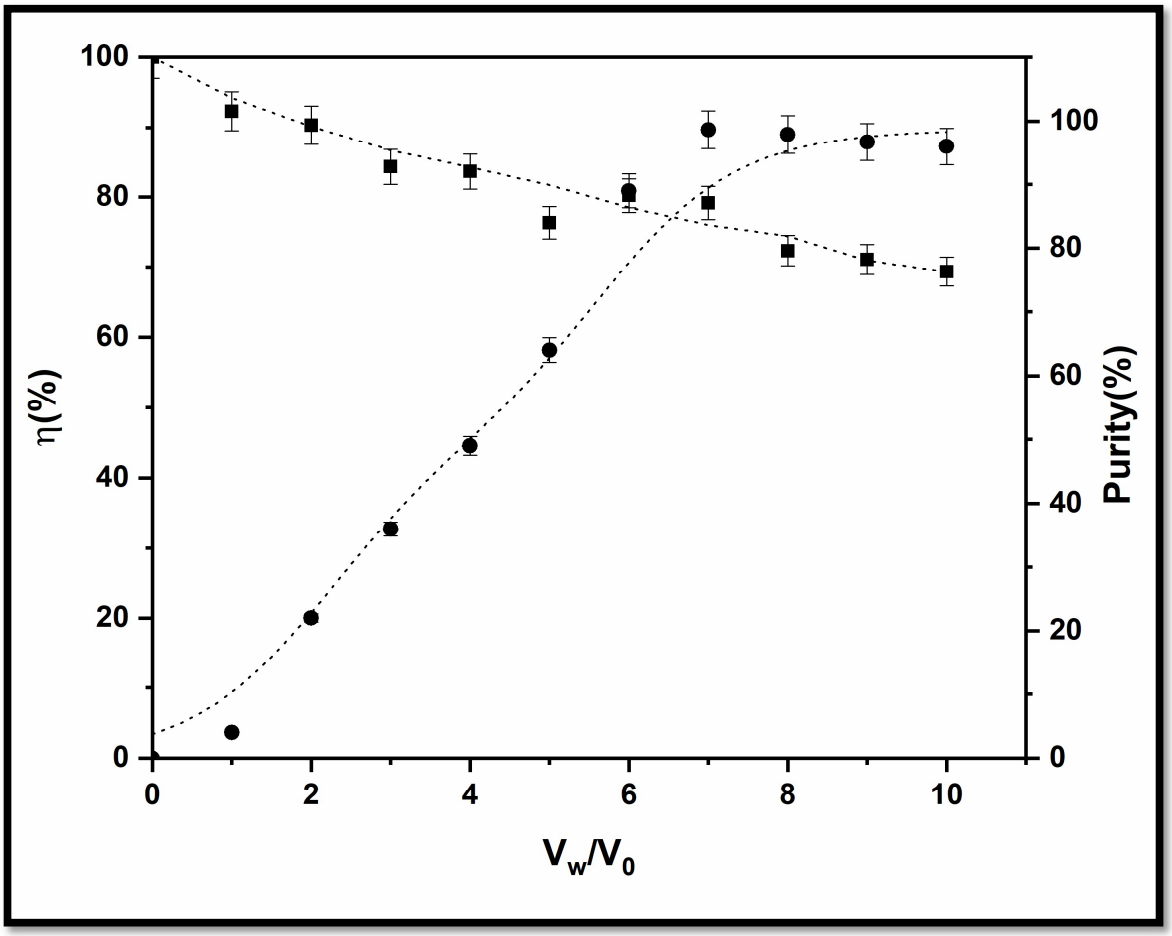

Figure 4.29 Purity (circles) and yield (squares) in the diafiltration process with V_w/V_o (number of diavolumes), theoretical (dotted lines), and experimental (squares and circles).

This work indicates that the assessment of retention and evaluation of the beginning concentrations of peptides/proteins, HA, and dry matter may be used to forecast DF performances for any culture conditions and media. The findings also showed that using 300 kDa membranes significantly reduced the amount of cell proteins and DNA in the permeate.

Higher molecular weight cut-off membrane tends to have a higher rate of permeate flow; this may be because of the removal of the air entrapped in the membrane pores after repeated cycles of diafiltration (Choi et al., 2014).

Diafiltration has been studied in various HA purification studies (Oueslati et al., 2015). Even though diafiltration has been employed in earlier reported studies (Carlino & Magnette, 2002), our approach was more effective because it required minimal solvent dilution and produced HA of higher quality.

Ultrafiltration in the diafiltration mode was used to remove even more contaminants, yielding a final product with a protein content of only 0.8 mg/g, which made it suitable for non-injectable medical applications.

The condensation of the HA retentate to its original volume was done and subsequently performed; vacuum drying was done to obtain the powdered form of HA. These approaches combined result in an intensified purification process with fewer steps, higher efficiency, and robustness. The produced yield of 79.16% was higher than many stated values (Cavalcanti & Santana, 2019).

Because HA is a polymeric molecule, it lacks an ultraviolet (UV) absorption chromophore, making its analysis difficult; CTAB analysis was utilized to identify HA.

4.6. Hyaluronic acid Characterization

4.6.1. High-performance liquid chromatography

HPLC verified the presence of hyaluronic acid in the fermented broth. The peak of hyaluronic acid was harmonized by comparing the sample's retention time to the HIMEDIA standard. There were few polar and nonpolar contaminants in the sample. HPLC examination of Standard hyaluronic acid and the sample revealed a similar chromatogram peak with a nearly identical retention period, as illustrated in Figure 4.30.

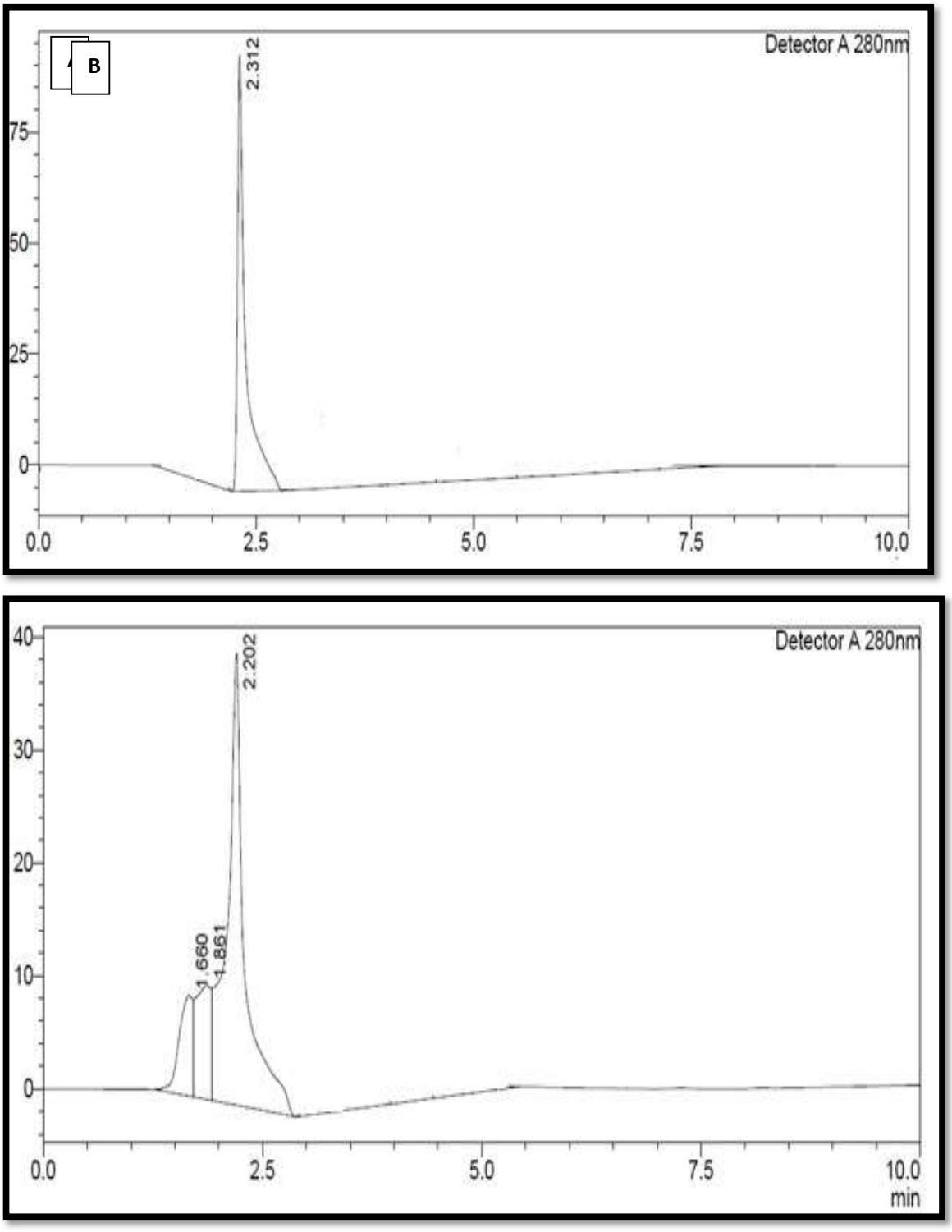

Figure 4.30. HPLC chromatogram of hyaluronic acid (A) Standard (B) fermented broth sample

The chromatogram of the standard HA showed a peak retention time of 2.31 minutes, and the sample showed a retention time of 2.20 minutes. These results are pretty similar to the recent studies of HA detection by HPLC methods (Botha et al., 2018; Kašparová et al., 2018)

4.6.2. FTIR absorption spectra of HA

FTIR spectroscopy can identify functional groups and organic molecules by assessing the transition between the vibrational states of bonds. Experimental and standard HA samples were compared using FTIR spectra (Figure 4.31).

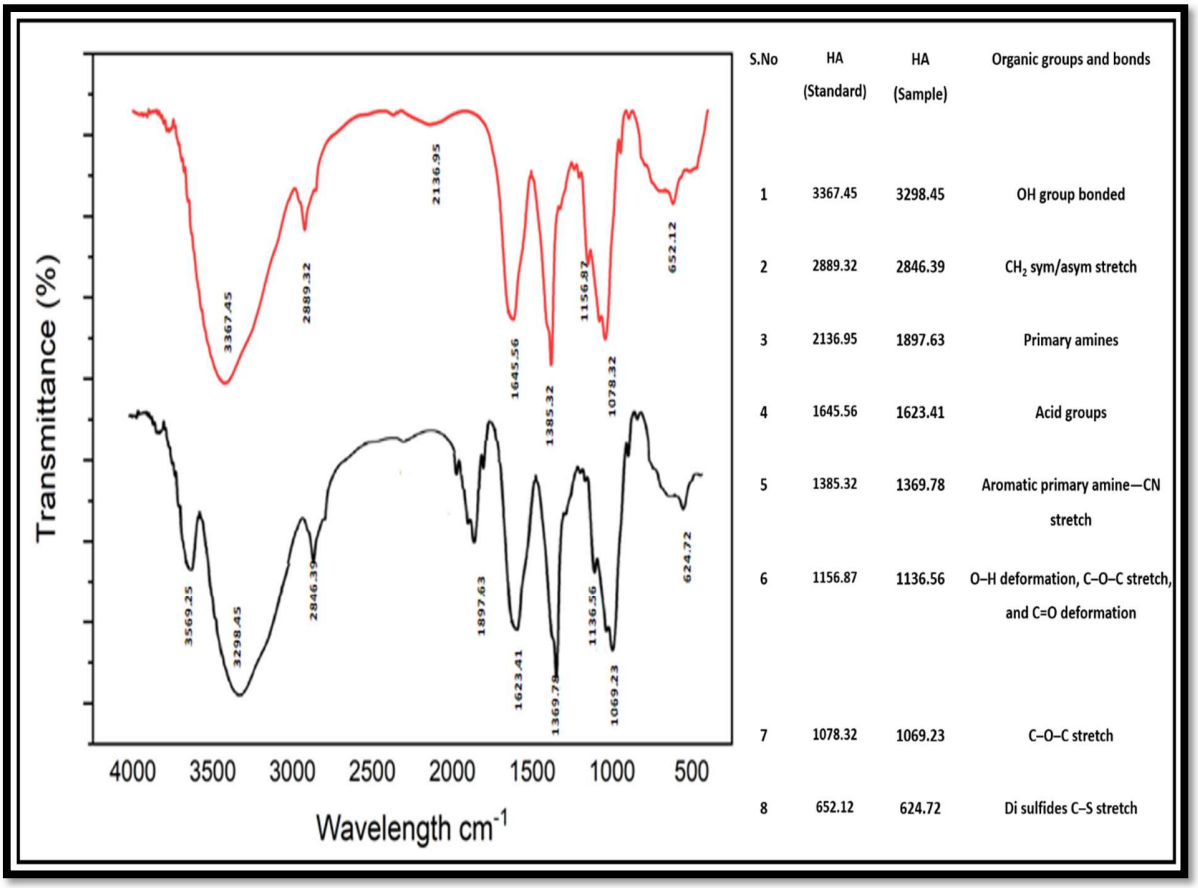

S.No	HA (Standard)	HA (Sample)	Organic groups and bonds
1	3367.45	3298.45	OH group bonded
2	2889.32	2846.39	CH_2 sym/asym stretch
3	2136.95	1897.63	Primary amines
4	1645.56	1623.41	Acid groups
5	1385.32	1369.78	Aromatic primary amine—CN stretch
6	1156.87	1136.56	O–H deformation, C–O–C stretch, and C=O deformation
7	1078.32	1069.23	C–O–C stretch
8	652.12	624.72	Di sulfides C–S stretch

Figure 4.31 FTIR spectrum showing the peaks of the functional groups present in the standard HA (red) and purified sample (black)

There were numerous peaks in the standard sample, including 1369, which stated a C–O functional group, and 624 and 1069, which indicated a C-O-C link. The amide two functional groups were represented by the 1623 wavelength, whereas the 2892 wavelength represented C–H bonds.

The existence of OH was confirmed by Peak 3298. All of these were the purified and control samples, respectively.

4.6.3. Mass spectrometry

Its viscoelastic properties are attributed to oligosaccharides generated from HA breakdown; using mass spectrometry to study HA is still tricky. (Kenne et al., 2013). According to a study (Kühn et al., 2003) utilizing an ESI-ion trap mass spectrometer, the HA molecules are multiply charged under ESI conditions, making the spectra much more challenging to decode.

According to the ESI-tandem MS data, odd-numbered oligomers split off glucuronic acid as [M-H-H_2O], m/z=149, whereas even-numbered oligomers lost one molecule of N-acetyl glucosamine as [M-H-H_2O], m/z=215.

HA showed a wide range of fragmentation of oligosaccharide patterns with variable chain lengths and relative intensities spanning from the hyaluronic acid basic unit (m/z 301) to more than 16-mers in this study.

Except for a few peaks in the upper m/z range, most hyaluronic acid ions were found below m/z 500, according to the results in Figure 4.32.

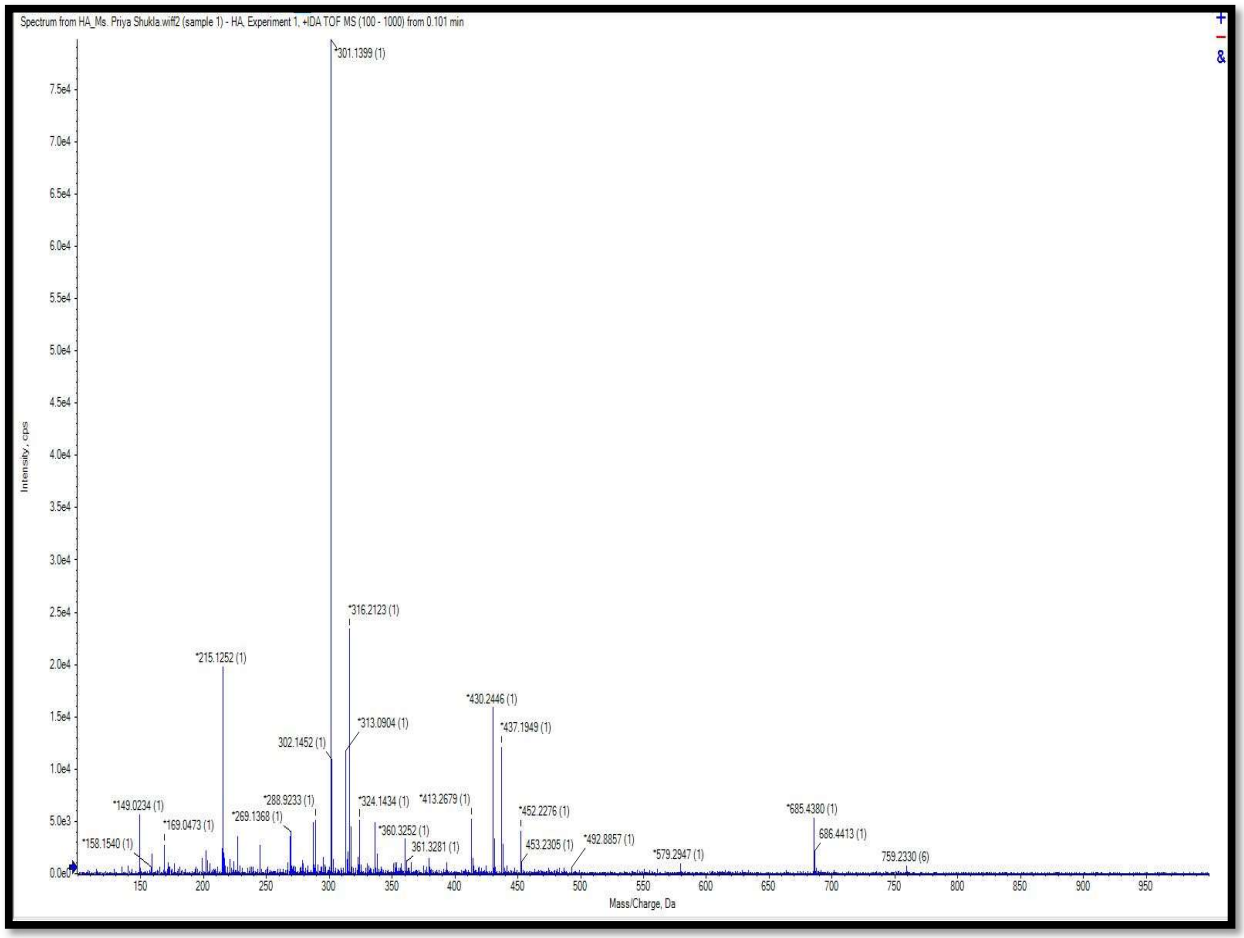

Figure 4.32. The ESI-MS profile for the HA sample

4.6.4. Scanning electron microscope

High-resolution images from SEM analysis are obtained, allowing one to see morphologic details while maintaining analytical accuracy. A scanning electron microscope showed that the HA appeared as a sponge with volumetric pores.

Furthermore, the surface has a high porosity because of the impedance of an abundance of inflated fibers and blindly ending, analogous to the fungus hyphae (Figure 4.33). The HA

comprises numerous layers of threads, each cylindrical and blind-ended, as revealed by the SEM.

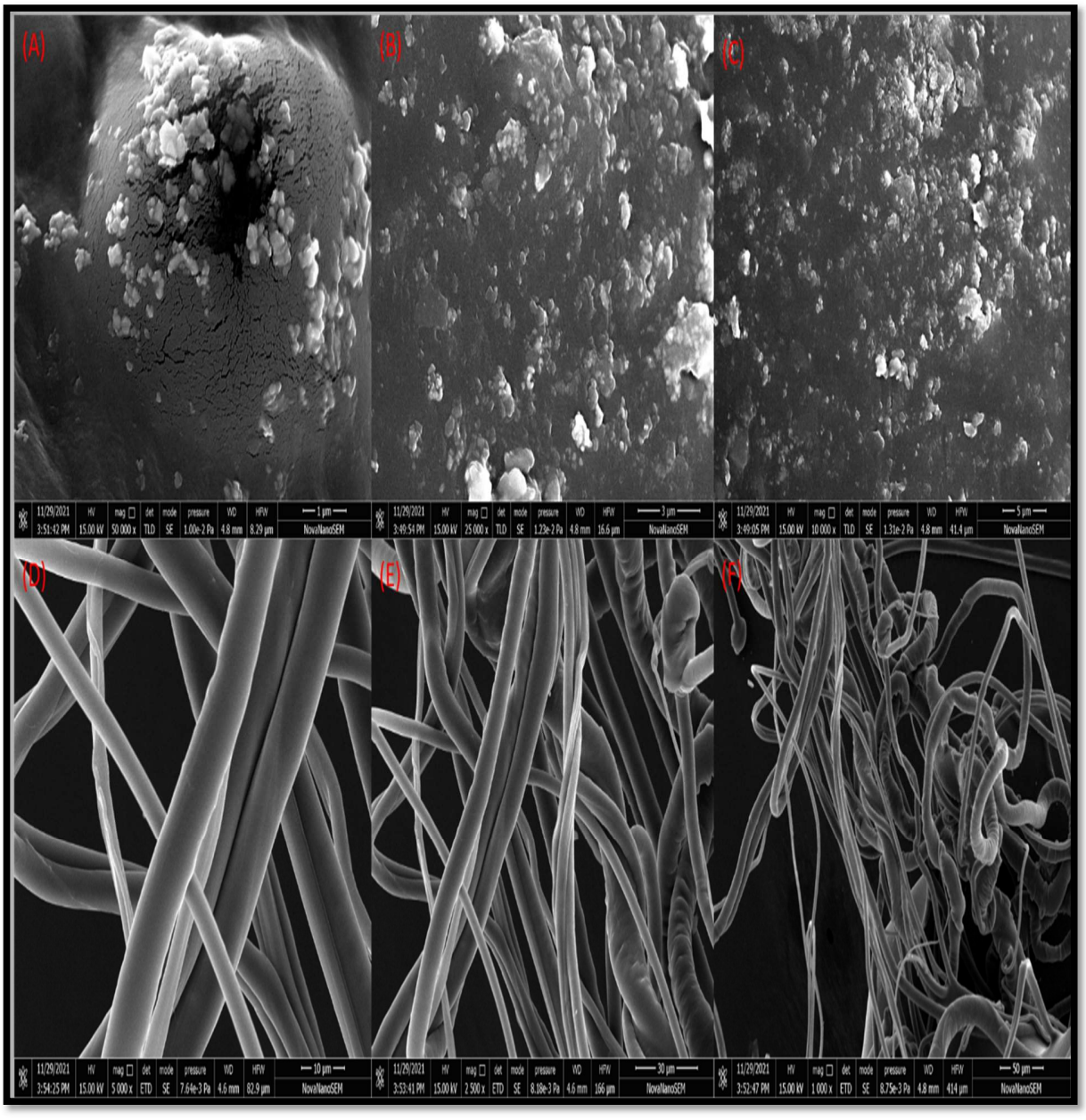

Figure 4.33. Scanning Electron Microscope images of purified hyaluronic acid at different resolutions ranging from 1- 50 µm; (A) 1 µm, (B) 3 µm, (C) 5 µm, (D) 10 µm, (E) 30 µm and (F) 50 µm

4.6.5. X-ray diffraction studies of HA

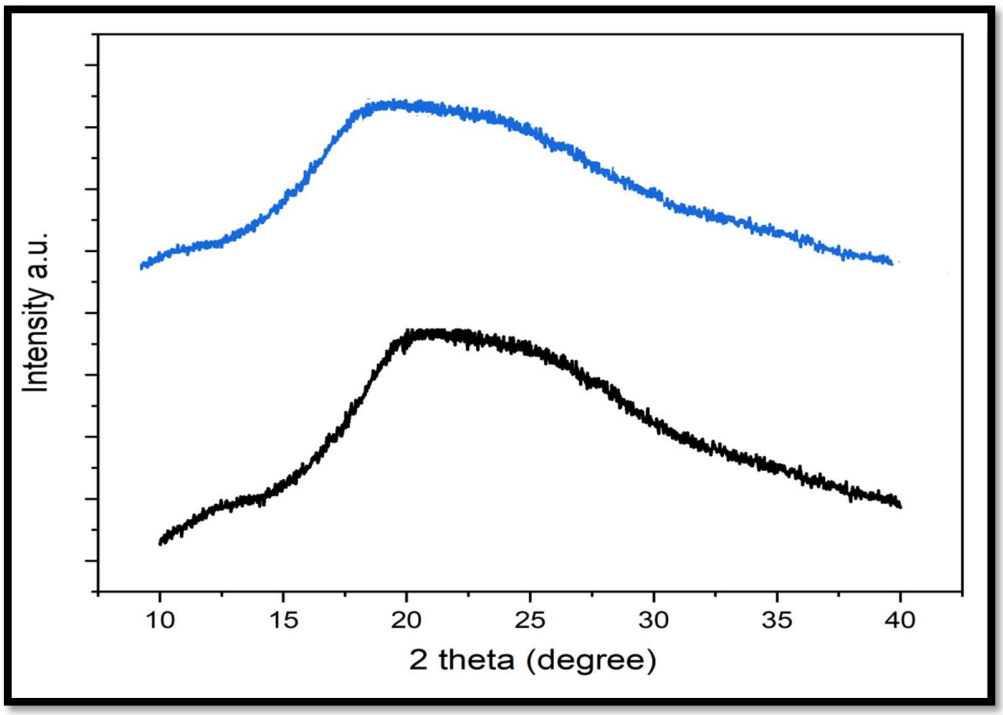

Figure 4.34. XRD graphs of the purified HA (black) from *Streptococcus zooepidemicus* MTCC 3523 and the standard HA (blue)

X-ray diffraction patterns revealed that the tested sample and standard had the same structure and morphology as semi-hydrated fibers and validated HA's non-crystalline/amorphous configuration. Figure 4.34 compares the XRD of the HA produced by the *Streptococcus zooepidemicus* MTCC 3523 strain to the standard.

4.6.6. Proton nuclear magnetic resonance studies

Protons in the sugar ring exhibit signals like those seen in the broad HA spectrum (Figure 4.35) between 3.0 and 4.0 ppm. The signals were superimposed, making it difficult to assign each proton to its proper location. On the other hand, signals were assigned to protons in the

sugar rings that corresponded to them. The methyl (-CH_3) protons of HA's N-acetyl group produced a signal at 1.9 ppm. An unusual signal is produced by the two anomeric protons coupling to the carbons close to the two oxygen atoms at 4.6 ppm.

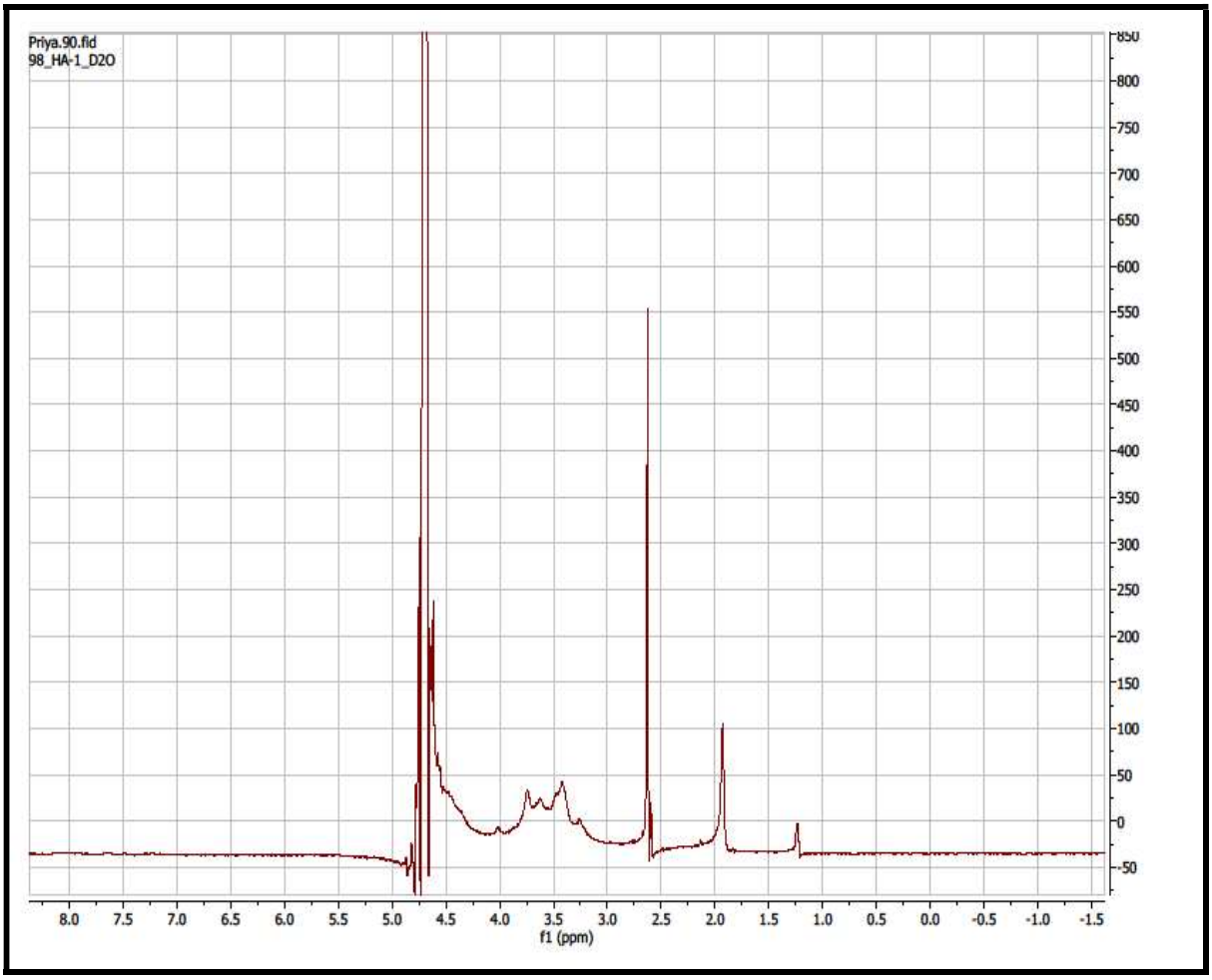

Figure 4.35 ^{1}H NMR spectrum of purified HA from *Streptococcus zooepidemicus* MTCC 3523

4.6.7. Thermogravimetric analysis

Because biomaterials like HA must be sterilized at high temperatures before use, thermal stability is crucial (Wang et al., 2020). Figure 4.36 displays the sample's TGA curves.

According to Vasi *et al.* findings, mass loss was seen to occur in both samples in four stages (Vasi et al., 2014). When assessing the mass losses at each stage, the purified HA had superior thermal stability because the HA samples had minor mass variation. Figure 4.36 displays the residue at 800 ºC (the analysis end temperature) and the mass loss percentage for each stage of degradation. Dehydration is undoubtedly a factor in the initial step. Thermogravimetric measurements of HA cause a slight weight loss during the initial stages; even though HA samples were arid before the analysis, H_2O molecules attached to them by hydrogen bonds evaporated during the process (Coimbra et al., 2011).

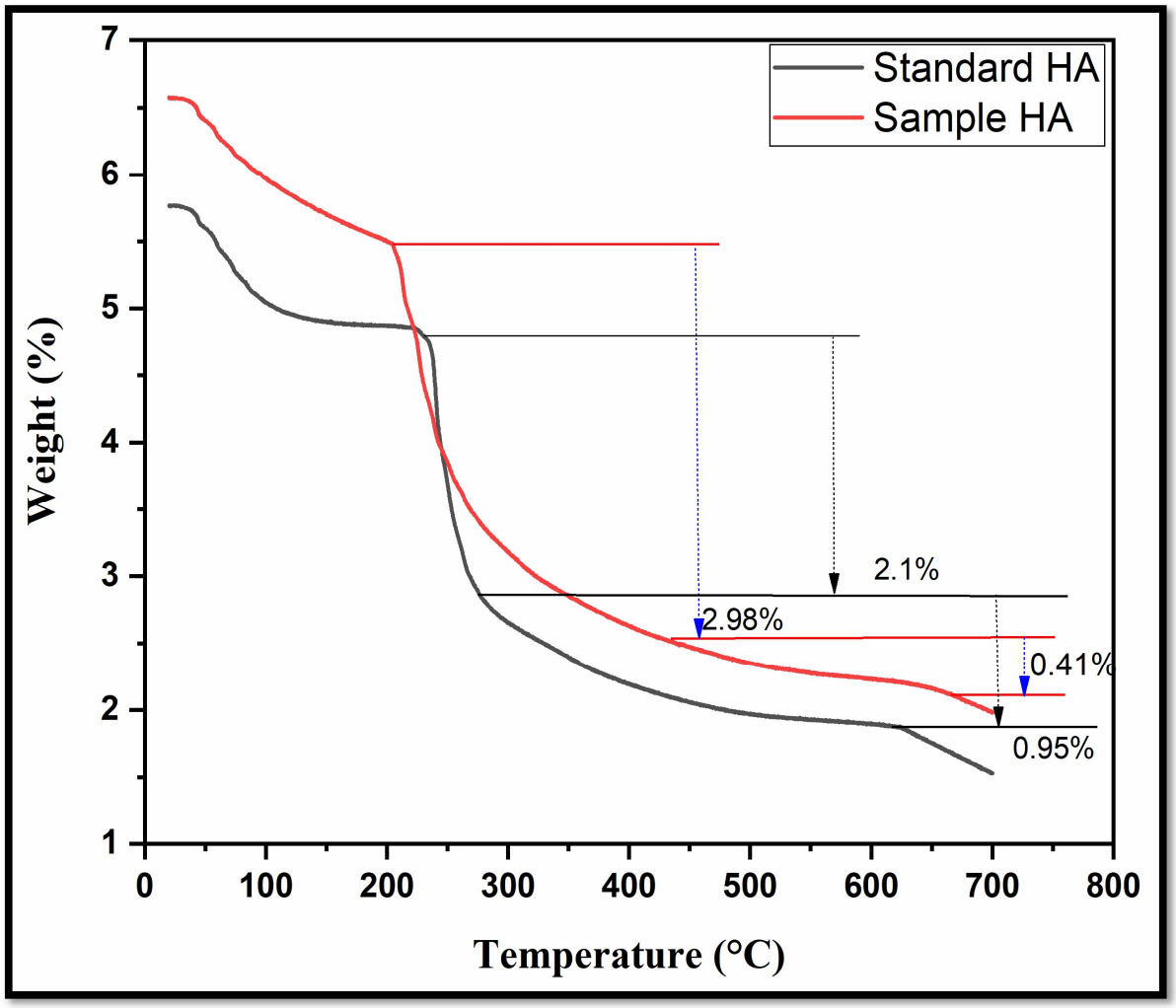

Figure 4.36. TGA analysis of standard (black) and microbially produced HA sample (red).

At 270 ºC, pure HA degrade (Lin et al., 2019). In addition to physicochemical properties and hydrogen bonding capability, covalent bonds may be responsible for the disparity in the thermal deportment between the materials. All this confers more significant structural durability to the hyaluronic acid polymer than the electrostatic interaction of sodium hyaluronate, which leads to decreased mass damage during thermal deportment (Vasi et al., 2014). HA residue at 800 ºC in the TGA curves indicates excellent thermal stability for *S. zooepidemicus* HA.

4.7. Antioxidant capacity

To explain the antioxidant characteristics of polysaccharides (like HA), numerous processes must be considered, including preventing chain initiation, reducing capacity, radical scavenging, binding of transition metal ion catalysts, and peroxide breakdown (Ke et al., 2009). Due to this, several techniques were used to assess the antioxidant activities of the samples, including those that prevent initiation (reducing potential and total antioxidant capacity), termination (hydroxyl, DPPH, and superoxide scavenging), and propagation (iron chelating).

The total antioxidant capacity (TAC) measures a substance's potential to provide an additional molecule with an electron, stabilizing it (Galinari et al., 2018).

Compared to standard HA (12.17 ± 0.36 g AAE/g), *S. zooepidemicus* produced HA with a higher TAC (13.32 ± 0.52 g AAE/g). By donating electrons or hydrogen atoms to free radicals, a compound has a reducing potential. It stabilizes free radicals and prevents radical chain reactions (Galinari et al., 2018).

The findings revealed that HA's lowering power (24.85 ± 0.45%) was more significant than standard HA (22.32 ± 0.14%). However, compared to ascorbic acid, it showed less action.

Similar findings were made by Sadhasivam *et al*. (Sadhasivam et al., 2013), who discovered that the reducing power of the HA sample was comparable to artificial antioxidants at lower concentrations (100-200 µg/mL).

One of the most dangerous ROS, the hydroxyl radical, reduces molecular oxygen in a cascading process that harms DNA, lipids, and proteins (Kanchana et al., 2013). Antioxidant defences against hydroxyl radicals can be divided into two categories: those that suppress hydroxyl radical production and those that scavenge produced hydroxyl radicals (Aquino-Martins et al., 2019).

As a result, HA's iron chelating and hydroxyl radical scavenging abilities were assessed.

Important pro-oxidant substances like iron and copper ions can catalyze the Fenton reaction when they interact with hydrogen peroxide to create hydroxyl radicals (Aquino-Martins et al., 2019). An antioxidant molecule would chelate iron ions, suppressing Fenton reactions by preventing oxidative damage (Rolim et al., 2018).

Polymers containing cross-linked carboxylic groups can chelate metal ions, according to Pan *et al*. (45). However, this activity was not observed in the analyzed samples. The lack of carboxylic groups in the FTIR study can be used to explain the lack of iron-chelating activity.

According to the results of the hydroxyl radical scavenging test, the HA sample inhibited 32.03 ± 0.12%, while standard HA only inhibited 17.36 ± 0.65%.

A stable free radical called DPPH frequently calculates how well biomolecules scavenge free radicals (Ke et al., 2009). The hydroxyl and carboxyl groups in polysaccharide structural makeup may be responsible for their capacity to scavenge free radicals, acting as hydrogen donors and minimizing the impact of oxidative stress (Hadidi et al., 2020).

The HA sample achieved 4.87 ± 0.45 Kmol TE/g, and the standard achieved 5.43 ± 0.23 Kmol TE/g in the DPPH radical scavenging test. Pan *et al.* reported that bacterial HA exhibited a scavenging DPPH of 41% at 1.0 g/L (Pan et al., 2017).

Furthermore, Ke et al. found that lower molecular weight hyaluronic acid scavenges the most outstanding amount of DPPH radicals at 59.38% (Ke et al., 2009). However, the superoxide radical scavenging test in the current investigation revealed almost negligible action for both standard and purified HA (0.003 ± 0.001%).

4.8. Hyaluronic acid as an antibacterial agent

4.8.1. Molecular Docking

Ampicillin and hyaluronic acid were tested using molecular docking to see if they might bind to the *S. aureus* and *E. coli* tyrosyl-tRNA synthetase ligand-binding sites topoisomerase II DNA gyrase proteins, respectively. The findings are presented in the following sections.

4.8.1.1. Molecular docking results with tyrosyl-tRNA synthetase

The tyrosyl-tRNA synthetase protein from *S. aureus* had a well-preserved binding domain with good binding energy values (Table 4.6, 4.7). The catalytic binding site of 1JIL has GLY 38, HIS 50, LEU 70, THR 75, ASP 80, GLN 174, ASP 195, and GLN 196. These amino acids are represented mainly within the defined grid box.

The binding energies of hyaluronic acid and the positive control ampicillin were -6.13 Kcal/mol and -9.63 Kcal/mol, respectively, whereas the kI values were 32.17 µM (hyaluronic acid) and 86.79nM (Ampicillin). Strong interactions between the molecule and the proteins, such as hydrogen bonds and hydrophobic and salt bridges, were observed. GLY 38, THR 42

(3), HIS 50, ASP 80 (2), GLY 193, ASP 195, and GLN 196 are the amino acids forming hydrogen bonds between the protein and hyaluronic acid.

GLN 196 was involved in the hydrophobic interaction with hyaluronic acid, and LYS 84(2) and ARG 88 took part in the salt bridge development. The total participation of amino acids in various interactions and the binding energies are reported in Table 4.7. The binding energy and the interaction patterns between the test molecule and positive control are comparable, suggesting hyaluronic acid to be a good alternative for overused resistant antibiotic ampicillin.

In molecular docking, optimal binding energy and well-conserved binding region were detected for the *E. coli* tyrosyl-tRNA synthetase protein. The ligand-binding pocket of 2YXN has GLY39, ASP41, GLY50, GLY198, ASP200, GLN201, HIS51, VAL53, ILE228, PHE236, and ARG89 amino acids. Many of these amino acids participated in hydrogen bond formation, hydrophobic interactions, and non-covalent bonds.

In the case of hyaluronic acid and ampicillin, binding energies were -5.79 Kcal/mol and -9.82 Kcal/mol, respectively. However, their inhibition constants are 56.95 μM and 63.77 nM, respectively.

Hyaluronic acid showed a lot more hydrogen bond formation with the help of amino acids GLY39 (2), ASP41 (2), GLY50, GLY198, ASP200 (2), and GLN201, as compared to ampicillin. ASP 41 participated in the hydrophobic interactions, and a salt bridge formation also took place with the help of HIS 51 in hyaluronic acid and ARG 49 in Ampicillin. Varied interaction patterns of hyaluronic acid compared to ampicillin suggest the potential antibacterial activity of hyaluronic.

4.8.1.2. Molecular docking results with topoisomerase II DNA gyrase

In molecular docking, the topoisomerase II DNA gyrase protein of *S. aureus,* a well-preserved binding domain with optimal binding energy values, was reported (Table 4.6, 4.7). There are ASN46, LEU125, ASP130, ILE 131, ASN132, LYS133, and ARG129 amino acids in the ligand-binding pocket of 5CDP. This amino acid spectrum involves hydrogen bond formation, hydrophobic interactions, and non-covalent bonds. The binding energies of hyaluronic acid and ampicillin were -5.02 Kcal/mol and -8.01 Kcal/mol. Nevertheless, they have inhibition constants of 207.69 µm and 1.34 µm, respectively. ASN46 (2), LEU125, ASP130 (3), ILE131, ASN 32 (2), and LYS133 played a part in the hydrogen bond formation between hyaluronic acid and the protein.

Table 4.6. A description of the docking proteins, their coordinates, and docking locations

S.No.	Protein (PDB ID)	X,Y,Z Coordinates	NPTS
1	1JIL	30.779, 11.547, 87.68	56, 72, 88
2	2YXN	7.562, 28.837, 20.042	68, 48, 82
3	5CDP	-27.022, -26.33, -32.405	94, 94, 82
4	6RKS	-27.022, -26.33, -32.405	94, 94, 82

Table 4.7. An overview of the types of ligand interactions, including interactions involving binding energy and intermolecular energy, as well as inhibitor constants

S.no.	Ligand	Binding Energy	Ki	Protein	Hydrogen bonds	Hydrophobic bonds	Salt Bridges
1	Ampicillin	-9.63	86.79nM	1JIL	GLY 38, THR 75, ASP 80, GLN 174, ASP 195, GLN 196	TYR 36, HIS 50, PRO 53, PHE 54, LEU 70, GLN 174	HIS 50
2	Hyaluronic Acid	-6.13	32.17µM	1JIL	GLY 38, THR 42 (3), HIS 50, ASP 80 (2), GLY 193, ASP 195, GLN 196	GLN 196	LYS 84 (2), ARG 88
3	Ampicillin	-8.01	1.34µM	5CDP	ASN 46 (2), LEU 125, GLU 126, ARG 471	ARG 129, ILE 131	
4	Hyaluronic Acid	-5.02	207.69µM	5CDP	ASN 46 (2), LEU 125, ASP 130 (3), ILE 131, ASN 132 (2), LYS 133	LEU 125A (2), ARG 129A	LYS 133A

5	Ampicillin	-9.82	63.77nM	2YXN	GLY 50A, GLY 198A, SER 199A, ASP 200A, PRO 226A	VAL 53A, ILE 228A (2), PHE 236A	ARG 89A
6	Hyaluronic Acid	-5.79	56.95µM	2YXN	GLY 39A (2), ASP 41A (2), GLY 50A, GLY 198A, ASP 200A (2), GLN 201A	ASP 41A	HIS 51A
7	Ampicillin	-6.59	14.73µM	6RKS	GLU 47A, ASP 1134A	ASN 132A, PHE 138A, ARG 147A	
8	Hyaluronic Acid	-4.9	253.89µM	6RKS	ASN 46A (2), LEU 125A, ASP 130A, ASN132A	THR 51A,LEU 125A	LYS 133A

LEU 125(2) and ARG129 were indulged in the hydrophobic interactions. Non-covalent bonds in the form of the salt bridge were formed with the help of LYS 133, whereas positive control ampicillin showed no covalent interactions. Interestingly, the binding energy and interaction patterns between the positive control and the test molecule are comparable, indicating that hyaluronic acid is an alternative to overused ampicillin.

The topoisomerase II DNA gyrase protein of *E. coli* molecular docking results showed a positive response for the ligand-binding region. The catalytic binding site of 6RKS has ASN

46, LEU 125, ASP 130, ASN132, GLU 47, ASP 1134 and LYS 133. Binding energy and ki of hyaluronic acid (-4.9 kcal/mol, 253.89 μM) and Ampicillin (-6.59 kcal/mol, 14.73 μM) were recorded. Hydrogen bonding (ASN 46 (2), LEU 125, ASP 130, ASN132), hydrophobic interactions (THR 51, LEU 125), and non-covalent interaction (LYS 133) are observed between the hyaluronic acid and the protein and are compared with the control ampicillin. It showed a positive result towards hyaluronic acid used as an antibiotic.

4.8.2. Molecular Simulation-

Five different analyses were performed on our simulated complexes to gain deeper insights into our simulation. The overall stability of both apoprotein and apoprotein-ligand complexes was investigated by generating the RMSD trajectory using the gmx_rms tool. During the experiment, the system's gyration radius was determined using the gmx gyrate tool. The number of hydrogen bonds formed between the ligand and the protein on average, which evaluates the apoprotein's stability and protein-ligand interactions, was calculated using the gmx h-bond tool.

4.8.2.1. Simulation of tyrosyl-tRNA synthetase of *S. aureus* (1JIL)

The tyrosyl-tRNA synthetase apoprotein, as well as the ligand complex, were simulated for 50 nanoseconds. The RMSD trajectories generated by JIL-HA complexes converge around 0.2nm compared to 1JIL apoprotein, which converges around 0.3nm. The 1JIL-HA complex trajectory took 20 ns to stabilize and stayed constant throughout the simulation (Figure 4.37).

This kind of RMSD trajectory suggests that the apoprotein tends towards the stabilized state in hyaluronic acid, meaning that interactions between the apoprotein and the ligands are strong enough.

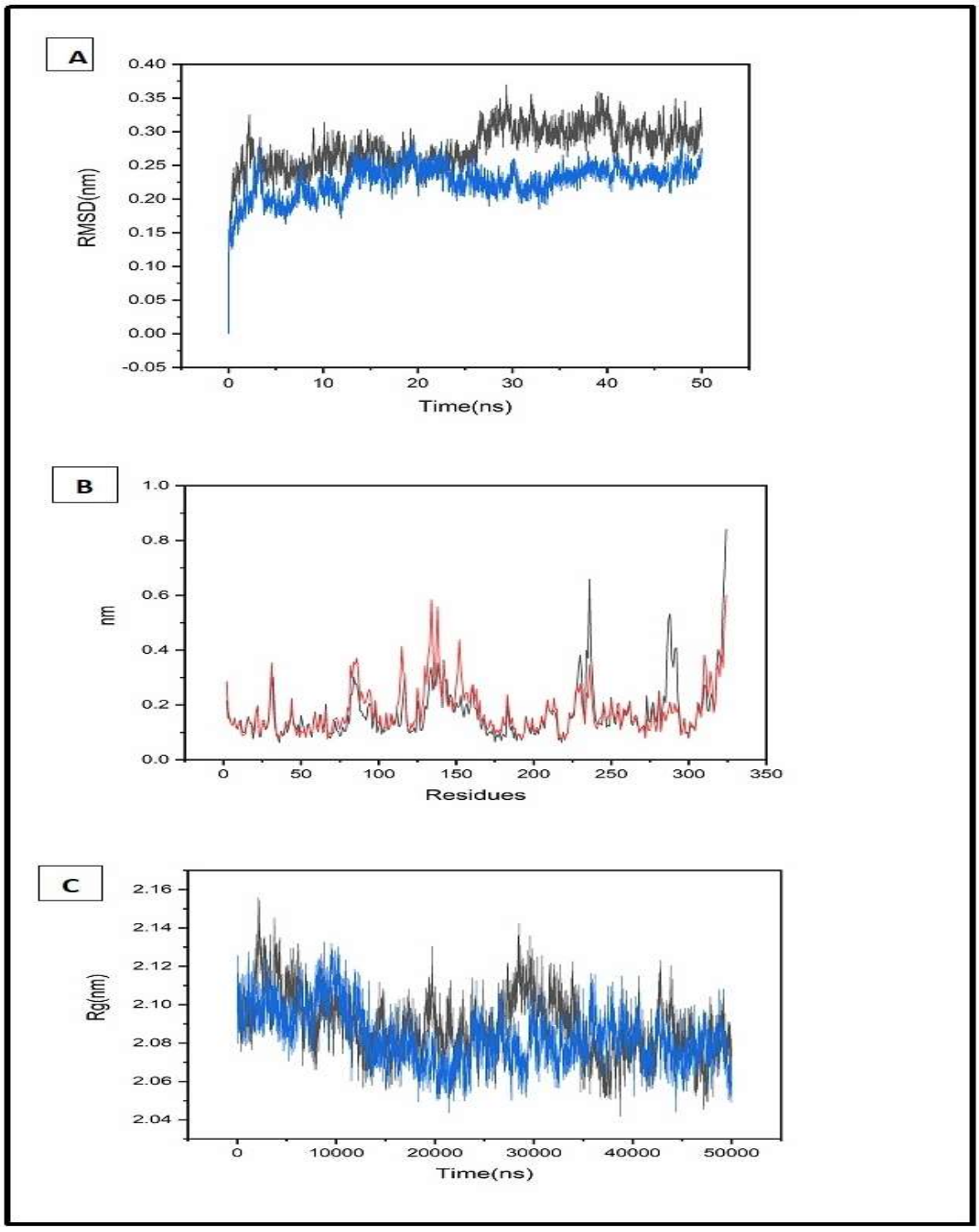

Figure 4.37. (A) RMSD, (B) RMSF, and (C) Radius of gyration of apoprotein (black) and 1JIL-HA complex (blue (RMSD, Rg) and red (RMSF)

Further RMSF analysis lowers overall residues of the 1JIL-HA complex compared to the apoprotein RMSF, which complements our RMSD analysis. The lowering of the RMSF trajectory in the presence of the ligand shows that the interaction with the ligand helps the apoprotein stay more folded than the native one. The radius of gyration of 1JIL-HA complex trajectories indicates that our protein is becoming more compact in the presence of hyaluronic acid, which was earlier suggested by our RMSD and RMSF trajectories.

4.8.2.2. Simulation of tyrosyl-tRNA synthetase of *E. coli* (2YXN)-

Similar simulation studies were performed for 2YXN and 2YXN-HA complexes for 50 ns. The RMSD trajectory of the complex, in comparison to the apoprotein, showed lower stability. The trajectory of the apoprotein converges somewhere around 0.2nm and 0.3nm, whereas the complex trajectory showed more fluctuations connecting about 0.5nm and 0.6nm. The ligand apoprotein trajectory took approximately 30 ns to attain stability; a slight deviation was observed around 45 ns, but it became stable at the end of the simulation. However, the apoprotein seemed more stable in a similar environment than the 2YXN-HA complex (Figure 4.38). RMSF trajectory also showed responses identical to RMSD. Irrespective of the few residues, the complex mostly encouraged randomness, indicating that protein may lose its original conformation and activity due to hyaluronic acid at its binding site.Furthermore, the radius of gyration supported our RMSD and RMSF studies (Figure 4.38). The randomness in the complex is particularly more visible after 30 ns, and more fluctuations are observed around 40 ns. In comparison, the stability in the apoprotein is clearly shown after 30 ns. The overall loss in strength and the protein's compactness in the presence of the ligand hyaluronic acid indicates significant conformational changes within the protein that could inhibit the enzyme function.

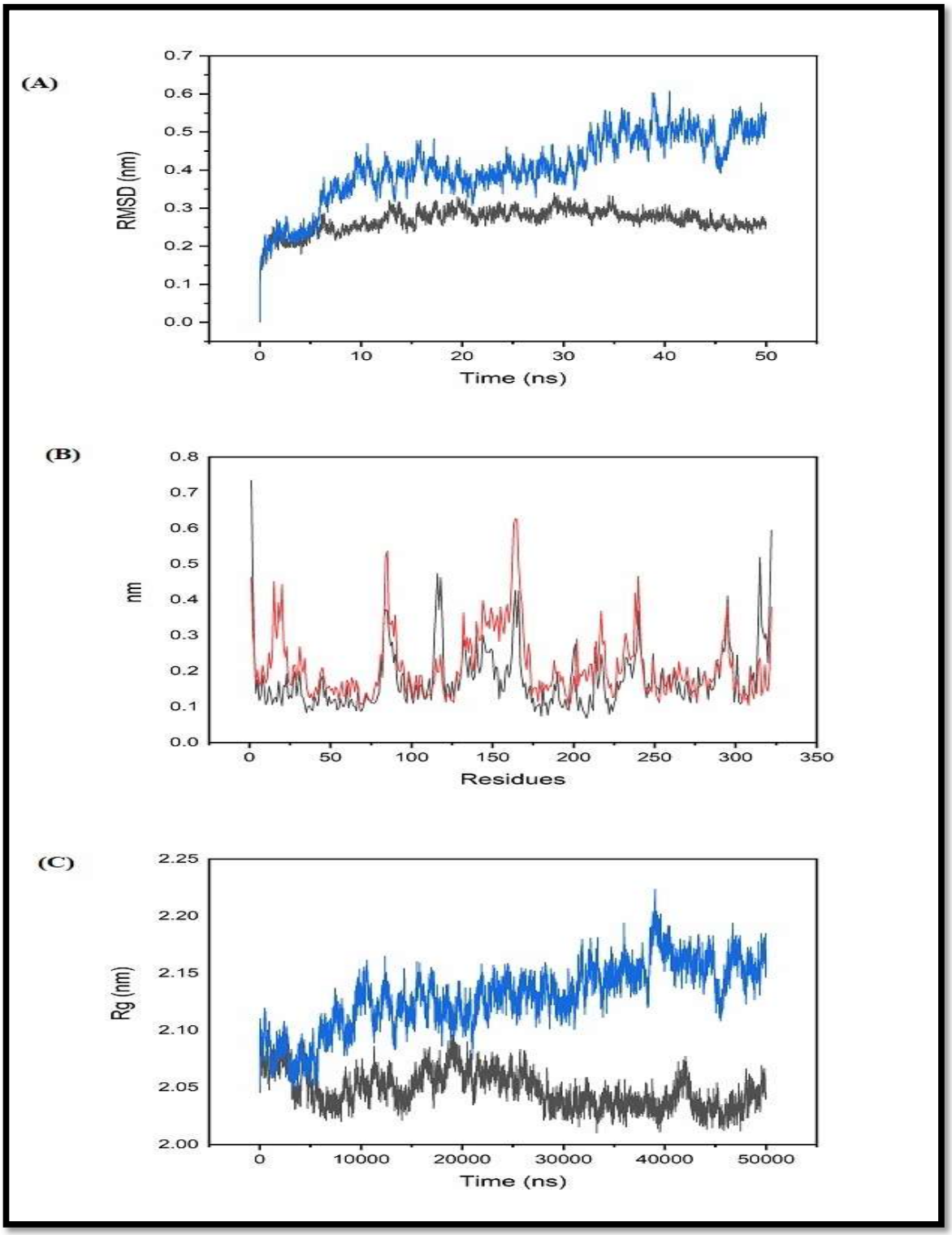

Figure 4.38. (A) RMSD, (B) RMSF, and (C) Radius of gyration of apoprotein (black) and 2YXN-HA complex (blue (RMSD, Rg) and red (RMSF).

4.8.2.3.Simulation studies of topoisomerase II DNA gyrase of *S. aureus* (5CDP)-

The simulation results of the 5CDP apoprotein and the complex with HA demonstrated enhanced complex stability compared to the apoprotein. The apoprotein's trajectory converges at 0.6nm, but the complex's trajectory is more stable at 0.4nm.

The ligand apoprotein trajectory took around 20 ns to stabilize; however, towards the end of the simulation, both the apoprotein and the complex displayed modest variability. However, the apoprotein ligand complex appeared more stable in the same environment than the apoprotein itself.

This type of RMSD trajectory indicates that the apoprotein is going toward a steady state in hyaluronic acid, implying that the apoprotein-ligand interactions are sufficiently strong.

Further RMSF analysis, which complements our RMSD analysis, shows that the 5CDP-HA complex has less overall randomness than the apoprotein. The lowered RMSF trajectory (Figure 4.39) in the presence of the ligand indicates that the interaction with the ligand aids the apoprotein in remaining in a more folded shape than in its native state.

The radius of gyration of 5CDP-HA complex trajectories reveals that our protein is getting more compact in hyaluronic acid, as our RMSD and RMSF trajectories predicted. The radius of gyration of apoprotein converges around 3.8 nm, whereas the 5CDP-HA complex has around 3.2 nm, which shows a high level of difference in compactness.

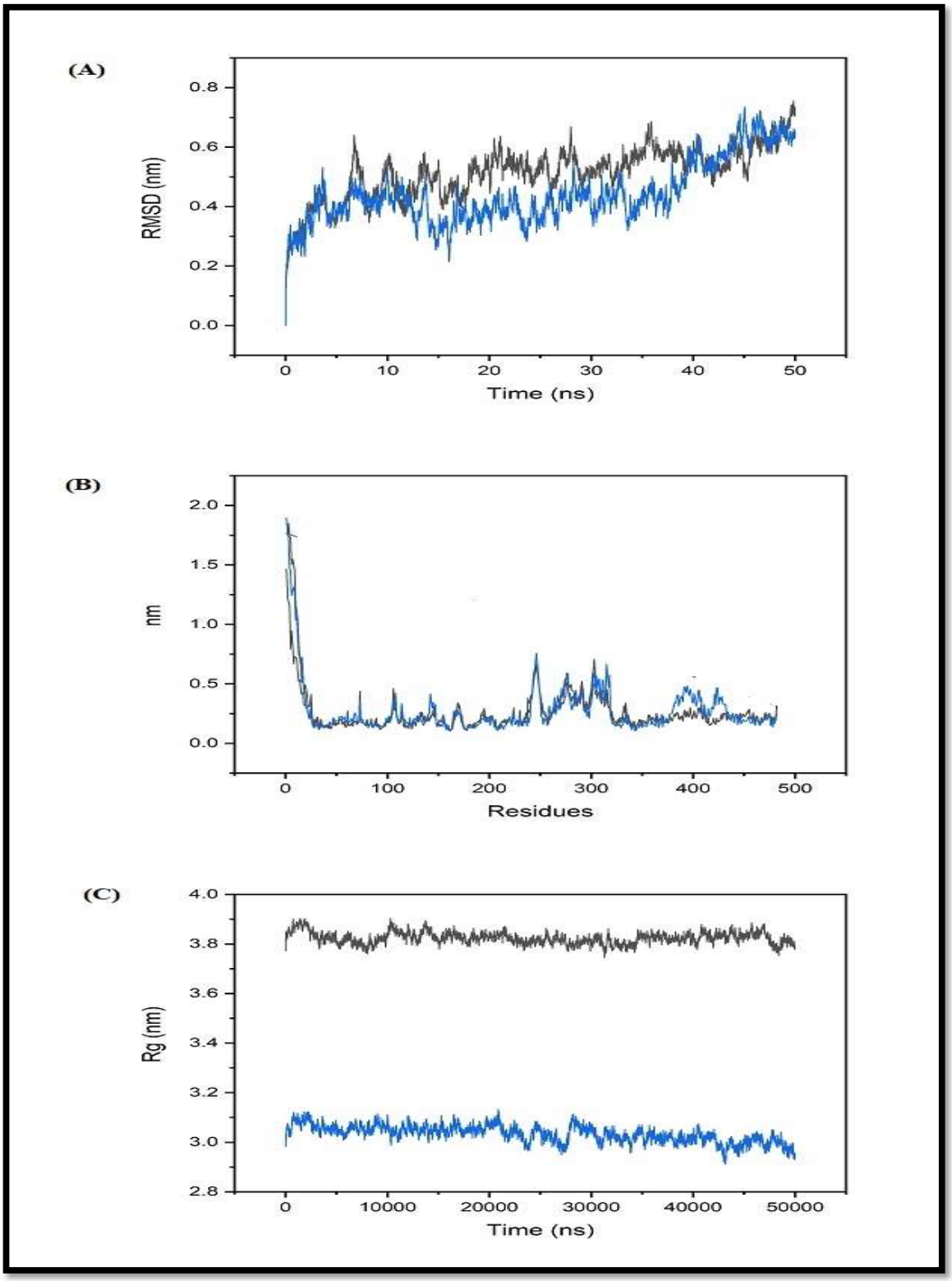

Figure 4.39. (A) RMSD, (B) RMSF, and (C) Radius of gyration of apoprotein (black) and 5CDP-HA complex (blue)

4.8.2.4.Simulation studies of topoisomerase II DNA gyrase of *E. coli* (6RKS)-

The RMSD analysis of the topoisomerase II DNA gyrase (6RKS) and the 6RKS-HA complex demonstrated improved stability compared to the apoprotein (Figure 4.40). While the trajectory for apoproteins tends to converge at 0.6nm, the trajectory for complexes is stable, coinciding at 0.4nm.

The 6RKS-HA complex attained stability around 20 ns contrary to fluctuations in the apoprotein till 30 ns with further during the end. However, the apoprotein ligand complex proved more stable than the apoprotein itself.

This type of RMSD trajectory suggests that the apoprotein is approaching a steady state in hyaluronic acid, showing that the apoprotein-ligand interactions are sufficiently strong. Further, RMSF analysis, which validates our RMSD analysis, indicates that the 6RKS-HA complex has fewer overall residual fluctuations than the apoprotein.

The lowered RMSF trajectory in the presence of the ligand demonstrates that the interaction with the ligand aids the apoprotein in remaining in a more folded shape and provides stability. The radius of gyration of 6RKS-HA complex trajectories reveals that our protein becomes more compact in the presence of hyaluronic acid, as suggested by our RMSD and RMSF trajectories.

The apoprotein gyration radius is roughly 3.8 nm, while the 5CDP-HA complex has a radius of around 3.0 nm, indicating a significant difference in compactness.

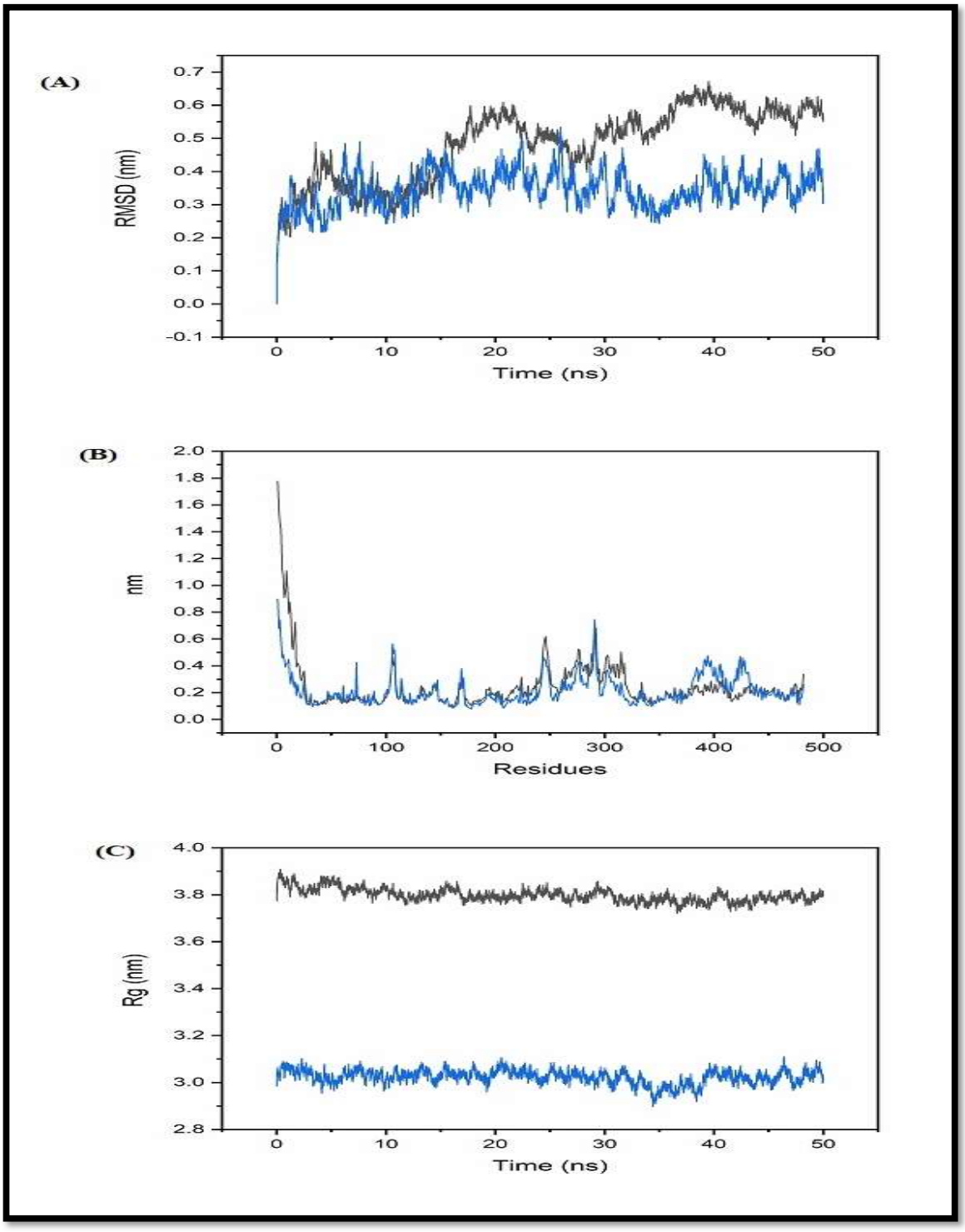

Figure 4.40. (A) RMSD, (B) RMSF, and (C) Radius of gyration of apoprotein (black) and 6RKS-HA complex (blue).

4.8.3. Hydrogen bonding, SASA, and MM/PBSA energy analysis

The solvent-accessible surface area of various complexes with hyaluronic acid decreased the overall SASA, except for the 2YXN complex with HA, which showed a slight increase in the SASA (Table 4.8, Table 4.10). In the presence of HA, an increase in SASA suggests that the protein's compactness is diminishing.

The decrease in compactness compliments our other analyses, which show the general tendency of the protein to lose confirmation in the presence of HA. The other proteins (1JIL, 5CDP, and 6RKS) show a significant decrease in HA, indicating an overall increase in the protein's compactness in the presence of the ligands. The presence of ligands in these proteins stabilizes the overall conformation of the proteins.

Hyaluronic acid-protein interactions are governed to a significant amount by forming stable hydrogen bonds. Hydrogen bonding between protein and ligand is essential for the ligand’s overall affinity for the protein binding site. Across all the proteins, HA forms 2-3 hydrogens (Table 4.9) bonds, maximum up to between 4-5 in the case of 1JIL and 2YXN. The impact of the hydrogen bonding is diverse across the proteins, as HA has been responsible for both providing stability and causing instability to the protein conformations.

In addition, the free energy analysis was used to figure out which complex has the best overall binding energy. Table 4.10 summarises the energy analysis. In terms of free binding energy, 1JIL-HA has overall binding energy of -85.45 ± 12.62 kJ/mol, which is the highest of all of them, followed by 2YXN-HA with -49.90 ± 64.19 kJ/mol, 5CDP-HA with -47.28 ± 13.92 kJ/mol and 6RKS-HA has one of -45.30 ± 21.33 kJ/mol.

Both the tyrosyl-tRNA synthetase complexes have incredible binding energy compared to topoisomerase II DNA gyrase complexes. The most influential contribution to these values is Van Der Waal's force. Higher Van Der Waal's force implies the role of a more hydrophobic environment around the complexes, favoring the complexes' stability and overall protein folding. RMSD and Rg trajectories align with the free energy analysis and formation of hydrogen bonds.

Table 4.8. Protein/ Protein-ligand complex and their Surface Accessible Surface Area

S.No.	**Protein/ Protein-ligand complex**	**SASA (nm^2)**
1	1JIL	165.31
2	1JIL-HA	163.99
3	2YXN	162.31
4	2YXN-HA	169.68
5	5CDP	493.76
6	5CDP-HA	269.76
7	6RKS	490.28

8	6RKS-HA	267.67

Table 4.9. Protein-ligand complex and their average Hydrogen bond formation

S.No.	Protein-ligand complex	H-Bond Average
1	1JIL-HA	~ 4
2	2YXN-HA	~ 5
3	5CDP-HA	~ 2-3
4	6RKS-HA	~ 2-3

Table 4.10. MM/PBSA free energy analysis of the protein complexes, SASA means Surface Accessible Surface Area

S.No.	Protein complex	van der Waal energy (kJ/mol)	Electrostatic energy (kJ/mol)	Polar solvation energy (kJ/mol)	SASA energy (kJ/mol)	Binding energy (kJ/mol)

1	1JIL-HA	-162.31 ± 14.10	-16.48 ± 9.43	111.14 ± 19.11	-17.80 ± 1.26	-85.45 ± 12.62
2	2YXN-HA	-68.08 ± 85.03	-12.13 ± 16.11	36.68 ± 65.26	-6.37 ± 7.95	-49.90 ± 64.19
3	5CDP-HA	-103.54 ± 13.90	-14.76 ± 9.52	83.09 ± 18.88	-12.06 ± 1.42	-47.28 ± 13.92
4	6RKS-HA	-88.45 ± 20.18	-12.55 ± 12.20	66.46 ± 33.59	-10.75 ± 2.35	-45.30 ± 21.33

This work falls under the purview of scientific investigations aiming to comprehend the function of biopolymer HA in regulating the processes of preventing bacterial infections. Hyaluronic acid has antibacterial and antioxidant properties, which many researchers have reported. These properties are suitable for their application in aesthetics. In addition, this product is not required for prior skin testing to enhance soft tissue.

Its property to hold water and maintain moisture when applied makes it a suitable candidate for skin gels and other applications. Its antibacterial properties will help it be used in gels and ointments for different skin treatments without damaging the skin tissues. Hyaluronic acid was fabricated by fermentation using *S. zooepidemicus* as our HA producer microorganism and then purified.

Systematic experimental work was performed for the antibacterial and antioxidant assay of the hyaluronic acid; molecular docking and simulations were carried out to determine the possible route of the following assays. Two ligands from our target bacteria were selected for docking and simulation: tyrosyl-tRNA synthetase and topoisomerase II DNA gyrase. The targeted ligand selection was not hypothetical; earlier research claimed the same ligand for the molecular antibacterial testing pathways (Pisano et al., 2019).

Our experiments showed a positive result in the antibacterial assays with a zone of inhibition of 12.38 ± 0.06 for *S. aureus* and 10.45 ± 0.05 for *E. coli* bacteria, and the IC_{50} values for the antioxidant assay were found to be 487.65 μg mL^{-1}. According to WHO guidelines for antimicrobial resistance, the zone of inhibition measurement states that the targeted pathogenic bacteria are susceptible to HA (Hudzicki, 2009).

Although the zone of inhibition obtained here is not strong enough to use HA as a solo antimicrobial agent compared to the other antibiotics used in the market, it enhances the effect of other biopolymers as an antimicrobial agent when combined with other biopolymers.

HA can indeed perform the dual function of encouraging the healing process and safeguarding scars from bacterial contamination, thereby preventing the requirement for antibacterial agents for preventive purposes.

Commonly, modest portions of HA (relatively low, over 1%) have been employed in the publications to establish HA for wound dressing and as an antibacterial agent (Fahmy et al., 2018; Michalska-Sionkowska et al., 2018; Silvestro et al., 2020). This information was used as HA has already been utilized for medicinal purposes. Docking and simulation studies were

opted to study the interactions and their binding affinity with various possible binding ligands.

The ligands were selected, and a precise result was obtained in the contexts of all the hyaluronic acid-ligand complexes. Systematic molecule docking was done, double-checked our docking results, and molecular simulations. The structure of the tyrosyl-tRNA synthetase from *S. aureus* (PDB ID: 1JIL) and *E. coli* (PDB ID: 2YXN) from the PDB, as well as the topoisomerase II DNA gyrase from *S. aureus* (PDB ID: 5CDP) and *E. coli* (PDB ID: 6RKS) were analyzed.

The binding energy of hyaluronic acid complexes and our positive control were comparable, and strong interactions, such as hydrogen bonds, hydrophobic interactions, and salt bridges, were observed between the molecule and the proteins. In our study, the test molecule's binding energy, interaction pattern, and positive control molecule are analogous, suggesting that hyaluronic acid may be an excellent alternative to the overused antibiotic ampicillin.

Molecular simulation results supported the docking results positively. Except for the 2YXN, all other three complexes, i.e., 1JIL-HA, 5CDP-HA, and 6RKS-HA, showed stability compared to the apoproteins. By this kind of stability, it was interpreted that HA actively binds at the active site of the apoprotein and prevents it from binding with the actual substrate for the multiplication of the bacteria.

2YXN-HA showed more randomness than the apoprotein, suggesting that this complex unstable the molecule and hinders its further interactions. Free binding energy simulated of this complex is relatively higher, and the main force contributing to it is Van Der Waal's

force. Our RMSD and Rg trajectories match the free energy calculations and hydrogen bond formation.